

UNIVERSITY OF OKLAHOMA

GRADUATE COLLEGE

THE INITIAL-FINAL MASS RELATION REVISITED: A MONTE CARLO APPROACH

WITH THE ADDITION OF THE M67 WHITE DWARF POPULATION

A DISSERTATION

SUBMITTED TO THE GRADUATE FACULTY

in partial fulfillment of the requirements for the

Degree of

DOCTOR OF PHILOSOPHY

By

PAUL ANTHONY CANTON

Norman, Oklahoma

2018

THE INITIAL-FINAL MASS RELATION REVISITED: A MONTE CARLO APPROACH  
WITH THE ADDITION OF THE M67 WHITE DWARF POPULATION

A DISSERTATION APPROVED FOR THE  
HOMER L. DODGE DEPARTMENT OF PHYSICS AND ASTRONOMY

BY

Dr. Mukremin Kilic, Chair

Dr. Kurtis A. Williams

Dr. Edward Baron

Dr. John P. Wisniewski

Dr. Braden Abbott

Dr. David P. Miller



# Contents

<b>List of Tables</b>	<b>vi</b>
<b>List of Figures</b>	<b>vii</b>
<b>Abstract</b>	<b>viii</b>
<b>1 Introduction</b>	<b>1</b>
1.1 Spectral Classification of White Dwarfs . . . . .	1
1.2 White Dwarf Cooling . . . . .	5
1.3 White Dwarf Masses . . . . .	8
1.4 Some Things We Can Learn From White Dwarf Physics . . . . .	12
1.5 Deriving the Ages of Open and Globular Clusters . . . . .	23
1.6 Deriving The Initial-Final Mass Relation (IFMR) . . . . .	25
1.7 Historical Context of the Work of this Initial-Final Mass Relation Analysis . .	30
1.8 The Scope of this Dissertation . . . . .	36
<b>2 Masses of White Dwarfs</b>	<b>39</b>
2.1 Methods by which White Dwarf Masses can be Obtained . . . . .	39
2.2 On Theory of White Dwarf Spectral Energy Distributions . . . . .	46
2.2.1 Natural Broadening . . . . .	48
2.2.2 Doppler Broadening . . . . .	49
2.2.3 Pressure Broadening . . . . .	49
2.2.4 Absorption Line Profiles . . . . .	57
2.3 Spectroscopy of our DA White Dwarf Sample and White Dwarf Masses . . .	58
2.3.1 Photometric Analysis . . . . .	59
2.3.2 Spectroscopic Observations . . . . .	60
2.3.3 Spectral Fitting Technique . . . . .	62
2.3.4 Spectroscopic Fits and Final Masses . . . . .	67
2.3.5 Splitting the Spectroscopic Degeneracy with Photometry . . . . .	78
2.3.6 On the Presence of Calcium . . . . .	84
2.3.7 Spectroscopic Peculiarities and Notable Objects . . . . .	86
<b>3 Testing for Membership and Isolation</b>	<b>89</b>
3.1 Requirement of Isolated, Single-Star Evolution . . . . .	90
3.2 Requirement of Cluster Membership . . . . .	94
3.2.1 Membership Cuts on Age . . . . .	96
3.2.2 Membership Cuts on Distance . . . . .	104
3.2.3 Membership Cuts on Proper Motion . . . . .	111
3.3 Comparison With Membership in the Literature . . . . .	115
<b>4 On the Initial-Final Mass Relation</b>	<b>119</b>
4.1 Extracting the Initial Masses . . . . .	121
4.2 The Initial-Final Mass Relation . . . . .	129
4.2.1 Our Monte Carlo Simulations . . . . .	134
4.2.2 Results and Discussion . . . . .	137

<b>5</b>	<b>Conclusions and Future Work</b>	<b>149</b>
5.1	Caveats and Future Work . . . . .	150
5.2	Concluding Remarks . . . . .	159

# List of Tables

2.1	M34 White Dwarf Data and Fit Atmospheric Parameters. . . . .	73
2.2	M35 White Dwarf Data and Fit Atmospheric Parameters. . . . .	74
2.3	M67 White Dwarf Data and Fit Atmospheric Parameters. . . . .	75
2.4	NGC 6633 White Dwarf Data and Fit Atmospheric Parameters. . . . .	76
2.5	NGC 7063 White Dwarf Data and Fit Atmospheric Parameters. . . . .	77
4.1	Random Error Dependence on Temperature . . . . .	125
4.2	Initial Masses of White Dwarfs in M34 . . . . .	126
4.3	Initial Masses of White Dwarfs in M35 . . . . .	127
4.4	Initial Masses of White Dwarfs in M67 and NGC 6633 . . . . .	128
4.5	White Dwarfs in Open Clusters Added to Our Sample From the Literature .	133

# List of Figures

1.1	Optical DA WD Spectra as a Function of Temperature . . . . .	4
1.2	Cooling of White Dwarfs . . . . .	9
1.3	White Dwarf Surface Gravity and Mass Distributions . . . . .	11
1.4	The Mass-Accretion Rate Plane . . . . .	17
1.5	Mass-Accretion Driven Evolution . . . . .	18
1.6	NGC 6791 Color-Magnitude Diagram . . . . .	26
1.7	Schematic Procedure of Extracting White Dwarf Masses . . . . .	28
2.1	Equivalent Width as a Function of Color . . . . .	44
2.2	Derivative of Equivalent Width with Respect to Temperature vs. Temperature . . . . .	45
2.3	Physical Parameter Dependency on Number of Lines Fit . . . . .	52
2.4	Physical Parameter Shift Due to Updated Stark Broadening Physics . . . . .	53
2.5	Atomic Hydrogen Opacity of a 20,000K DA White Dwarf . . . . .	54
2.6	Theoretical Line Profiles at Various Temperature and Surface Gravity . . . . .	58
2.7	Normalized Balmer-Line Profiles and Best Fit Solutions for White Dwarfs in M34 . . . . .	79
2.8	Normalized Balmer-Line Profiles and Best Fit Solutions for White Dwarfs in M35 . . . . .	80
2.9	Normalized Balmer-Line Profiles and Best Fit Solutions for White Dwarfs in M67 . . . . .	81
2.10	Normalized Balmer-Line Profiles and Best Fit Solutions for White Dwarfs in NGC 6633 . . . . .	82
2.11	Normalized Balmer-Line Profiles and Best Fit Solutions for White Dwarfs in NGC 7063 . . . . .	83
3.1	Binary Fraction as a Function of White Dwarf Mass . . . . .	95
3.2	Age Cut for M34 . . . . .	99
3.3	Age Cut for M35 . . . . .	100
3.4	Age Cut for M67 . . . . .	101
3.5	Age Cut for NGC 6633 . . . . .	102
3.6	Age Cut for NGC 7063 . . . . .	103
3.7	Distance Cut for M34 . . . . .	107
3.8	Distance Cut for M35 . . . . .	108
3.9	Distance Cut for M67 . . . . .	109
3.10	Distance Cut for NGC 6633 . . . . .	110
4.1	The Initial-Final Mass Relation From 1 to 7 Solar Masses . . . . .	138
4.2	Density Map of The Initial-Final Mass Parameter Space . . . . .	139
4.3	Slope Frequency . . . . .	146
4.4	Intercept Frequency . . . . .	147

# Abstract

The initial-final mass relation (IFMR) describes how the initial mass of a stellar object maps to its mass as a remnant. The focus of this work is to re-examine this relation for low to intermediate mass stars.

Studies of the IFMR have been used in derivations of the age of the galactic components, to measure the total integrated mass loss from stars, to bound the initial mass which will form a white dwarf as opposed to a core collapse supernova, and to study the effects of post-main sequence evolution on exoplanet systems.

Given stellar lifetimes far exceed what we can observe in real time it is impossible to measure both a star's mass as it once was when it came to be as a star and its mass as a stellar remnant. For this reason, we look to objects which are white dwarfs (WDs) to get the latter piece of information and use the fact that they are in clusters of known age to get the prior piece of information. With both the initial and final mass of the object in hand it is then possible to fit a function to the data to obtain the IFMR.

This dissertation presents the first spectroscopic analysis of WDs in the aged solar-metallicity open cluster M67, a reanalysis of the M34, M35, NGC6633, and NGC7063 WD samples, and an IFMR from the application of the spectroscopic technique for deriving WD masses with a Monte Carlo approach to explore the uncertainties in the initial and final masses in an improved way.



# Chapter 1

## Introduction

White dwarfs (WDs) exist as an oddity of nature. They are found in a parameter space of luminosity where no star at such a temperature could possibly exist as understood with the physics of the Sun. When combined with the fact that their spectral energy distributions roughly follow that of a black-body emitter it is clear that WDs must be much smaller in size than the majority of stellar objects. Being roughly the size of the Earth but comprised of about half the mass of the sun, they are of immense densities ( $\sim 10^6 \text{ g cm}^{-3}$ ). It is in tribute to this that we refer to WDs as compact objects.

### 1.1 Spectral Classification of White Dwarfs

Common features or patterns allow us to study distinct underlying physical mechanisms, and so classification is often used in astronomy to study groups of objects. As unimpeded photons can only escape WDs from about 1% of their radius<sup>1</sup>, the physical

---

<sup>1</sup>Optical depth ( $\tau$ ) is a measure of the level of transparency in a medium. It is a function of density ( $\rho$ ), depth into the object ( $z$ ), and opacity ( $\alpha_\nu$ ) which is itself dependent on wavelength. If we only consider photons whose path length is perpendicular to the surface and assume for simplicity that density and opacity are constant with depth, then the relationship between these parameters is:  $\tau = \alpha_\nu * \rho * z$  (Carroll & Ostlie, 2006, Equation 9.37). Figure 2.5, from Tremblay & Bergeron (2009), suggests that between the lower Balmer lines of hydrogen, where the opacity is lower and photons can more easily escape from a greater depth, the log of the opacity is  $\sim 10^{-5} \text{ cm}^2/\text{g}$ . Kowalski (2006, Figure 5) suggests that at  $\tau \approx 2$ , or the depth in the atmosphere from which just 14% of photons escape the object,  $\rho \approx 0.02 \text{ g/cm}^3$ . Putting it all together and solving for depth, one finds that just 14% of photons with wavelength between the Balmer lines escape from a depth of  $10^7 \text{ cm}$ , or  $\sim 1\%$  of the radius of a typical WD. Some caveats are that the optical depth from Kowalski (2006) is the Rosseland depth, a weighted value over a broad range of wavelengths, for a 6,000K WD, whereas the opacity we have adopted from Tremblay & Bergeron (2009) describes an order of magnitude estimate of the unweighted opacity between lines for a 20,000K WD. As such it is likely our approximation of depth is an overestimate, but we have safely illustrated that the physical parameters we extract

parameters we measure are representative of just the stellar atmosphere. Therefore, the atmosphere provides us with our observable quantities, and it is quite natural that we classify WDs by common features in their spectral energy distributions. While the spectral energy distributions of these objects are governed by surface gravity, temperature structure, and chemical composition, it is by their spectrum’s chemical footprint that we have historically classified them.

The present classification scheme of WDs was defined in the work of Sion et al. (1983). WD spectral classification always starts with a D which indicates an object is a dwarf. This is followed by an upper case letter indicative of the dominant spectroscopic feature in an optical spectrum, which is in turn followed by an uppercase letter for any other less prominent spectroscopic features present in any part of the electromagnetic spectrum. Occasionally, a number rounded to the nearest half integer is appended to indicate some idea of effective temperature, following from  $50400\text{K}/T_e$  (Kawaler, 1995; Wesemael et al., 1993). Here we illustrate the most common classifications:

- DA      Hydrogen lines are present; with no helium I or metal lines
- DB      Helium I lines are present; with no hydrogen lines
- DO      Helium II lines are present; accompanied by He I or H lines
- DQ      Carbon lines present in any part of the electromagnetic spectrum
- DZ      Metal lines are present; no hydrogen or helium

---

describe the atmosphere. For reference, the sun’s photosphere ( $\tau = \frac{2}{3}$ ) is at a depth of 525km (Carroll & Ostlie, 2006), while (Bergeron, 1989, Page 55) state the atmosphere of a WD extends to  $\sim 10^{-4} R/R_\star$ , or on the order of just 1 km.

- DC      Continuous spectrum

It is important to note that the lack of an element in a spectrum (or in the WD's spectral type) does not mean it is not present. It may be simply that the physical conditions are such that the relevant electron levels are not sufficiently populated. Furthermore, the spectral type may evolve as the species present in the atmosphere may change in time due to accretion, gravitational settling of heavier elements out of the atmosphere, or the onset of changes in opacity which drive convection as the WD cools and forms atomic or molecular species (Koester & Chanmugam, 1990; Bergeron et al., 1997).

Figure 1.1 provides illustrative examples of optical DA WD spectra. Spectra have been offset vertically for clarity, and organized as a function of effective temperature (hottest objects at top). The names of each object derive from the McCook and Sion catalog (McCook & Sion, 1987), and the Balmer lines  $H\alpha$  through roughly  $H8$  can be seen, depending on the particular spectrum. The line strength is a function of effective temperature as electrons tend to be ionized in high temperatures and in the ground state at lower temperatures. Surface gravity, through pressure broadening, also plays a small roll in the shape of the line profile. Objects of DC spectral type show no significant spectral lines, the continuum itself being rather similar to the coolest DA example illustrated in Figure 1.1.

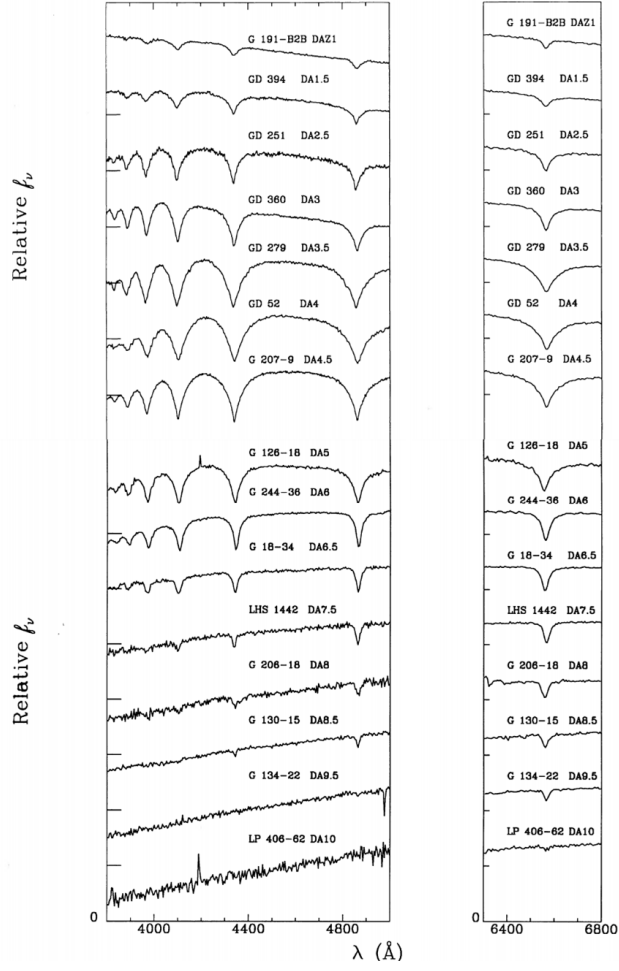


Figure 1.1: Optical spectra of DA WDs as a function of effective temperature, ordered from top to bottom from hottest to coolest with an arbitrary vertical offset for clarity. Characterized by the strong Balmer lines of hydrogen ( $H\alpha$ , right panel,  $H\beta$  through roughly  $H8$ , left panel), the line profiles of these objects is described by the physics which govern electron populations of each energy level. For a fixed surface gravity, peak line strength falls off to either side of an effective temperature at which the electron populations are at maximum. About 75% of WDs are DAs. Figure adopted from Wesemael et al. (1993).

## 1.2 White Dwarf Cooling

The true age of the Sun has long been studied. Early works derived its age from the gravitational potential energy liberated during its formation, while later works suggested nuclear processes were the dominant source of energy production (Stacey, 2000; Eddington, 1920; Burbidge et al., 1957, and references therein). In general, over the course of time a star finds equilibrium where the relentless inward pull of gravity is negated by outward thermal pressure. This balance results in a fixed set of physical parameter values at any phase of stellar evolution. As higher mass objects support themselves against a stronger gravitational pull they tend to burn through their fuel quicker as they require more thermal support, but no matter the mass of the star when the material of the light element being processed begins to run out the star will reconfigure itself to find equilibrium again. This process repeats itself as the star progressively processes heavier elements.

Near the end of the course of stellar evolution low and intermediate mass objects are comprised of cores which are primarily carbon and oxygen. Enhanced mass loss is periodically driven by runaway fusion of a narrow shell of degenerate helium surrounding the inert core in what is called a thermal pulse. The radial pulsation of the envelope which follows drives the formation of dust, which is in turn driven from the object through the absorption of radiative momentum (Vassiliadis & Wood, 1993). As the helium shell rebuilds from the hydrogen burning shell above it and the cycle continues over and over what remains of the hydrogen envelope surrounding the helium shell is shed until conditions are insufficient for any further fusion to proceed, ushering in the

transformation of the star to a WD. As the object begins to cool there is a small amount of residual contraction which liberates some gravitational potential energy. Although radiative levitation is important for hot WDs heavy elements generally sink out of the atmosphere, leaving trace amounts of the lightest elements are left to populate the surface. This description is true only of stellar evolution for low and intermediate mass stars - their more massive counterparts experience core collapse before exhausting their stellar fuel as conditions in their core are such that carbon and oxygen can be processed to heavier elements.

From the fact that the physics of WDs are relatively simple and that they generally lack a significant source of energy generation one can derive the timescale for the object's existence as a stellar remnant (Fontaine et al., 2001). As a WD we observe today has long since ceased contraction and the production of heavier elements within its core via fusion it cools radiatively, monotonically draining its pool of internal energy in time. The internal energy of the remnant is a function of how many ions per unit mass the remnant is made of, or in other words its composition. While direct measurement of the internal structure of the star is impossible, indirect probes such as asteroseismology have actually shown that their internal composition is predominantly oxygen (Giammichele et al., 2018), with a substantial proportion of carbon. More massive WDs may be an exception to this, instead having a core comprised of oxygen, neon and magnesium, but in either case the amount of internal energy the WD possesses and the rate at which it radiates energy can be modeled and so it is possible to predict the timescale for how long it has taken for a WD to cool to its current temperature, or in other words how

long the object has been in existence for as a WD.

WDs cool rapidly when in excess of temperatures on the order of 35,000 K. So much so, that the timescale of which a WD has cooled for is not sensitive to the initial temperature of the WD model. The reason for this is that the dominant physical process by which WDs cool at high temperatures is not an electromagnetic process. Unlike photons which scatter as they find their way to the surface of the object before energy is radiated away, in hot WDs neutrinos are produced from plasmon decay which leave the WD from nearly any depth without undergoing multiple scattering events. This process shuts off when the isothermal core has cooled to the point at which plasmons are no longer produced in significant quantities, and the relatively inefficient process of radiative cooling becomes the dominant mechanism.

As the WD cools even further, now through radiative transfer, the rate at which energy leaves the remnant is dependent on the atmosphere's thickness as well as composition, which sets the opacities. Convection begins, and material from greater depths is pulled up as the remnant further cools. When convection reaches the depth at which the core is degenerate the bulk movement of material has a significant effect on the cooling rate since the transportation of energy is less reliant on rather inefficient radiative and conductive processes. At low temperatures crystallization settles in, with the phase change having a significant role in altering the cooling rate through a change in the specific heat of the material. More massive WDs have higher densities and tend to solidify first, thereby cooling fastest at low temperatures even though they initially start out with higher energy reservoirs.

Figure 1.2, from Fontaine et al. (2001), illustrates this process and quantizes the temperatures by which these mechanisms are apparent for carbon core DA WDs. The physics of these remnants describe how long a WD has been cooling, and is therefore central to understanding the age of such objects. The importance and use of knowing WD ages in the context of the IFMR can be found in sections 1.6 and 3.2.1.

### 1.3 White Dwarf Masses

The mass of a WD can be found through a number of independent methods (see section 2.1 for a detailed discussion). While the variety of techniques provide a test of accuracy, some methods can be more widely applied than others. One of the most versatile and precise is called the spectroscopic technique (Bergeron et al., 1992a), which we use in the course of this dissertation. In this technique a series of model spectra are compared to an observed spectrum, and the physical parameters of the best fit model simultaneously reveals our best correspondence of the WD's temperature and surface gravity. From the surface gravity the mass of the WD can be found, as we shall describe.

The surface gravity of a WD is unlike anything we are familiar with from our day-to-day lives. As the surface gravities of WDs vary over many orders of magnitude it is common to express the surface gravity using a logarithmic scale. It is well known that the acceleration at the surface of Earth is about  $10 \text{ m/s}^2$  - converting to CGS units, the surface gravity on Earth becomes about  $1,000 \text{ cm/s}^2$ , or  $10^3$ . The logarithm of base ten presents this simply at 3. In these units, WDs exhibit the log of their surface



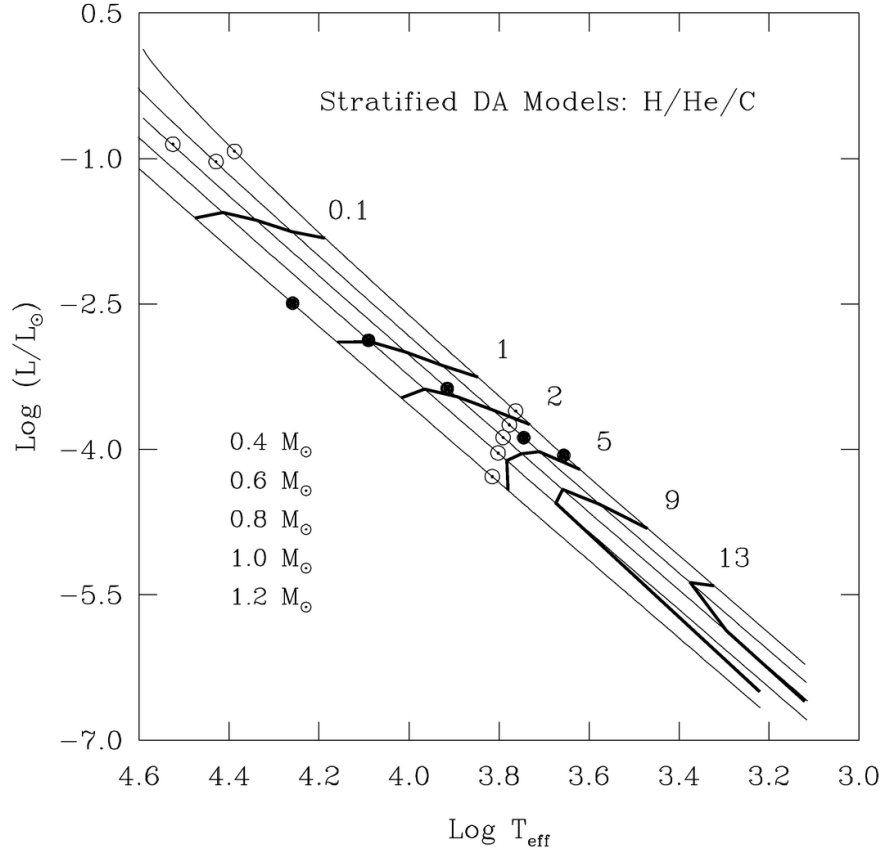


Figure 1.2: Cooling of five WD models are depicted with solid tracks, which proceed from top left (hot, bright, and young) to bottom right (cool, faint, and old), in the luminosity-temperature plane. From top ( $0.4 M_{\odot}$ ) to bottom ( $1.2 M_{\odot}$ ) each track depicts a WD of successively higher mass. Bold solid black lines cross the evolutionary tracks which depict lines of constant cooling age in billions of years, indicated by the number to their upper right. To the right end of the open circles near  $\log T \approx 4.4$  the dominant cooling mechanism is radiation, while convection drives deep enough to couple the atmosphere to the degenerate core below the open circles near  $\log T \approx 3.8$ . Solid circles illustrate where cooling temporarily pauses during crystallization. Figure adopted from Fontaine et al. (2001).

gravity, or  $\log g$ , to typically have values ranging from 6 to 9.

Converting from the surface gravity to mass requires both the mass-radius relation and some basic physics. With a lack of nuclear energy generation in the core to maintain the thermal pressure which holds a stellar object up, the object will shrink to a point where electron degeneracy pressure dominates the internal equation of state. While gravity has made strides towards collapsing the object under its own weight, as long as the final mass of the object is under the Chandrasekhar Limit it will continue to support itself against gravity by electron degeneracy pressure as a WD. WDs therefore follow the inverse mass-radius relation,  $R \sim M^{-1/3}$ . While there is also some dependency on core composition, the more massive the remnant is the smaller it is in size and the higher its surface gravity.

Although it is appropriate to quantify the relation between surface gravity and mass with the theory of General Relativity in combination with the mass-radius relation, a simplified Newtonian approach can illustrate the basic principle. It is well known that  $|F_g| = \frac{GMm}{R^2}$ . It is also well known that the surface gravity of an object is just the acceleration a point mass would feel at the radius of that object,  $|g| = |a| = |F/m| = \frac{\frac{GM_{WD}m_{particle}}{R_{WD}^2}}{m_{particle}} = \frac{GM_{WD}}{R_{WD}^2}$ , where we have written the surface gravity of the WD as  $g$ . Algebraically inverting this equation allows one to find a relationship for the mass of a WD:  $M_{WD} = gR_{WD}^2/G$ . As the WD is primarily supported by electron degeneracy pressure the dependence on  $R_{WD}$  can be eliminated with the mass-radius relationship, leaving the mass of the WD in terms of a number of constants and the surface gravity alone. In summary, where the spectroscopic technique can be applied a

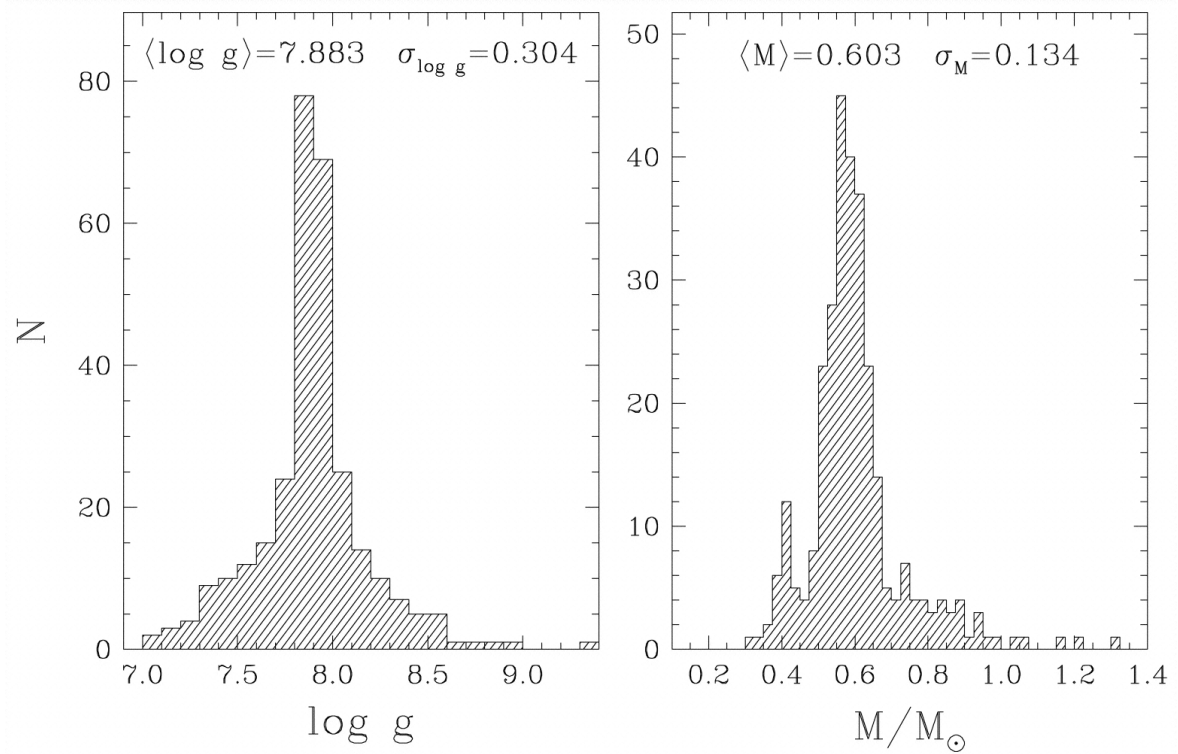


Figure 1.3: The WD surface gravity (left panel) and mass (right panel) distributions from 298 objects in the magnitude limited Palomar-Green sample (Green et al., 1986; Liebert et al., 2005a). The mass distribution is narrow, centered around  $0.603 M_\odot$  with a standard deviation of  $0.134 M_\odot$ .

single spectrum is sufficient to derive the mass of a WD.

The mass distribution of WDs has been studied using this approach (Bergeron et al., 1992a; Liebert et al., 2005a). To give some idea of the shape of this distribution we have borrowed Figure 12 of Liebert et al. (2005a), illustrated in Figure 1.3. The mass distribution for WDs is very narrowly peaked around  $0.6 M_\odot$ .

We can understand the sparse nature of the high mass end through the initial mass function (IMF), which describes the rate of which objects of various zero age main

sequence (ZAMS, or initial) mass come to be for a population of stars. The slope of the IMF suggests that there are fewer stars at higher masses than there are at lower masses. One could use the IMF to show the vast majority of all stars will eventually form WDs by integrating the IMF over the ZAMS mass range by which stellar evolution guides objects to the WD stage. Indeed, just as the IMF predicts there should be fewer neutron stars and black holes than there are WDs it also suggests that there should be fewer WDs at higher masses.

An understanding of the sparse nature of the low mass end stems from stellar evolution. While the IMF suggests that there should be an ever increasing amount of WDs towards lower masses, low mass WDs evolve from low mass stars of which many are not of sufficient age to have reached the remnant stage. While the age of the Milky Way places a firm limit on the least massive WD that could have formed through isolated evolution, this sharp mass cut off is slightly broadened as the stars these WDs form from are of various age and metallicity. In addition, the low mass end is further infused by WDs which have come to be through a binary channel, especially in the case of the lowest mass WDs in the distribution.

## **1.4 Some Things We Can Learn From White Dwarf Physics**

We examine WDs not just because they are intriguing facets of nature, but because our understanding of them allows us to investigate many aspects of physics and astronomy. Through the examination of WDs one can, amongst other things, study plasma physics at extreme densities, test stellar evolution, examine the evolution of

galaxies, and derive the ages of the Milky Way’s components. Indeed the initial-final mass relation (IFMR), a fitted function that describes the dependency of an object’s initial and final masses, is but one tool to come from WD astrophysics which makes the study of some of the aforementioned topics possible.

The physics which guide supernovae, and in turn cosmology, follow from the physics of WDs. The composition of a WD can be thought of as fuel because of the fact that fusion of its constituents liberates energy. Furthermore, the Chandrasekhar limit is well defined so there is a natural maximum amount of fuel contained in a WD before explosion. Therefore, any WD which accretes material collapses with roughly the same amount of potential energy to liberate. An accreting WD steadily shrinks in size as its mass grows, leading to higher pressure and density in the interior regions of the WD. Eventually carbon burning processes commence. This additional source of energy is balanced by energy losses in the locality of carbon fusion from both convection within the WD interior and neutrino losses due to the Urca process (Paczynski, 1972; Iben, 1978). While convection moves energy, it also can stir neutron rich ions which have readily captured an electron and emitted a neutrino in the deep interior to cooler regions where such ions can relax to their former state by releasing an electron and an anti-neutrino. The net effect is that neutrinos have been created which easily escape the remnant, thereby cooling the WD. Modern models of this so called ‘simmering’ phase suggest that there is generally a rise in temperature which eventually leads to runaway fusion (Zingale et al., 2009, 2011). Moreover, even in the case where the rate of fusion fails to break out into a thermonuclear shock front, eventually the collapse

of the WD would occur beyond the Chandrasekhar limit leading to sufficient physical conditions to propagate a flame front throughout the degenerate remnant. In either case, enough energy is released to unbind the star as a type Ia supernova.

More generally, supernovae are thought to either derive from the explosion of a massive WD or from the collapse of a degenerate iron core in a massive star. The latter reach the physical densities and temperatures in the core for carbon to steadily burn and nuclear processes continue all the way up through the formation of iron. There is a critical mass by which a star has enough self-gravity to do this, below which the final stage of evolution is a WD. This critical mass value has been observationally constrained from above by the detection of the progenitor star in pre-explosion images of core collapse supernovae to be  $8.5^{+1.0}_{-1.5}M_{\odot}$  (Smartt et al., 2009), whereas the existence of massive WDs has constrained the value from below at somewhere between  $6.3$  and  $7.1M_{\odot}$  (Williams et al., 2009). While massive WDs are relatively few in number and cool so quickly they are often difficult to detect studies of the IFMR pursue such WDs to populate the IFMR parameter space, and in doing so they often uncover the most massive WDs known for which the mass of the progenitor can be derived. This is to say that, work pertaining to the advancement of the IFMR not only influences our understanding of chemical evolution by defining how much material a star of a given mass sheds back into the interstellar medium (ISM), but also by constraining the exact value of the critical mass from below which effects metal yields from supernovae over many generations of stars.

As stars process material into heavier elements in time, chemical evolution of galaxies

is sensitive to not just the frequency of supernovae but of which type (Nomoto et al., 1984). While the number of massive stars is fixed by the IMF and the fraction of these which undergo core collapse is constrained by both pre-explosion images of progenitors and massive WDs, yields of the iron group elements are predominately determined by the fraction of supernovae of type Ia. The frequency of these supernovae should be tied to the frequency at which WDs achieve the Chandrasekhar limit, which is largely governed by the accretion rate for each remnant. Figure 1.4, of Ma et al. (2013), illustrates the Goldilocks regime by which any particular WD can accrete material in such a way that it will grow in mass. At low accretion rates material slowly piles on, is supported by degeneracy pressure, and is blown back off the WD in episodic novae when eventually conditions are ripe for fusion on the surface and a thermonuclear runaway proceeds. At the highest accretion rates material also piles up before a hydrogen shell flash is triggered. Steady burning follows and radiation pressure limits the rate by which mass is accumulated as unprocessed material is blown off as an optically thick wind. At slightly lower rates material is able to accrete without any being blown away, and the object undergoes steady shell burning under an envelope as would be the case for a Red Giant. In either high accretion rate regime the mass of the WD increases, but at a very leisurely pace. At still lower accretion rates material is burned at a rate commensurate with the accretion rate, and the processed material remains bound to the object growing its mass in a sustainable and relatively rapid fashion. Figure 1.5 illustrates an alternate look at this process, showing how the core mass of the remnant grows in each of these regimes as a function of time. Only in the steady burning state

does the WD mass approach the Chandrasekhar Limit in rapid fashion (solid black line, middle panel), illustrating that only in such a regime of the rate of accretion do WDs explode as a type Ia supernova within a reasonable time frame, thereby chemically enriching the ISM. Of course, this process requires that the material accreted comes from somewhere. Although metals, which should settle out of the atmosphere of a WD rapidly, have been observed in the spectra of some WDs accretion of material from asteroids, comets, or from the ISM is unlikely to grow a WD to the Chandrasekhar mass. Rather, significant accretion likely occurs in binaries where a donor star fills its Roche lobe and material spills over to the companion. Supernovae, as brilliant as they are, are observed in galaxies of significant redshift (Cooke et al., 2012; Riess et al., 1998). Supernovae of type Ia are important standardizable candles for cosmological studies, extending the impact of WD physics to the edge of the observable universe and to the frontiers of philosophy.

Deriving the IFMR is one more facet studying the physics of WDs makes possible. However, the IFMR itself has found a wide range of applications in modern astrophysics. Its strength is simply that the ZAMS mass of any field WD can easily be found.

A recent example of this utility showed that the presence of debris disks around WDs is likely correlated with the presence of exoplanets around these remnants. This is particularly intriguing as there has not yet been a direct detection of an exoplanet around a WD. Debris discs were thought to be correlated with the presence of exoplanets as they may perturb the orbits of minor bodies, some of which would break up as they pass within the Roche limit of the WD (Debes & Sigurdsson, 2002). To explore



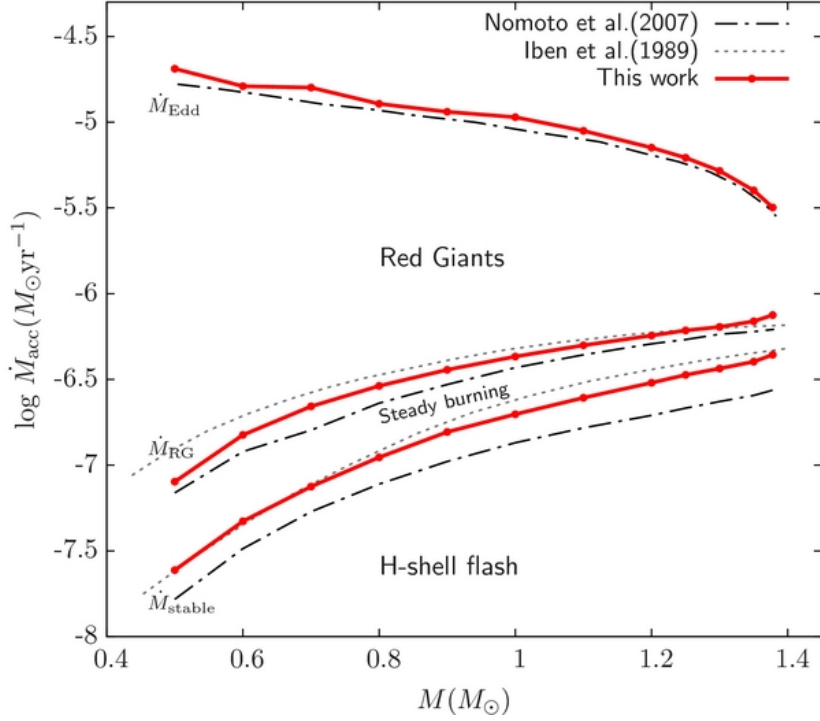


Figure 1.4: From Ma et al. (2013), the parameter space of WD mass against accretion rate as it defines model dependent regimes of physical phenomena. At the lowest accretion rates degenerate material piles up before ignition triggers nuclear run aways on the surface of the WD referred to as thermal pulses. At higher accretion rates material accreted is burned in a steady sense as it falls onto the object and the WD grows in mass. At high accretion rates steady burning isn't rapid enough to process material as it accretes onto the surface and the remnant grows into a red giant like object burning material in a shell. At the highest accretion rates the object is constrained by the Eddington limit. Solid, dashed-dotted, and dotted curves depict models which describe transitions in parameter space between these phenomena.

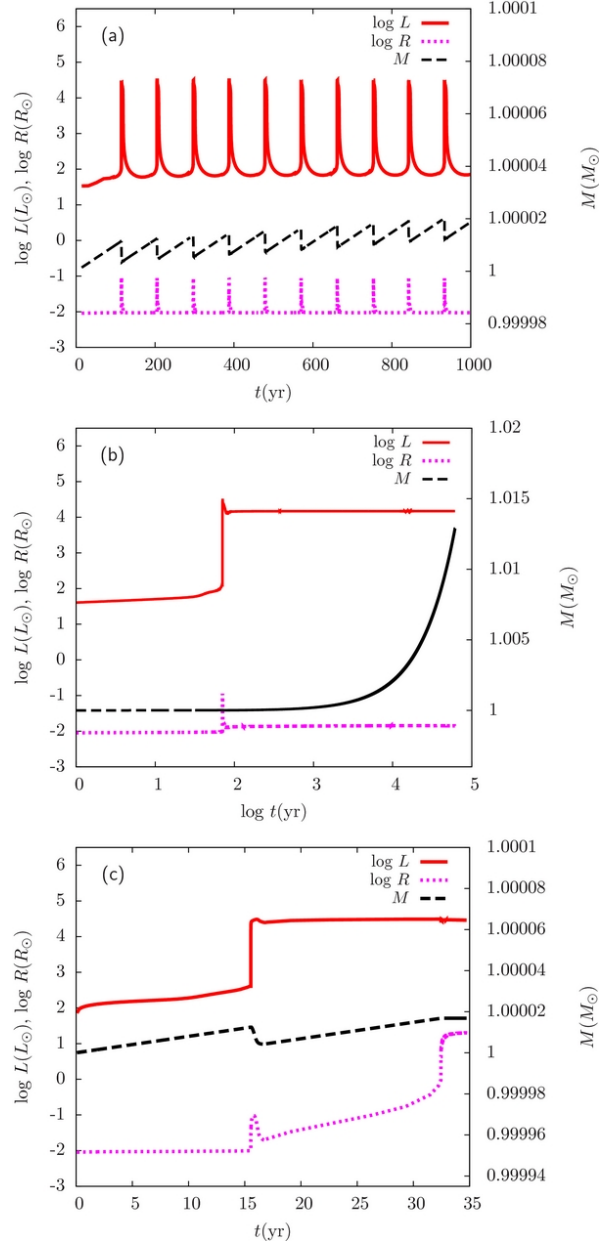


Figure 1.5: From Ma et al. (2013), the evolution of luminosity, object mass, and size are described for thermal pulse (top), steady burning (middle) and red giant like (bottom) regimes. Only in the steady burning regime does the object grow relatively rapidly as a WD towards the Chandrasekhar limit.

this Barber et al. (2016) examined the frequency of debris disks around WDs as a function of final mass, and found the frequency peaks around  $0.70 M_{\odot}$ . The IFMR was applied to this to express the frequency distribution of debris discs around WDs in terms of ZAMS mass, and intriguingly this was found to closely mirror the prediction of giant planet formation as a function of ZAMS mass. This directly supports the idea that debris disks around WDs are correlated with the presence of exoplanets around these remnants. The very presence of such exoplanets would have implications for how planetary systems evolve through the late stages of stellar evolution.

The ease of getting the ZAMS mass of a WD through the IFMR also enables study of the age of the individual galactic components, and hence the sequence by which they formed. The components are made of the stellar populations contained within, so the age of a WD population under study is identified as the age of the galactic component. The age of the population of WDs can be found by modeling the observed distribution of their brightness. The distribution falls off sharply at faint luminosity as any WD sample under study is pulled from a stellar population of finite age where the remnants have simply not had enough time to cool and fade to lower levels. Each model is described by an integral in ZAMS mass over the IMF (the number of stars formed at a given ZAMS mass), the star formation rate, and the inverse of the cooling rate factored together (Fontaine et al., 2001). Here, the IFMR must be used to convert terms in inverse of the cooling rate from WD to ZAMS mass. As the models are sensitive to age, by comparing a series of them to the observations the best fitting model can be identified, whose age is identified as that of the WD population. The kinematics, or

how these WDs are moving as they orbit about in the Milky Way, then reveal if the derived age is that of the galactic halo or the disk.

In a similar manner a lower limit can also be placed on the age of a galactic component by the detection of the single oldest WD with kinematics which characterize that component. With the IFMR the total age of the coolest WDs in any galactic component can easily be found to reasonable precision so these objects are a natural choice over alternatives which might also be ancient but difficult to date with precision (such as main sequence dwarfs). A series of models can be used to find a suitable fit to the observed photometry of each remnant, whereby the cooling age and final mass can be found. The IFMR then gives the WD's initial mass, through which a stellar evolution model can reveal the object's lifetime as a star. Adding this to the cooling age then gives the object's total age, and thereby a lower limit on the age of the component its kinematics suggest it is a part of. However, the aforementioned technique is more favorable as with it a precise age is possible from a large sample size. Also, there may always be a significantly older WD out there with similar kinematics waiting to be identified.

The IFMR also allows us to examine mass loss and core growth, which pertain to both stellar and galactic evolution. With it we can semi-empirically quantize the mass an object sheds over its entire existence and use this to test models of stellar evolution. The total mass a low to intermediate mass star sheds back into the ISM over the course of stellar evolution is simply the difference between the initial and final mass. This is a function of ZAMS mass, with more massive objects shedding not only more

material back out into the ISM but a larger fraction of the mass they came to be with (Kalirai et al., 2008, Figure 11). The IFMR has also been used to test stellar evolution through the effects of convective overshoot (in which material driven by convection moves beyond the unstable region). This effects the growth of the core, and has been shown to be an important factor in models of stellar evolution (Salaris et al., 2009). Continued refinement of the IFMR will further allow careful examination of stellar evolution.

Models of galactic evolution enable the study of the history of galaxies through making predictions of their observed spectral energy distributions. In the optical, most of the light emitted by a galaxy is from its stellar populations. The models describe the characteristics of these underlying populations by predicting a spectral energy distribution based on a set of fixed characteristics (e.g. star formation history, metallicity evolution, the IMF). The model which predicts the spectrum which most closely resembles an observed galaxy’s spectral energy distribution therefore reveals our best representation of that galaxy’s evolution throughout time. Computational limitations prevent such large stellar populations from being individually resolved, so evolutionary population synthesis is typically employed. These models are described by an integral in time over the star formation rate convolved with the sum of the spectral energy distributions of the stellar populations therein. At each moment in time the spectral energy distribution of each underlying stellar population is described by a stellar isochrone (e.g., see Figure 1.6) which is weighted by the IMF. However, it is difficult to accurately model stellar evolution from the ZAMS through the WD stage so

it is uncommon for the required isochrones to be available. This is in part due to the fact that in the late AGB phase both thermal pulses and convective mixing of heavier elements pulled into the atmosphere from below (dredge up) lead to rapid changes in surface brightness which are difficult to accurately describe as degeneracy in a galaxy's color can arise from the effects of age, metallicity, or dust (Bruzual & Charlot, 2003). This late stage of stellar evolution is particularly important as evolved stars contribute a significant fraction of the light from a galaxy. To address this Bruzual & Charlot (2003) stitched together a series of independent models of stellar evolution to describe the entirety of stellar evolution. In this process, the light emitted by WDs was incorporated by using the semi-empirical IFMR to map ZAMS mass to WD mass, from which WD cooling models described the contribution to the model galaxy's light produced by these remnants.

In a similar sense, Renzini & Ciotti (1993) invoked the IFMR to derive the mass-to-light ratio of old stellar populations (of which galaxies are comprised). This parameter evolves in time as its constituents do, and so it can also be used to constrain the star formation history of a galaxy. The mass-to-light ratio is the sum over all the objects in a galaxy as represented by an integral over the mass of each object divided by its luminosity. Since luminosity follows a power law for stellar objects, the authors write the integral representation over ZAMS mass alone, but the integral must be broken up over intervals representing ZAMS masses which result in WDs, neutron stars, and black holes. A relation must then be used to map remnant masses to ZAMS mass, such as the IFMR, to evaluate the integral over each appropriate interval.

## 1.5 Deriving the Ages of Open and Globular Clusters

Open and globular clusters are groups of stars. The stars in an open cluster all share the same metallicity, or fraction of material which is not hydrogen or helium, alluding to the idea that in each open cluster the stars are all of the same age having come to be from the collapse of a single molecular cloud. Open clusters tend to consist of a young population of hundreds to thousands of stars. These clusters dissociate in time as the cluster's gravitational potential well is not always deep enough to keep the objects bound as they periodically perturb the orbits of one another.

On the other hand globular clusters are of a much deeper potential well, consisting of tens of thousands to hundreds of thousands of stars. These do not dissociate in time, and are observed to consist of stellar populations which are much older than those found in open clusters. The formation of some globular clusters remains poorly understood as their stellar populations exhibit a bimodal distribution in a color-magnitude diagram (see below for example), which may be evidence of either a large binary fraction or evidence of subpopulations of different metallicity or age.

The precision of the results of this dissertation, and in turn our conclusions, in part hinge on both the ages of the clusters assessed in the study and the precision by which these ages are known. It is therefore important to understand how the ages of the open clusters in our study have been obtained. While previous works have determined cluster ages in various ways, we have used the common method of fitting a stellar isochrone to the color-magnitude diagram of the cluster's stars.

A group of model stars of various mass but the same age can be varied in age

until the physical parameters of stars in the model, when corrected for distance, are a good representation of the observed distribution in apparent magnitude and color of stars in the actual cluster. A set of model stars at one age form what is known as a stellar isochrone. Often, the distribution in mass is interpolated such that the isochrone is continuous, and in common practice the cluster age is usually found directly by obtaining the best fit stellar isochrone to the distribution of observed stars, which is illustrated in a color-magnitude diagram.

An example of this for the open cluster NGC 6791 is shown in Figure 1.6. Color is measured by subtracting how bright each object appears through two filters ( $B-V$ ), while  $V$  is a measure of how bright an object is as seen by an observer on Earth. Much of the scatter in the plot is due to objects foreground or background to the cluster in the same area of the sky as the cluster, called field stars, but the cluster objects form a clear distribution in this parameter space which is followed well by the isochrone for 8.5 billion year old stars (shown in red). Of the many isochrones which were compared to the data this particular one proved to be the best match, characterized by the additional parameters depicted in the legend on the right. The distribution of objects in the various sequences represent objects at a common phase of stellar evolution, e.g. the large central group of objects cutting from upper left to bottom right between  $B - V = 0.9$  to about 1.6 are stars of various mass burning hydrogen in their core. This is the main sequence. Objects are dynamic in this figure in the sense that over the eons they move between the different groups depending on the physics which characterizes them at the time. More massive stars are to the upper left on the main sequence, with



the most massive objects no longer being on the sequence having moved to the right at low apparent magnitude (high apparent brightness) as they are beyond the epoch of fusing hydrogen in their core. It is this dynamic property which bears sensitivity to age through which we can date the cluster. The bracketed parameters describe the abundance of various elements. Higher metallicity contributes to increased absorption of light at particular wavelengths which effects color, so metallicity must be taken into account to make sure the model is a fair comparison to the observations. The other parameters in the legend are required to make a fair comparison to the observed data as there are some dependencies that go beyond the models of stellar evolution. For example, the model isochrone has been corrected for distance, expressed in this figure by the distance modulus,  $(m - M)_0$ , which is independent of stellar evolution as it is a property of the particular cluster under study. Similarly, the color excess,  $E(B-V)$ , describes the reddening effect of the tenuous material that exists in space which preferentially scatters bluer light out of the line of sight. Only when all of these parameters are taken into account can an accurate isochrone, and hence the cluster's age, be found.

## 1.6 Deriving The Initial-Final Mass Relation (IFMR)

The IFMR is derived through regression analysis of a sample of objects with known initial and final masses. There is more than one way to obtain the initial and final mass for an object. Various techniques exist to derive the ZAMS mass of stars, but to derive their final mass would require models of stellar evolution which describe objects

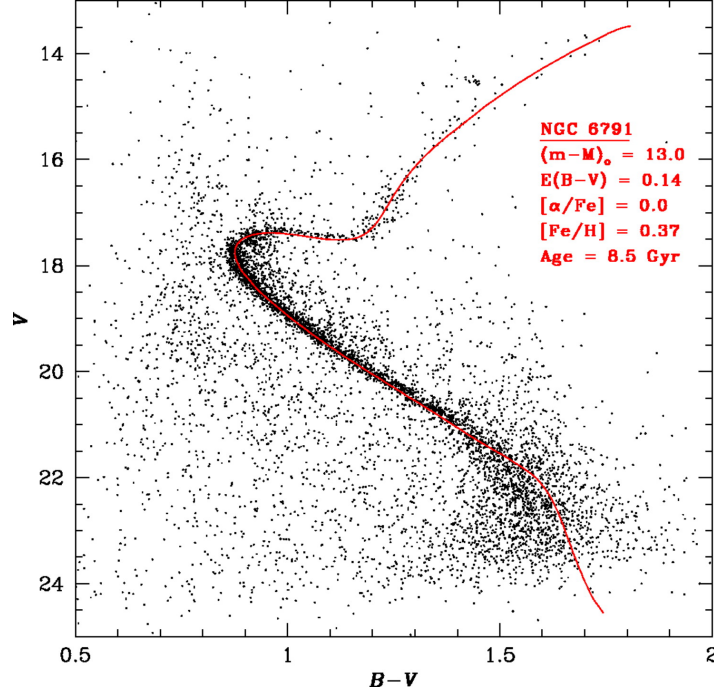


Figure 1.6: Color-magnitude diagram for objects observed in an area on the sky in the open cluster NGC 6791. The color excess  $E(B - V)$ , or interstellar reddening, along the line of sight to the cluster, the distance as described by the distance modulus having been corrected for extinction  $(m - M)_0$ , and the log of the relative number of iron atoms to hydrogen atoms as compared with the log of the Sun's value,  $[Fe/H]$ , were all pulled from the literature for the cluster. For each of the elements which are built from the addition of alpha particles to oxygen, the log of the ratio of the count of that element's atoms to the number of iron particles,  $[\alpha/Fe]$ , was presumed to be the same as that of the Sun. With these parameters, models of stars at 8.5 billion years old form the isochrone (shown in red) which is an excellent fit to the observed objects, identifying the cluster's age. Figure adopted from Kalirai et al. (2007).

from the ZAMS all the way through to the WD stage. While isochrones which cover the various stages of stellar evolution can be stitched together to do this, by focusing instead on WDs the final mass can be known empirically and the ZAMS mass can be derived from a semi-empirical approach (relying on the empirical observations, known cluster or systemic ages, models of stellar evolution to the AGB stage, and independent models of WD cooling).

Throughout this work we use what has been the most popular procedure, introduced originally by Sweeney (1976) and illustrated in Figure 1.7. In this method, the extra piece of information is the age of an open cluster, which is pulled from the literature. Cluster ages are obtained by fitting isochrones to the distribution of stars in each cluster as described in section 1.5. We then assume the WDs we have observations for are cluster members until our selection cuts suggest otherwise. This assumption is necessary as it is very difficult, perhaps impossible, to demonstrate with absolute certainty an object has evolved in an isolated fashion which is coeval with the open cluster it resides with. A series of tests of membership for our candidate objects show for which objects our assumptions are clearly false. We have then shown that our operating assumption is likely to be true for all other WDs in our sample, and go on to assume these are coeval members of their respective cluster which have evolved as isolated stars. We then invoke our extra piece of information by assuming that objects which have passed our membership tests are of the same total age as the open cluster. As the star’s cooling age can be modeled, we subtract the cooling timescale by which the object has been a WD from the total time the object has been in existence (the cluster’s age). This

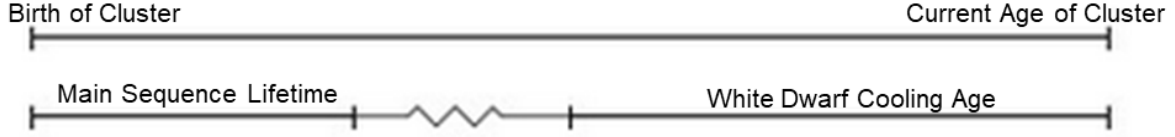


Figure 1.7: The total age of an object (bottom) and the age of it’s coeval cluster population (top). By assuming the object’s total age is that of the cluster and subtracting off the model cooling age the timescale by which the object was a star processing nuclear fuel is found. The nuclear lifetime is the sum of the main sequence and post-main sequence (trapezoidal line) lifetimes. Isochrones are used to convert the nuclear lifetime to the ZAMS mass of the object.

leaves the time the star existed as a nuclear burning entity (or as we will call it, the nuclear lifetime). Stellar isochrones are then used to map how long the object burned nuclear fuel for to derive the WD’s initial mass.

For studies of the IFMR accreting binary systems of all types are a possible source of contamination as the assumption that a WD has evolved in an isolated fashion is crucial to the derivation of the remnant’s initial mass. While an unseen companion must be fainter than the WD under study in the observed pass band to go undetected, there is a slew of stellar mass companions that are possible which include more massive WDs, M dwarfs, and neutron stars. It is unfortunately difficult to conclusively show that a WD is a single object without observations that are prohibitively costly in telescope time. However, the combination of the prevalence of binary systems and the frequency of these faint objects is low enough that with the sample size available today such contamination is likely to be few in number. Further, scatter introduced in the

initial mass by such binaries may be overwhelmed by sources of intrinsic scatter or unrecognizable through more dominant sources of error.

Extrapolation is known to potentially lead to inaccuracy, and as the IFMR is a tool for astronomy as a whole to use it is important to empirically cover as much initial and final mass parameter space as possible. In principle, the maximum extent by which initial and final mass data can be obtained over by using the Sweeney (1976) method is limited to the threshold by which objects evolve to WDs instead of undergoing core collapse at the high end and the age of the oldest stellar populations at the low mass end. However, the discovery of WDs in clusters over such a wide range of mass is challenging for a number of reasons. The WD mass distribution illustrates that few WDs exist at the greatest extent of the high and low mass tails. This suggests that a large number of WDs in clusters must be discovered to populate the parameter space at the extremum. Further, dwarf stars have low luminosities and at the distances of clusters often require a significant amount of large telescope time to get sufficient spectroscopic data for analysis. Moreover, after formation these remnants cool quickly and may fade below our detection limits. Despite the analysis contained in this dissertation, which includes the first study of the initial masses of newly identified objects in the open cluster M67, it is for these reasons the initial-final mass parameter space remains sparsely populated.

Globular clusters, being some of the oldest populations, have provided constraints down to  $\approx 12$  Gyr, or about  $0.8 M_{\odot}$  (Kalirai et al., 2009). At such an advanced population age the turn off mass evolves slowly and massive WDs have had enough time to cool below detection limits so in such clusters it is common to discover objects

in a very narrow range of WD mass. To further populate the IFMR at lower masses will require significant telescope time to examine objects in clusters with ages that further approach the Hubble time.

Open clusters, being generally younger in age, allow study of more massive objects. The best opportunity to both extend the empirical data to the highest mass possible for the IFMR and simultaneously bound the critical mass for core collapse supernovae from below comes from objects in the youngest open clusters, where relatively massive objects have barely had enough time to evolve to the WD stage but also have yet to fade below detection limits. Any particular cluster age tends to populate a fairly narrow mass range for these reasons. In slightly older clusters the most massive WDs may have faded below detection limits, but sufficient time has passed for slightly lower mass WDs to form. Thus, for a study such as this, that looks to reanalyze the IFMR in a consistent manner, it is necessary to sample many open clusters of various age to discover WDs which populate the entire parameter space. Regression can then provide IFMR, although future studies should still be wary of its use beyond the extent of the ZAMS mass extremum in the sample.

## **1.7 Historical Context of the Work of this Initial-Final Mass Relation Analysis**

Early studies which examined initial and final masses focused on testing stellar evolution rather than quantifying the IFMR (Sweeney, 1976; Weidemann, 1977; Romanishin & Angel, 1980; Anthony-Twarog, 1982). These sources both constrained mass loss

and the lower limit of core collapse supernovae. It was Weidemann & Koester (1983) that first fit the initial-final mass parameter space with a linear function.

Some later works have studied the IFMR using wide binaries. To examine the IFMR with wide binaries two things must be assumed. Firstly, that the two components of the binary are coeval. While this does seem likely, it should be noted that at present there is little empirical evidence to justify this assumption. Secondly, it must also be assumed the components have remained far enough apart to evolve without significant mass transfer. Then, objects have effectively undergone isolated evolution and one can apply isochrones to WDs if their system has a known age which can be used to derive nuclear lifetimes from which initial mass can be found with the use of models of stellar evolution. Different authors have applied different techniques, but all rest upon these two basic assumptions.

The initial and final masses have been studied for the nearby Sirius and Procyon binary systems (Liebert et al., 2005b, 2013). Both precise parallax and interferometric measurements allowed the distance, radius, and in turn the luminosity of Sirius A and Procyon A to be precisely known. In turn, with their metallicity from the literature their ages were derived using models of stellar evolution which was then adopted as the systemic age of each binary. The WD cooling age was then subtracted from the systemic age for the WD component in each binary to get the remnant’s nuclear age, which was then converted to the initial mass for Sirius B and Procyon B in either study. These authors did not use these results to derive the IFMR, but their measurements are notable for their precision and we have used some of the results of their work.

A different approach was used by Finley & Koester (1997) to extract initial and final masses for the wide double WD binary PG0922+162. A spectrum was obtained for both components, from which surface gravity, effective temperature and final mass for the remnants were found. The systemic age was derived by first identifying the two objects with known initial and final masses closest to the more massive component’s final mass. The ZAMS mass of the more massive binary component was then found from a linear extrapolation of the initial and final masses of those two objects out to the final mass of the more massive WD in the binary. Its nuclear lifetime was then found with evolutionary models, and its cooling age was co-added to the object’s nuclear lifetime to derive the timescale of the object’s total existence. This was adopted as the systemic age for the binary. The cooling age of the less massive WD was then subtracted from the derived systemic age, and the initial mass of the second binary component was found. Through relying on extrapolation from a linear fit of just two data points the systematic accuracy of this approach leaves something to be desired. The application of an IFMR derived from many objects would be free of such dependencies.

Approaching the IFMR with wide double degenerate binaries was later revisited by Andrews et al. (2015). In this work the IFMR was derived using a sample of multiple wide binaries. A set of 19 binaries were identified, and a new Bayesian framework was used to simultaneously fit a solution. However, their results failed to match up with the initial and final masses of WDs in previously studied open clusters. At present it seems likely the use of wide binaries to derive the IFMR is not sufficiently developed as the historic procedure of Sweeney (1976) invokes much of the same physics while using



independent measure of total stellar (e.g. cluster or binary systemic) age. Further, theoretical IFMRs tend to agree more with the results from open cluster studies. Future work examining the systematic accuracy of the techniques which use either open clusters or wide binaries is certainly warranted.

While WDs in globular clusters have been studied, only Kalirai et al. (2009) has derived initial masses for such objects. M4 is such an old cluster that the WD cooling ages for remnants which are yet to fade below detection limits are small with respect to the total cluster age, and so it was assumed that the nuclear lifetime of each WD in the cluster was that of the cluster age. Therefore it was suggested by Kalirai et al. (2009) that the six cluster WDs identified had the same nuclear lifetime and initial mass. This procedure differs from the method of Sweeney (1976) only slightly with an assumption that is reasonable, but one of which introduces a small systematic error. A reanalysis which excludes this assumption and derives the nuclear lifetime of each WD to get the initial mass of each object using the full method of Sweeney (1976) would be both appropriate. This would be important for extending the coverage of low mass end of the IFMR.

More extensive work has been done on the IFMR with WDs in open clusters (see Kalirai et al. (2008) and references therein for a review through that time). Prior to the work of Kalirai et al. (2008) the present day turn off mass of the oldest studied open clusters was  $\approx 2.75 M_{\odot}$ . Kalirai et al. (2008) extended this down to  $\approx 1.16 M_{\odot}$  with the inclusion of WDs in the open clusters NGC 7789, NGC 6819, and the metal rich 8.5 billion year old NGC 6791, using a linear function to model the IFMR as most

previous studies had done.

To this point in time it has been unclear if a linear function is appropriate to describe the relationship between initial and final mass. Amongst other authors, Andrews et al. (2015) suggested that the relation would be best described by a piecewise function. Motivated by models of stellar evolution which predict two transitions where the physics that governs a star transforms, they proposed that it is appropriate to break a linear IFMR into three segments. Below a ZAMS mass of about  $2 M_{\odot}$  stars process hydrogen into helium at first in the core, and then in a shell around an inert helium core supported by degeneracy pressure. Eventually physical conditions are such that helium begins to fuse, and with increase in temperature a runaway quickly precedes which leaves carbon as a product in the core. Above this mass, rather than building a degenerate helium core physical conditions are sufficient for helium to burn steadily into carbon. Models predict this transition has a noticeable effect on the object's final mass. The second transition occurs around a ZAMS mass of  $4 M_{\odot}$ . Stars more massive than this transition experience what's called second dredge up. In the later stages of stellar evolution deep convection driven by hydrogen and helium shell burning around a carbon core increase both the opacity of the atmosphere through chemical enrichment and the efficiency of energy transport. With the accompanying shift in the star's equation of state models predict the final mass of these objects will be stunted.

The IFMR may be more sophisticated than this as secondary effects may combine with model systematics and uncertainty in cluster age to form complex behavior and degeneracy. It is clear that the initial and final masses are primarily dependent on each

other and are positively correlated. However, systematic shifts in each cluster age can also push all of the initial masses for objects in each cluster up or down at amounts which are sensitive to each object’s corresponding stellar lifetime. Complicating this, is that scatter in the relation may be introduced by differences which effect mass loss and in turn core growth, including metallicity, magnetic fields, rotation, or close binary pollutants (Dominguez et al., 1996; Kalirai et al., 2007). Scatter may also be introduced by a lack of internal consistency with the models employed (Salaris et al., 2009). It has often been the case that the isochrones used to fit the cluster color-magnitude diagrams to derive the age of the population and those used to derive the initial masses do not yield the same core composition at the WD stage as the cooling models employ for the composition of the WD. Perhaps more importantly, the set of isochrones used to derive the age of the cluster have often not been the same as those used to map the nuclear lifetime of the progenitor star to initial mass. Taking various dependencies into account, it is quite possible that the relationship between initial and final masses is not one-to-one.

Paramount to these issues however, is that current measurements of initial and final mass are not precise enough to decipher any of the effects which may be contributing scatter about the relation. This is true even for studies which have been internally consistent, where considerable attention has been payed to using consistent sets of models to minimize systematics. The errors are simply too large to conclude with confidence that any of the more subtle effects on mass loss are present, much less at what level they contribute.

One recent development has shown that, at least for objects near an initial mass of  $1.5 M_{\odot}$ , secondary effects aside from metallicity do not significantly contribute to mass loss. By examining one cluster where both cluster age and metallicity are fixed, additional dependencies on the relationship between initial and final mass can be explored. Some of our recent work has done just this (Williams et al., 2018). The new M67 WD sample has derived from such an old cluster that the remnants above the detection threshold which have had time to evolve to the WD stage are from virtually the same initial mass. In this sense, the primary dependency (initial mass) on final mass was removed, as was metallicity by virtue of all the objects having evolved in a coeval sense in the same open cluster. The variance in the mass distribution of WDs was found to be nearly the typical error in the calculated WD masses. A lack of any variation in WD mass from a sample of fixed metallicity and initial mass suggests that, to within errors, secondary effects beyond metallicity have not played a significant role in the integrated mass loss from these objects. While the M67 sample shows this is the case near  $1.5 M_{\odot}$  this conclusion may not hold at higher or lower masses. Still, we will follow these results and make the assumption that secondary effects on mass loss play a limited roll and we will not investigate any effects of scatter in the IFMR beyond metallicity.

## 1.8 The Scope of this Dissertation

In this work I will present a derivation of the IFMR from all of the available objects in the literature for which a consistent set of models has been applied. By ensuring

the same set of stellar evolution models are used to derive the cluster ages as are used to map effective temperature and surface gravity to initial mass we avoid introducing intangible scatter where possible. To that end, we have also been careful to only include objects which use the same spectroscopic models in our sample. However, the models of stellar evolution we employ to derive the ZAMS mass have some particular core fraction of carbon and oxygen. This value does not match the carbon and oxygen fraction our WD cooling models adopt. While this systematic is small, it is difficult to control as the available WD cooling models and stellar evolution models are written by different external groups.

We have been able to populate the initial-final mass parameter space from 1.17 to 7.22  $M_{\odot}$  in initial mass and 0.50 to 1.18  $M_{\odot}$  in final mass. In our process we present the discovery and analysis of a new sample of WDs in NGC 2682 (M67), and our reanalysis of WDs from NGC 1039 (M34), NGC 2168 (M35), NGC 6633, and NGC 7063 with the latest models. From the literature we have included only additional WDs which maintain internal consistency as described. Included in our sample are objects from NGC 2099, NGC 2287, NGC 2323, NGC 2516, NGC 3532, NGC 6791, the Pleiades (M45), and the Hyades. We also include Sirius B, as it has a well determined system age from studies of Sirius A.

Most authors have historically illustrated error bars in the initial and final masses for each object along their respective axes. While this approach can illustrate the asymmetrical errors in initial mass which derive from the use of isochrones to map surface gravity and effective temperature to initial mass, it is a poor way to illustrate

the form of the uncertainty of each object in initial-final mass parameter space. It also brushes correlation between the initial and final masses under the rug. In this work we illustrate how the uncertainty is distributed for our sample through Monte Carlo simulations, presenting the IFMR in a way that has never been done before. Having explored the errors in both initial and final masses by varying the input parameters, we then derive the IFMR by applying an unweighted linear fit to all of the Monte Carlo simulation trials.

For clarity later, I will clear up some terminology here. I use the terms evolutionary models and cooling models to refer to the same thing. As has been done throughout this chapter I refer to the ZAMS mass as the initial mass, and to the mass as a WD as the final mass. Lastly, I will continue to refer to an object as a star only while it is supporting itself by nuclear fusion in its interior. It is common to speak of WDs as stars, but they are instead the remnants of stars. Such precise terminology is more accurate, and will also alleviate significant confusion as we later discuss epochs of the objects in our sample both before and after they have become WDs.

In chapter 2 we discuss the observations and how we obtain the masses of WDs in our sample. In chapter 3 we prune our sample of field objects to obtain a sample of WDs which are likely isolated and coeval cluster members. In chapter 4 we derive the initial masses for this sample and discuss the IFMR analysis. Finally, in chapter 5 we summarize our major conclusions and suggest future work.

## Chapter 2

# Masses of White Dwarfs

The mass of a WD represents the difference between the ZAMS mass of an object as a star and the star’s integrated mass loss over the course of stellar evolution. Through simplicity, such as the lack of an internal source of energy production and stratified layering due to gravitational settling, applications for these objects have been found which influence a wide variety of subfields in astronomy. Therefore the mass of a WD, a fundamental quantity, has far reaching effects when it is precisely known.

## 2.1 Methods by which White Dwarf Masses can be Obtained

As it is impossible to go to the location of the WD and put it on a scale as one would in order to measure any typical lab sample, we instead must rely on techniques which use the electromagnetic radiation that reaches us. There are multiple ways the masses of WDs may be obtained, although each has its own limitations and they do not all result in agreement (Bergeron et al., 1995a; Genest-Beaulieu & Bergeron, 2014).

Perhaps the most precise method for obtaining a WD’s mass is through observing its orbital motion in a resolvable binary. Kepler’s third law allows for the conversion of the orbital period, an observable quantity, to the component masses. Notably, the results of this technique are independent of models which involve the physical descriptions of either object. However, the main disadvantage of the technique is that the system must be resolved, meaning nearby, and it can take years to obtain the required data to

measure the orbital period. As such, using this technique to derive WD mass is only possible for a few known objects.

Masses have also been derived for a handful of WDs which exhibit rich spectra of pulsation modes. In certain regimes of temperature and surface gravity pulsation modes in the spherical geometry of the object are excited which can be observed as periodic variations in brightness (Winget & Kepler, 2008; Gianninas et al., 2015). Photometric observations reveal this change in brightness with time, and a Fourier transform in the time domain readily reveals what pulsation periods are present in the frequency spectrum. Stellar models are then compared to the observed frequency spectrum, and physical properties such as mass are inferred. The use of this technique is however restricted by the fact that the range of parameter space in which WDs pulsate is small.

Another technique for deriving the mass of a WD is by measuring their gravitational redshift (Barstow et al., 2005; Falcon et al., 2010). The observable quantity is a shift of the absorption lines towards longer wavelengths in the object’s spectrum, where the amount of shift is indicative of the object’s mass. This technique requires a high signal to noise spectrum, and resolution such that the center of absorption lines can be determined with high precision. It also requires that the remnant’s radial velocity with respect to the observer is known. Without a binary companion or some comoving group with the WD, such as an open cluster, the effect of Doppler shift and gravitational redshift are impossible to disentangle. This technique also has the advantage that it is model independent, but the prior requirement restricts its practical use.

Recently, the mass of the WD Stein 2051 B was found by studying how the relativistic



deflection of a background star to this remnant changed with time (Sahu et al., 2017). This work was only possible with the precision of the Hubble Space Telescope, and given such chance alignments are rare the use of this technique is limited. Nevertheless, it has an advantage over some other techniques in that it can be used to yield a precise mass measurement in the case of a DC spectral type WD, as is the case of Stein 2051 B.

The photometric method is one of the most widely used techniques for deriving the mass of WDs. Its advantage lies in that it can be applied for any WD for which photometry is available in multiple band passes. A model spectrum of a WD is integrated over each bandpass and a correction for distance is made in order to predict the flux in each filter, which is then compared to the observed values by calculating a  $\chi^2$  statistic. Once a minimum for the statistic has been found the effective temperature and surface gravity of the best fit model is adopted as that of the WD, and then used to derive the mass of the remnant through the mass-radius relationship. This approach is not always the most precise, particularly at temperatures above 20,000 K as the Balmer jump weakens. Further, unless distance is known it cannot be certain that an object is in fact a WD.

In this dissertation we employ the spectroscopic method to derive WD masses. This process is described in more detail in the context of our work in section 2.3.3. Typically, a series of models which describe a WD’s atmospheric physics is generated over a range of parameter space, and then compared to observed spectra to reveal which model is the best approximation of the true physics of the remnant’s atmosphere. The best fitting model is then taken as a physical match to the atmosphere of the WD, and we adopt

the model’s surface gravity and temperature as that of the remnant’s. Then, the mass of the WD is readily found through a mass-radius relationship with some assumption with regards to core composition (see section 1.3).

As with other techniques, the spectroscopic method has both its advantages and limitations. By spreading light out into its constituents spectroscopic observations of sufficient quality require more telescope time to obtain the same signal-to-noise, but are especially valuable as they allow for unambiguous identification of WDs by their absorption line profiles (because of their high surface gravities, WDs have very broad lines). Furthermore, hydrogen Balmer lines are detectable from a few thousand to more than 100,000 K, allowing for the determination of effective temperature and surface gravity through this technique for most WDs (Wesemael et al., 1993).

While examples of the application of the technique can be found for cool and hot stars at these extremes in Wesemael et al. (1993) and Gianninas et al. (2010), we examine the sensitivity of this technique with the following illustrations. Figure 2.1 provides an illustration of the sensitivity of the technique at lower temperatures. The equivalent width, or a measure of area, of the  $H\alpha$  absorption line for a sample of DA WDs as a function of color, which is a proxy for effective temperature, is displayed. Bluer, or hotter objects, are to the left. The downturn in the trend near  $V-I \approx 1.0$  mag., which is around 5,000 K, illustrates that for objects warmer than this temperature the equivalent width is sensitive to temperature until at least 7,000K ( $V-I \approx 0.4$  mag.), while below this the sensitivity disappears completely. Figure 2.2 illustrates the continued sensitivity of the absorption lines at higher temperatures, albeit for lower mass remnants

( $\log g = 6$ ). The differential of equivalent width with respect to temperature is a measure of how sensitive an absorption line is to temperature (this is the slope in Figure 2.1). Where the magnitude of the differential deviates from zero the most the lines are the most sensitive to temperature, and in turn the physical parameters can be the most precisely determined. This nicely illustrates just how the sensitivity of an absorption line changes with effective temperature beyond the range of Figure 2.1: From 8,000 to about 11,000 K the absorption lines are all quite sensitive to temperature. Beyond 11,000 K the sensitivity peaks around 12,000 K, before falling off with a long tail. An extension of this figure to much higher temperatures would likely show this trend continues, with sensitivity approaching zero, until the Balmer lines disappear completely due to depletion of the population levels by ionization at high temperature. It can be seen that at the peak line strength, in a very small region near 11,000 K, the sensitivity does go to zero (Gianninas et al., 2014). For models with  $\log g = 8$ , as was the case in Figure 2.1, the pattern of sensitivity is similar but the peak line strength shifts to  $\sim 13,500$  K, although this is sensitive to the parameterization of mixing-length theory which is used to describe convection (Fontaine et al., 2003; Gianninas et al., 2014; Bergeron et al., 1995b). Nevertheless, the spectroscopic technique can be used to derive precise masses of WDs over an incredibly broad range of temperatures.

The sample of DA WDs examined in this dissertation are well within the temperatures for which the physical parameters are sensitive to the line shapes. It is for this reason it is sufficient to examine our objects using the spectroscopic technique alone. While this technique can also be applied to WDs of other spectral types, the DB WDs

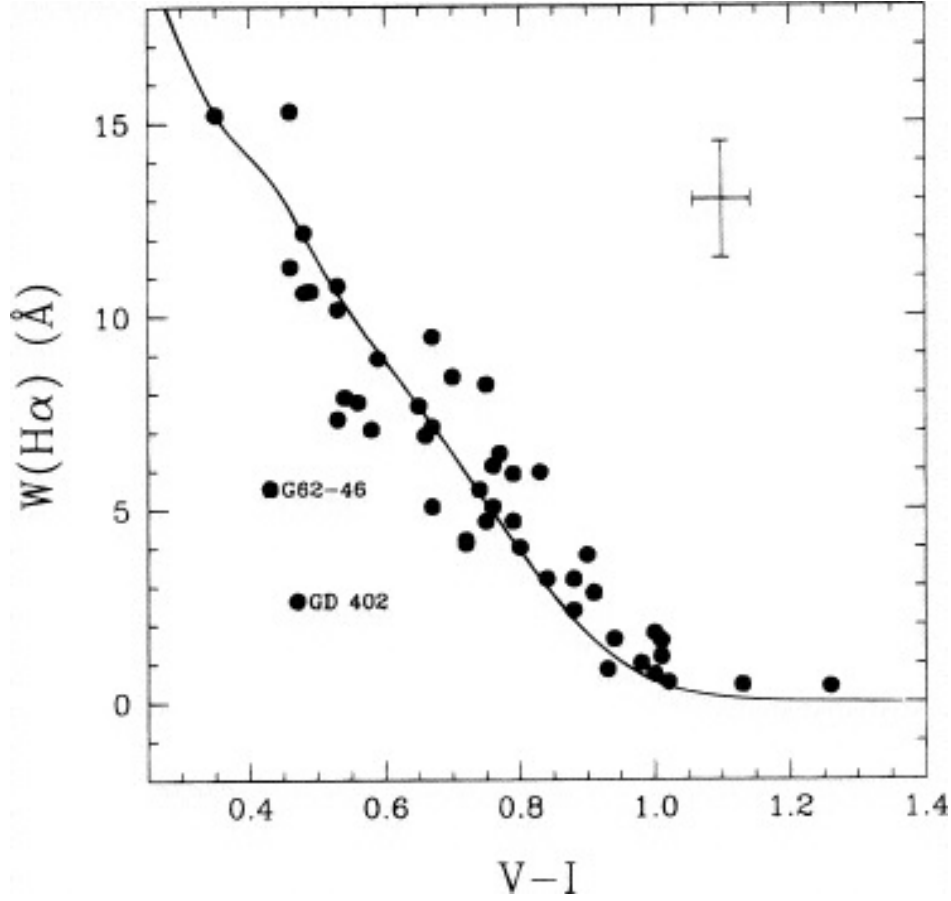


Figure 2.1: Equivalent width of the  $H\alpha$  line as a function of color for a sample of DA WDs. The solid line depicts model predictions for  $\log g = 8.0$  WDs. The outliers, G64-46 and GD 402 are unresolved double degenerate binaries. Typical uncertainty for the WDs is denoted in the upper right. A nonzero slope, such as to the left of  $V - I \sim 1.0$  mag., illustrates for what color (or temperature) this Balmer line has at least some sensitivity to temperature. Figure adopted from Bergeron et al. (1997).

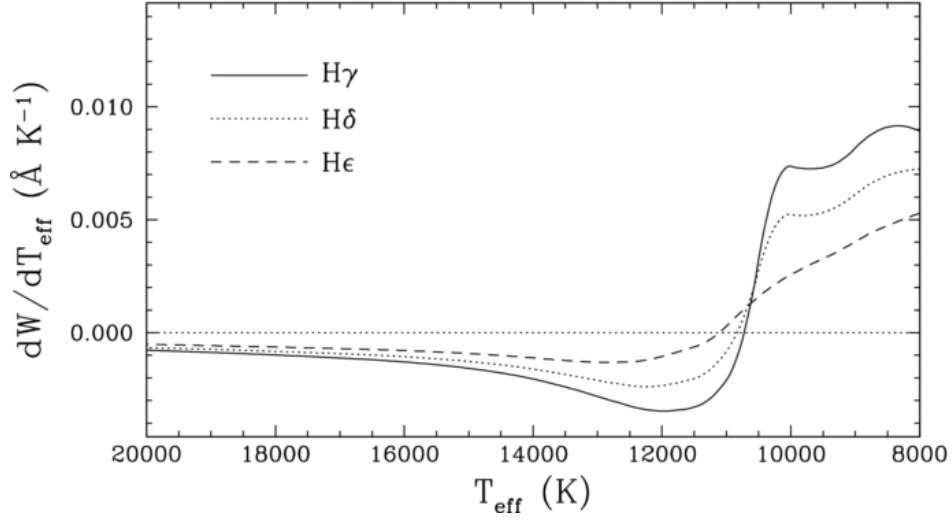


Figure 2.2: Derivative of equivalent width with respect to temperature of the  $H\gamma$ ,  $H\delta$ , and  $H\epsilon$  lines as a function of effective temperature for models of low mass ( $\log g = 6$ ) WDs. The amount of deviation from zero illustrates how sensitive equivalent width of each line is to temperature at that particular temperature. Figure adopted from Gianninas et al. (2014).

observed in the clusters studied herein will be included in a future analysis.

## 2.2 On Theory of White Dwarf Spectral Energy Distributions

To derive the mass of a WD using the spectroscopic method one must pick a set of physical models which predict the remnant's spectral energy distribution. By iteratively comparing one of these models to an observed spectrum until the model which fits the data best has been determined, we shift through many possible sets of surface gravity and effective temperature before we have identified our best guess as to the true physical parameters of a WD. The last step in the process is to simply map the physical parameters of the best fit model to the mass of the WD through the mass-radius relation (section 1.3).

The choice of models used for comparison with each observed spectrum has an effect on the physical parameters identified with the WD. Simplistic models are often used as they are computationally inexpensive or easy to understand. For a quick measure of full width at half maximum a Gaussian is often used to describe one line profile at a time, but such a method has no physical underlying description so the models used to obtain any kind of real physical understanding must be more complex. A physicist might think to use a series of black-body emitters to find an appropriate physical model. Such predicts the continuum shape is a function of effective temperature alone, and so the temperature of the best fit model identifies the temperature of the object in question. This description can be appropriate for an optically thick object, but in truth such a model provides a less than perfect fit to observed spectra of stellar objects. One

reason is the fact that temperature is a function of depth in these objects. Thermalized photons experience their last scatter before escaping the object from various depths, so the black-body emitter assumption of thermal equilibrium across the emitting volume is not valid. Being sensitive to just temperature, black body descriptions also lack the ability to measure mass as they are not sensitive to surface gravity.

From the spectrum of a WD careful study of the absorption line profiles can provide precise measure of both temperature and surface gravity, and so it is generally preferred that the complex physics of these objects be taken into account. Both temperature and surface gravity are state variables - on a macroscopic scale we cannot follow every photon-atom interaction and so we look to state variables which statistically describe the atmosphere as a whole. Models examine the microphysics in order to make predictions about state variables which give a macroscopic view. An excellent fit can often be found using a full physical description of the atmosphere which takes into account the various microscopic broadening and opacity effects discussed below. As the absorption lines take center stage, the line profiles are normalized to the continuum level to isolate the physics from which the line opacities derive. These include ‘bound-bound’ and ‘bound-free’ opacities, in reference to if the electron undergoing a transition has been ionized or is confined to one of the absorbing atom’s energy levels. As continuum light from deep within the star passes through the atmosphere atoms preferentially absorb photons, resulting in deficiencies of flux in the spectrum at particular wavelengths. However, it is the physics of the broadening effects which give the absorption lines their shape. In our work we have employed models which include such physics to obtain the

most accurate masses possible for each WD in our sample.

### 2.2.1 Natural Broadening

A photon which passes by an atom in the atmosphere applies a time dependent perturbation to the atom. A time-dependent approach to perturbation theory allows for an analytical solution of such (Griffiths, 1995, Chapter 9). The probability an atom will absorb an incoming photon depends not only the time of arrival of the photon but on the frequency of the photon. The distribution of this probability about the line center is symmetrical, with the greatest chance of absorption at the frequency characteristic of the transition energy. In other words, even in the hypothetical case where the energy levels are exact a photon need not be exactly of the characteristic energy of an atomic transition to be absorbed, however it has a higher likelihood of being absorbed if this is the case (Griffiths, 1995, e.g. Figure 9.2). Indeed, when integrated over the width of a spectral line this probability gives rise to the famous Einstein A and B coefficients, which describe the total rate at which electrons undergo such a transition. In short, line broadening is one prediction of quantum mechanics.

The time-energy uncertainty principle, however, provides a natural limit for the minimum width a spectral line can have (Hubeny & Mihalas, 2014, Section 8.1). The absorption line profile that results from this follows a Lorentzian distribution, which is also symmetrical about the line center. While natural broadening is apparent in all atmospheres, the amount of broadening is so small it is not resolvable with moderate resolution spectra in the optical which we examine in this work.



### 2.2.2 Doppler Broadening

Particles in the atmosphere are in motion in random directions and so light from the region we observe is Doppler shifted both to the red and the blue. While the atmosphere has some temperature structure to it, it is often a reasonable approximation to assume thermal equilibrium across the photosphere. A Maxwell-Boltzmann distribution can therefore be used to describe the particle speeds. Bulk motion, such as that of convection in the atmosphere, mass loss, or rotation, all have additional contributions to Doppler broadening. The absorption profile characteristic of Doppler broadening is that of a Gaussian distribution, which falls off faster than a Lorentzian distribution such that this effect dominates the core of the line profiles.

### 2.2.3 Pressure Broadening

The spectroscopic technique depends heavily on the physics of pressure broadening as it is the dominant broadening effect in WD atmospheres. Sometimes called collision broadening, pressure broadening effects pertain to external electric perturbations applied by a passing particle on an absorbing atom. Ions and free electrons in the atmosphere contribute to this effect, as do readily polarizable atomic species such as hydrogen.

The presence of an external electric field on any particular absorbing atom splits the degeneracy of that atom's energy levels. As charged particles in the vicinity of an absorbing atom move about the strength of the electric potential on that atom, or the amount by which the states are split, is function of time. The transition energies for one absorbing atom are therefore also time dependent, although they are discrete.

Therefore, when averaging over both time and many absorbing atoms, absorption over these discrete transitions spans what is effectively a continuous range of wavelengths. The result is a broadened spectral line in absorption.

The external electric field can be provided by either a charged particle in the case of the linear stark effect (in which the energy shift is linear with the electric field) or a polarized atom in the case of the quadratic stark effect. As such, in the hotter WDs the linear stark effect tends to dominate the broadening of the profile, whereas for cooler WDs a larger fraction of the atmosphere is atomic and the quadratic effect becomes more significant. Composition also plays a role as Hydrogen has a permanent dipole moment so DA atmospheres tend to be characterized by the linear stark effect rather than the quadratic stark effect even at lower temperatures. Further, in the more dense atmospheres of more massive WDs neighboring particles tend to pass closer so the applied external electric field on each absorbing atom is of greater strength, resulting in broader line profiles (except in the case of line quenching for the higher order line transitions, see below). As with natural broadening, the line shape due to pressure broadening is a Lorentzian distribution (Hubeny & Mihalas, 2014).

The exact physical description from which the line profiles derive continues to be the topic of ongoing research. As the state of the art continues to progress the masses derived in previous IFMR work has now become obsolete, which serves as motivation for the reanalysis of WDs in four of the open clusters we study herein. Some of the relatively recent progress was discussed in Tremblay & Bergeron (2009), whose models originate from Bergeron et al. (1992a). Bergeron et al. (1992a) recognized that the

physical parameters for the best fit model spectrum had some dependency on which lines were used to determine the fit. The top panel in Figure 2 of Tremblay & Bergeron (2009), illustrated here in Figure 2.3, shows how the parameters were found to drift with earlier models. As a WD has one set of true physical parameters there should be no such dependency. The fact that the drift was significant implied that the line physics was in need of refinement. Bergeron (1993) traced the issue back to nonideal gas assumptions in the calculation of stark broadening profiles (e.g. that inelastic collisions need to be accounted for), and in an ad hoc sense doubled the field strength defined by the minimum perturbation strength for which electrons in any particular energy level would be ionized (the critical ionizing field) as an unphysical solution to the issue. In Tremblay & Bergeron (2009), the equation of state of Hummer & Mihalas (1988) (a notable departure from earlier ideal gas models) and the theory of stark broadening of Vidal et al. (1970) were combined to compute the effect of pressure broadening. The bottom panel illustrates that this physical approach alleviates much of the drift, although there still may be some present.

The result of the Tremblay & Bergeron (2009) description is that, with respect to the old profiles, the updated models tend to yield both hotter temperatures and higher surface gravities by about 1000-2000K and about 0.1 dex respectively, as can be seen in Figure 2.4. We briefly discuss how the physical parameters for massive WDs have changed in light of the more recent models in chapter 5 as they are of particular interest. The opacities in this prescription, both bound-bound and bound-free, are shown in Figure 2.5. The line opacity that results in bound-bound transitions are illustrated

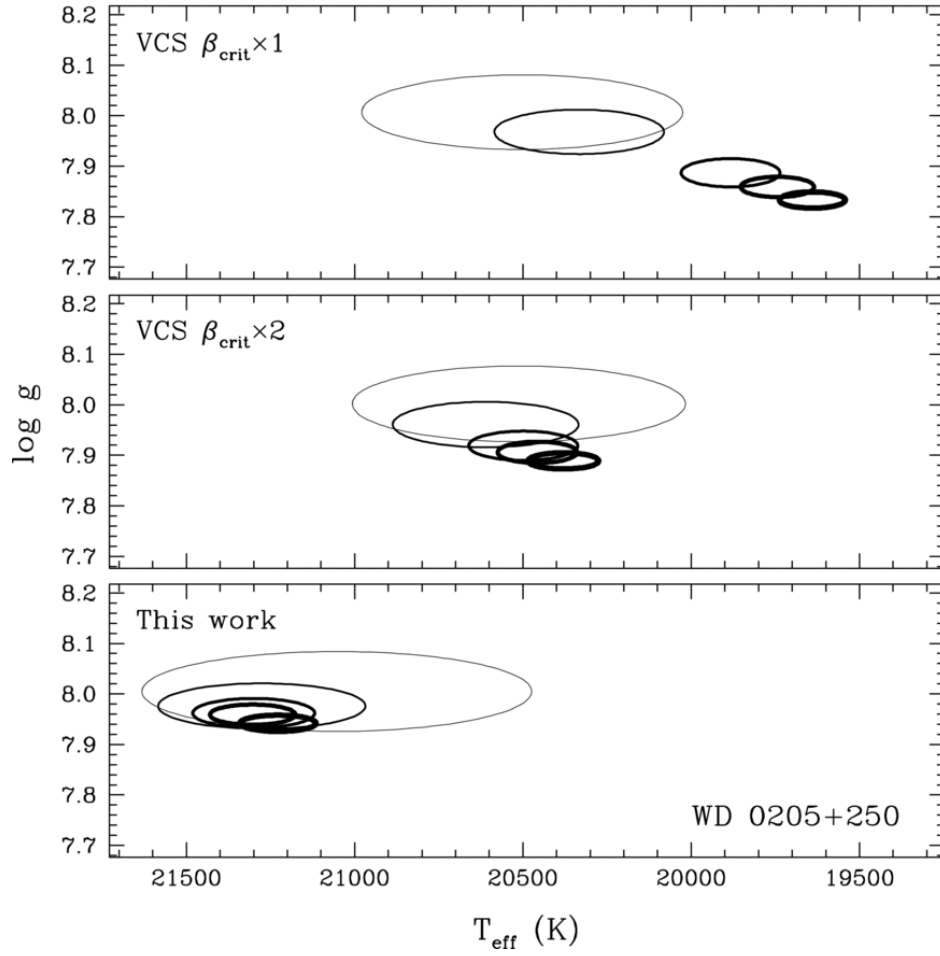


Figure 2.3: Physical parameters for a typical DA WD by deriving a fit from 1 line ( $H\beta$ ) up to 5 lines ( $H\beta$  through  $H8$ ). The fitting procedure errors are described by  $1\sigma$  contours. The top panel shows drift with the Vidal et al. (1970) calculations is large enough for the results to be significantly different when various lines are used in determining the best fit. The middle panel describes the amount of drift using twice the value of the critical field as suggested by Bergeron (1993). The lower panel illustrates that the updated physics resolved the issue as the physical parameters for a WD using the models are now statistically consistent no matter how many lines are considered. Figure adopted from Tremblay & Bergeron (2009).

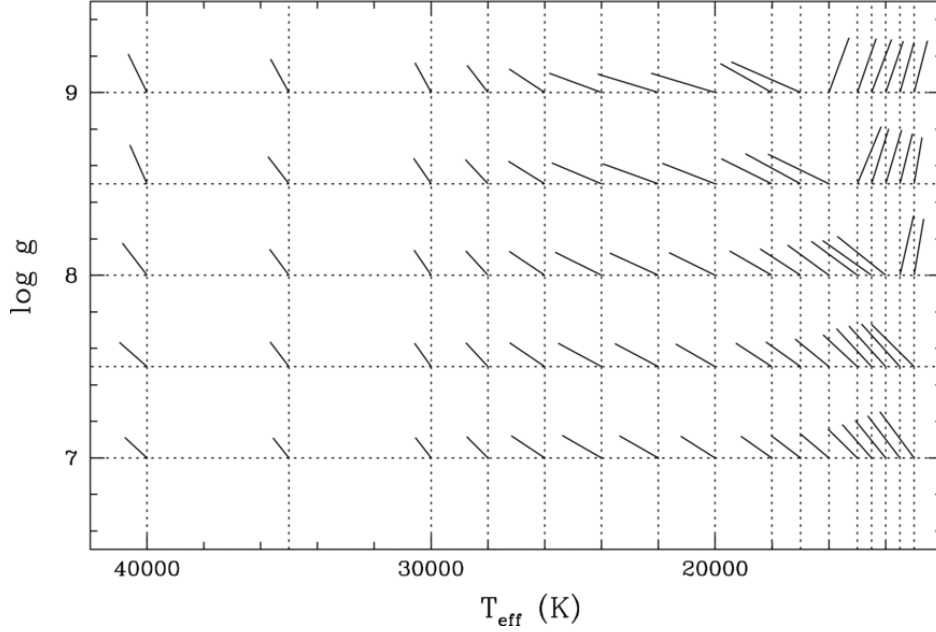


Figure 2.4: Shift in physical parameters of the Tremblay & Bergeron (2009) models to those obtained using the Vidal et al. (1970) profiles. The grid points center on the VCS prediction and the updated results generally move towards hotter temperatures and higher surface gravities. Figure adopted from Tremblay & Bergeron (2009).

in solid black, where peaks are indicative of absorption line centers. Although the bound-bound opacity in between the lines is nonzero, in these regions the so called pseudo-opacity (dotted line) dominates.

As does the broadening of each of the lines, the pseudo-opacity also arises from electric perturbations on the absorbing atoms. As stark broadening splits degenerate energy levels, energy levels of the higher order lines will cross if the perturbations are large enough, either forming one degenerate state or elevating a state of lower principle quantum number ( $n$ ) above the next higher ( $n+1$ ) such that electrons can freely transition from lower to higher levels. If the lower and higher energy levels have

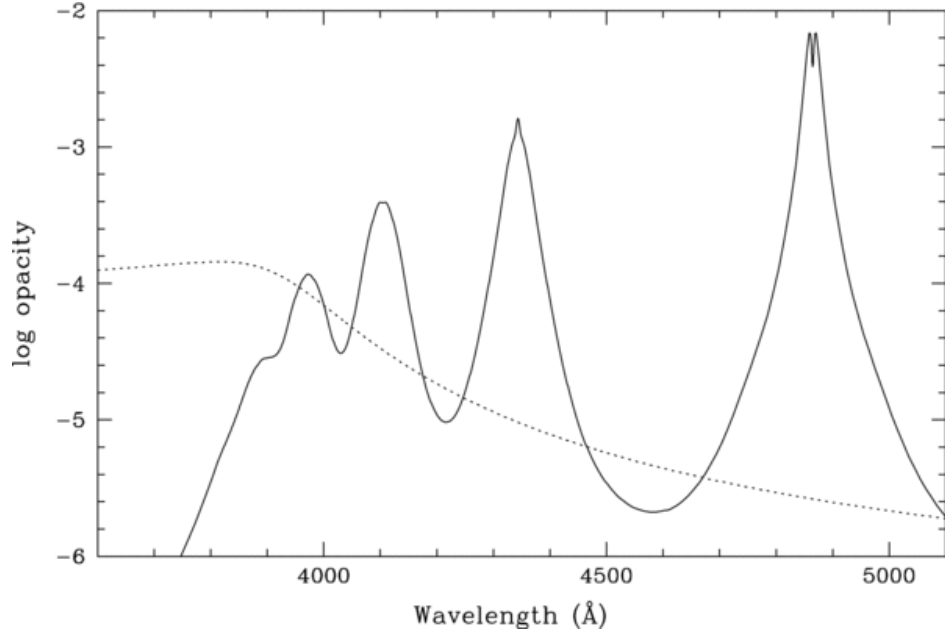


Figure 2.5: Opacity as a function of wavelength for a 20,000K WD. Absorption line centers are located where the bound-bound opacity peaks (solid line). By contrast the pseudocontinuum opacity that arises through pressure ionization acts as a continuum opacity source (dotted line). Figure adopted from Tremblay & Bergeron (2009).

crossed, the line wings will have some opacity due to both transitions in the adjacent wings, and there will be some overlap between the two adjacent lines in the spectrum. Over the ensemble of absorbing atoms, each under a haphazard perturbation strength that changes in time as perturbing particles move about in the plasma, photons of any energy from the lowest overlapping states all the way up to the ionization level can be absorbed. In effect, the sum of many bound-bound transitions amongst all the overlapping line transitions effectively forms a continuum opacity source.

Of the states that are split to higher energies some will extend beyond the ionization energy. Transitions to these states do contribute to the continuum opacity as is typical of bound-free processes: An electron undergoing such a transition becomes ionized leaving the atom with some kinetic energy equivalent to the difference between the photon's energy and the ionization energy less the energy of the lower energy state from which the electron began. As continuum opacity arises from both above and below the ionization level, the ionization potential is effectively lowered. Physically, this may come about as once an electron is in an overlapping state it can wait for a time when the degree of external perturbation allows for a transition between degenerate states, possibly ascending to ionization. While this is sometimes called pressure ionization it should be stressed that the bound states do still exist and that the ionization level is not actually lowered. Rather, that it is only lower in an effective sense. Likewise, the appearance of a continuum opacity is the culmination of a great number of bound-bound transitions rather than a conduction band as some have metaphorically referred to it.

Whether this physical description is accurate continues to be explored. It was

once thought that at high densities the lines grew so broad that their profiles were so shallow they were simply lost in the noise of experimental data. While thermodynamic approaches have used statistics to describe the lowering of the ionization potential by the use of occupation probability formalisms (such as Hummer & Mihalas (1988)) some current calculations are revisiting pressure broadening with quantum mechanical treatments which solve for the atomic structure in the presence of many ions (Gomez, 2017). As these calculations incorporate perturbations due to neighboring protons they are inherently N-body simulations which push the limits of our current computational capabilities, but such a sort of brute force solution to Schroedinger’s equation may yield new physical interpretations of line quenching. Indeed, whether line quenching derives from ionization through which the bound states are actually destroyed or if the lines simply become too broad to distinguish is still hotly contested.

For an astronomer looking to refine the IFMR there are a few simple takeaways. It should simply be noted that line quenching is highly sensitive to, and therefore an excellent indicator of, WD mass through surface gravity. This illustrates the importance of getting the physical model right, but it should also be kept in mind that significant systematic differences can be apparent in physical parameters for any spectrum simply due to the use of different physical models (this is sometimes referred to as the external fitting error). Finally, line quenching does seem to come with a noticeable effect on color, an observable which suggests there truly is an additional source of continuous opacity with the subsidence of the higher order lines (which models predict, e.g. by the slope of the psuedocontinuum opacity as a function of wavelength in Figure 2.5). What is



clear from both laboratory experiments and astrophysical observations is that the higher order lines disappear at high density due to the effects of pressure broadening, and efforts to find a physical model which perfectly describes our observations of plasmas in these conditions are ongoing.

#### 2.2.4 Absorption Line Profiles

A description of the line physics is incomplete without a qualitative illustration of the absorption line profiles themselves. Generally, the shape derives from Doppler broadening in the cores (Gaussian) and follows pressure broadening (Lorentzian) in the wings. Whereas effective temperature governs the energy level populations, surface gravity plays an important role in both line width and, in the case of the higher order lines, depth. The absorption lines of WDs are noticeably wider than for main sequence stars. Figure 2.6 illustrates the line profiles as a function of both effective temperature and surface gravity. The Hydrogen Balmer series is displayed with the wavelength regions of interest about each line center offset vertically for clarity. Typically there is some slope to the continuum due to the color of the object, but here the continuum slope has been normalized across the absorption line at each wavelength bin. The equivalent width of the lower lines ( $H\beta$  and  $H\gamma$ ) increase with surface gravity through the linear Stark effect at higher pressure, while the higher order lines ( $H\delta$  and higher) decrease in strength with increasing surface gravity due to the effect of pressure ionization, line quenching, in which the highest order lines disappear first. Hence the use of fitting many Balmer lines simultaneously can not only identify where the models could benefit from improved physics, but can be used to precisely determine the physical parameters

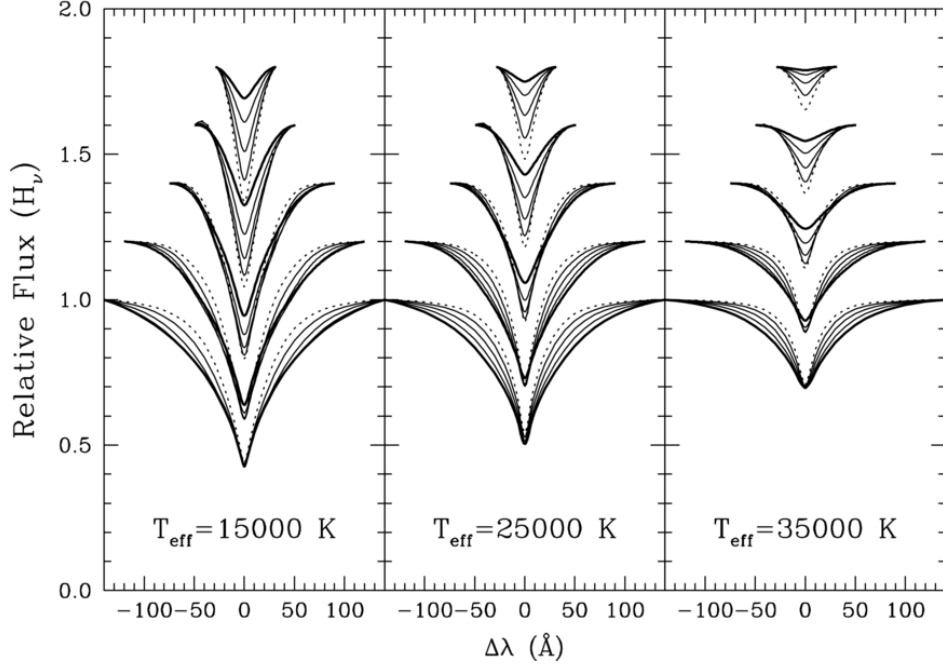


Figure 2.6: Theoretical line profiles, normalized to the continuum level and offset by an arbitrary constant for clarity, of the  $H\beta$  (bottom) to  $H\delta$  (top) lines for models at different effective temperatures and surface gravities. Temperature is fixed in each panel, increasing left to right, while the logarithm of the surface gravity varies from 7.0 (dashed line) to 9.0 (thick line) in steps of 0.5 dex. Figure adopted from Tremblay & Bergeron (2009).

with great precision.

## 2.3 Spectroscopy of our DA White Dwarf Sample and White Dwarf Masses

As WDs in open clusters are at a considerable distance and they are intrinsically faint due to their small radii spectroscopic observations consume significant resources.

To work efficiently, photometry from a 4m-class telescopes is first used to identify candidate objects before obtaining follow up spectroscopy of a limited number of objects on a large telescope which are likely to be the type of object we are interested in. All observations of the WD open cluster samples were taken and reduced prior to the work performed during the scope of this dissertation.

### **2.3.1 Photometric Analysis**

Observations of our DA WD samples in both our newly published data for M67 and our reanalyzed clusters (M34, M35, NGC6633, and NGC7063) have been described in detail by Williams & Bolte (2007); Rubin et al. (2008); Williams et al. (2009, 2018). In brief, photometric measurements were taken from the Canada France Hawaii Telescope archive of the Canadian Astronomy Data Centre, the Kitt Peak 4m, the Lick 3m, and the MMT. Calibration was performed with standard IRAF packages: DAOPHOT (Stetson, 1987), DAOPHOT II, and MSCRED. Further observations using the Nickel 1m telescope at the Lick observatory were calibrated with Landolt standards (Landolt, 1992), which were in turn used to calibrate photometry taken on nights where observing conditions of the archived data were unknown. In addition, our recent M67 analysis in Williams et al. (2018) instead used Sloan Digital Sky Survey Data Release 12 data to calibrate our photometric observations (Alam et al., 2015).

Candidate selections followed from regions of color-magnitude diagrams from the calibrated photometry. In short, evolutionary sequences were over plotted and a parameter space spanned by both WDs of cooling ages less than the age of the cluster and within cooling tracks from  $0.4 M_{\odot} < M_{WD} < 1.2 M_{\odot}$  were selected. Details of this

are discussed in Williams & Bolte (2007); Rubin et al. (2008) and Williams et al. (2009, 2018).

### 2.3.2 Spectroscopic Observations

Spectra for WDs in M34, M35, M67, NGC 6633, and NGC 7063 were all obtained using the Low Resolution Imaging Spectrometer (Oke et al., 1995; McCarthy et al., 1998) on the Keck I telescope. Most observations employed the 400 grooves  $\text{mm}^{-1}$ , 3400 Å blazed grism with a 1" slit at the parallactic angle (the slit was orientated such that the direction of dispersion due to the atmosphere is aligned with the long axis of the slit as to maximize the amount of light from the object that enters the spectrograph). A few observations employed the 600 grooves  $\text{mm}^{-1}$ , 4000 Å blazed grism, while some spectra used a 1.5" slit. The onedspec and twodspect IRAF packages were used to reduce the raw data. These spectra have also been discussed in Williams & Bolte (2007); Rubin et al. (2008); Williams et al. (2009, 2018), where additional details and the full spectrum of each object are available.

Determining the resolution of our data presented unusual challenge. To empirically measure the resolution of an instrument's configuration one can take a spectrum of something that has a line width which is much smaller than the resolution of that instrumental configuration's design. Then, the width of a spectral line falls within one spectral element, and therefore the measured width of the line measures the size of the spectral element (the resolution) rather than the unresolved line. This can be done by closing the shutter of an instrument and turning on an internal lamp of known

composition. Such a lamp is commonly available as they are often used to derive wavelength calibration, where the pixels corresponding to the spectrum are matched to spectral lines of known wavelength, thereby identifying the wavelength of that part of the spectrum in the 2D image. In our data it was found that the lamp lines were non-Gaussian, and so we looked elsewhere for an unresolved source through which we could measure resolution. The atmosphere is a strong emitter at particular wavelengths, and its physical conditions are such that line broadening puts the width of these so called sky lines below the resolution of our instrumental configuration. Sky spectra can be extracted from regions of the sky just next to the point sources of interest (the WDs we observe), and it is from these sky spectra that we directly measured the resolution of each of our spectra. Further complicating this was the fact that some of our object spectra were missing complimentary sky spectra. We therefore derived resolutions appropriate for each of our instrument configurations from the sky spectra that were available. For each instrument and slit width configuration we calculated the average resolution as measured by the 5577 Å sky emission line of [O I] (Osterbrock et al., 1996) from the epochs for which sky spectra were available. As resolution is a function of wavelength and most of our information is taken from wavelengths blueward of the 5577 Å line we also took into consideration the theoretical resolution of the blue side. This was found from the Keck Observatory’s web page on dispersive elements. We adopted a resolution between their theoretical value and our mean observed values of each grating and slit size configuration for all of our observations. The resolutions range from 4.1 to 10.7 angstroms.

We estimate that our resolution is accurate to within half an angstrom. Reiterating our spectral fitting process with a one Angstrom perturbation has demonstrated that our surface gravities typically change by about half their uncertainty, and the effect is much less in effective temperature.

### 2.3.3 Spectral Fitting Technique

We derive physical parameters for DA WDs by comparing our spectra with the models of Bergeron et al. (1992a), as updated by Bergeron et al. (1995b) and summarized nicely by Liebert et al. (2005a), as later updated with the work of Tremblay & Bergeron (2009). Unless convection dredges up material or the WD is actively accreting the atmospheric composition of these objects is generally uniform due to stratification by gravitational settling. These models assume pure hydrogen composition, and extend from 1,500 to 140,000 Kelvin in effective temperature and 6.5 to 9.5 dex in log of the surface gravity. As the Balmer line profiles of DA WDs are very sensitive to surface gravity and effective temperature, we focus on fitting the Balmer line profiles alone by normalizing out the continuum slope. Here, we provide a summary of our spectral fitting procedure including a more precise description of the references used than previously available in the literature. Our user supplied functions for describing the absorption line profiles are nonlinear, and the reader is strongly encouraged to review chapters 2, 3, 10, and 15 of *Numerical Recipes* (Press et al., 1992), paying particular attention to sections 2.1, 10.5, 10.6, 10.7, 15.2, 15.4, 15.5, and 15.6 for a detailed understanding of the procedure and interpretation of our errors.

The results of the comparison of the observed spectrum to the model spectrum is

sensitive to the exact normalization of each spectral line. It is for this reason that we require spectra to have an adequate signal-to-noise ratio in later parts of our analysis. From two user supplied wavelengths on either side of each absorption line a simple linear fit is used to normalize the flux values of both the model and the observed spectrum. How this is done has evolved over time as the models have developed. The points chosen for normalization should be within the noise level of the flux in the continuum, but because of the nature of noise an extremum could be selected which would offset the normalization slope over the given absorption line a small amount. In Bergeron et al. (1992a), for either point corresponding to the user supplied wavelength, the flux value was taken as the average flux over a small number of points in the area. This was done to ensure that a spike in the noise would not yield a poor fit through an ill defined continuum slope across the line. In later works it was found that using the smooth function of either a best fit WD model or a pseudogaussian function to describe the line profile yielded a more appropriate linear fit by which to normalize to. For WDs in the temperature regime where the Balmer lines are strongest we fit the spectrum with pseudogaussian profiles to define the continuum slope from two points out in the continuum. Such a function, described in the appendix of Saffer et al. (1988), is not the most appropriate as they describe just the line cores well, but they are sufficient for this purpose as they are computationally inexpensive where the absorption lines are well defined. Unfortunately pseudogaussian profiles do have quite a few degrees of freedom and the fitting routine has difficulty converging if the absorption lines are weak. While the peak line strength depends on surface gravity, peak equivalent width occurs

at roughly 12,000 Kelvin for  $\log g \approx 8.0$  WDs (Wesemael et al., 1993). For remnants more than a few thousand Kelvin from this peak we instead fit the spectrum with our WD models to obtain the flux at the normalization points.

We minimize a  $\chi^2$  figure of merit using the non-linear Levenberg-Marquardt method, an algorithm based on the path of steepest decent. An initial guess of effective temperature and surface gravity are given. From there the procedure runs iteratively. The user inputs the spectral resolution of an observation, and the routine normalizes each line and convolves the models to match the observation's bin size in wavelength. It calculates a  $\chi^2$  for the observation and the WD model of the temperature and surface gravity of the initial guess as well as adapting a new step size. It interpolates the available WD models for the new values of temperature and surface gravity before comparing the new model against the observation and the routine repeats. The mathematics dictates that the method always proceeds in the direction of a minima, and would continue indefinitely in pursuit of that minima unless the user has supplied satisfactory convergence criteria. We set these such that the routine iterates until the step size is less than 10 Kelvin in effective temperature and 0.01 dex in the logarithm of the surface gravity. This sets a fundamental limit of precision in which the physical parameters are known, but it is generally much smaller than our errors. At this point the routine sets the scaling parameter, which normally is used to scale the step size in a non-linear fashion for each iteration, to zero before evaluating the routine once more with the WD model of the previous step's physical parameters to derive the appropriate best fit's physical parameters. In principle, the exact  $\chi^2$  minimum is not found but the



satisfactory step size ensures nearly the best obtainable fit using this set of models has been found. In practice, we set the convergence criteria to be much smaller than the uncertainties in the physical parameters such that this reality has a negligible effect. The best fitting model is of course, our best guess as to the true nature of the WD and its true physical parameters.

The routine fits lines simultaneously by applying equal weight to all points within a user supplied definition of the spectral lines to be considered. Data outside of this range is not considered at all, so issues where the raw data are questionable far enough from line center are not of concern. It is possible to deweight data to elect to fit certain chunks of data and not others in effect, e.g. in the case of blends a DA spectrum can still be fit by assigning a negligible weight to the narrow range of data in which the blend occurs. Equal weighting is applied to all of the other line data. This is important for fitting, e.g. a DAZ WD with significant calcium H+K lines or M dwarf+DA WD binaries.

Fitting the absorption lines simultaneously is important for testing the models to get the physics right. Historically, studies which have not fit the absorption lines simultaneously have revealed inaccurate physics in the atmospheric models on more than one occasion. In principle, no matter what lines are chosen to fit the spectrum the physical parameters should be the same as the WD has just one surface gravity and effective temperature. Where Bergeron et al. (1992a) had noted just such a discrepancy in the physical parameters when different ranges of Balmer lines were used to fit the spectrum and introduced the ad hoc microfield parameter, Tremblay & Bergeron (2009)

accounted for nonideal effects in the line profile calculation. Other studies have also illustrated the ability of simultaneously fitting many absorption lines to improve the model’s physics. In the so called Balmer line problem, systematic differences in the physical parameters arose from fitting the Lyman series as opposed to the Balmer series. Traces of elements heavier than Hydrogen were found to be the cause (Gianninas et al., 2010, 2011).

Related works have also shown that the use of non-local thermodynamic equilibrium (NLTE) models is important beyond 40,000 Kelvin in the case where traces of such elements are present, but Napiwotzki (1997) and Liebert et al. (2005a, Figure 3) suggest local thermodynamic equilibrium (LTE) models are sufficiently accurate for pure Hydrogen models for WDs with temperatures as high as 80,000K. LTE describes the scenario where within a given volume gas particles and blackbody radiation are in equilibrium. While there is a net flux of energy across any volume in the atmosphere, LTE is a common approximation in models of stellar atmospheres. In our 40,000K+ objects we do not see any significant absorption lines which would suggest NLTE models are appropriate, and we note that downward settling at these surface gravities is extremely efficient. With a lack of evidence to the contrary we make the assumption of pure Hydrogen atmospheres throughout the rest of this analysis, and find all our WDs are much less than 80,000 Kelvin which assures us that the use of the Bergeron and Tremblay LTE models is appropriate for our work.

To gather an understanding of the uncertainties in our free parameters, the surface gravity and effective temperature, one may consult sections 15.5 and 15.6 in *Numerical*

*Recipes* (Press et al., 1992). Equation 15.6.5 describes our error,  $\delta a_i$ , for the spectrum's  $i$ th free parameter:

$$\delta a_i = \pm \sqrt{\Delta \chi_\nu^2} \sqrt{C_{ji}}$$

This is derived from a Taylor expansion about the minimum  $\chi^2$  value, where  $\Delta \chi_\nu^2$  describes the interval in  $\chi_\nu^2$  from the minimum to the location of the interval limit chosen and  $C_{ji}$  is the ( $j$ ,  $i$ )th covariance matrix value. With two free parameters,  $\nu = 2$ , we adopt  $\Delta \chi_\nu^2 = 2.30$  such that our errors describe the 68% confidence interval of our  $\chi^2$  figure of merit. The components of the covariance matrix are the inverse of the gradient components where  $\chi_\nu^2$  is minimized (Press et al., 1992, equations 15.5.6, 15.5.8, and 15.5.15). It is *not* simply the case that the RMS of the data to the best fit model are in some direct way represented by our uncertainty in either physical parameter. Our error also does *not* describe ‘one sigma’ as the variance of the  $\chi_\nu^2$  distribution is not the same as that of a Gaussian (whose 68 % confidence interval is the square root of the variance of that distribution), but rather it simply describes the convolution of the 68% confidence interval with covariance value of each parameter.

### 2.3.4 Spectroscopic Fits and Final Masses

We present the physical parameters of our spectroscopic results in Tables 2.1 through 2.5. We have included a simbad identifier for these objects where available as well as their J2000 coordinates for cross-identification.

The spectroscopic fitting routine applies the mixing-length theory (ML2) of convection in one dimension for each object (Bergeron et al., 1992b, 1995b), shown under 1D

$T_{eff}$  and  $1D \log g$ . We use the  $\alpha = 0.8$  prescription, where  $\alpha$  is a free parameter which describes how far material is mixed over the pressure scale height. Simply put, while mixing-length theory does quite well, convection does not work in one dimension as some material must be rising while other material is sinking. We follow the study of Tremblay et al. (2011b), who solved the high  $\log g$  problem for DA WDs, by effectively replicating their more appropriate NLTE 3D model treatment by applying the correction functions for ML2 1D models which are found in the appendix of Tremblay et al. (2013). Unlike the earlier 1D models, the 3D models take into consideration the fact that convectively driven material tends to overshoot past the point in which hydrostatic equilibrium is met (e.g. convective overshoot). It should be emphasized that in these tables the 3D physical parameters are more appropriate, and it is these that we propagate through the rest of this dissertation. There is a small amount of error introduced in the application of the 3D correction function as it was derived as a fitted relationship to real data. This is yet to be quantified, but is qualitatively discussed (Tremblay et al., 2013) and negligible with respect to the size of our uncertainties and physical parameter space for our objects. We note that while the 3D correction functions tend to pull the WD mass and temperature down (Tremblay et al., 2013, see figure 4) this only effects WDs which are cool enough for significant convection ( $T_{eff}$  less than about 14,000K). This is in contrast to the work of Tremblay & Bergeron (2009) (see Figure 2.4), which generally pulled masses and temperatures up over a much broader range of parameter space. The net of these two effects gives the difference in magnitude to be expected between spectroscopic parameters of the reanalyzed objects using the most recent

versions of the models and that which is published in the literature (e.g. Bergeron et al. (1995b)). For the objects which had previously published physical parameters from using earlier versions of Bergeron’s models, we do find that the physical parameters for some of the WDs are significantly different at the level of our errors. That is to say the improvements in the models have made a significant difference. Most of the objects have seen their physical parameters change in such a way that are generally consistent with the level of deviation expected from their previously published values. As we have used models which have incorporated the most recent stark profiles the physical parameters presented here (and in Canton et al. (2019)) should supersede previously published values for the reanalyzed WDs.

By examining how the physical parameters for a WD might vary between a number of different observations of the same object Liebert et al. (2005a) was able to quantify systematic sources of error which are external to the fitting routines. Flux calibration is the dominant source of such external error. Bédard et al. (2017) identified the external error values discussed in the text of Liebert et al. (2005a) were incorrect, and that the correct values are actually shown in Figure 8 of the same paper (Liebert et al., 2005a). They are described explicitly in Bédard et al. (2017). These have been added in quadrature to the uncertainty in each of the physical parameters of our WDs from the fitting routine. While we use their average values, we note that there is significant scatter within their sample and as many of our spectra have poor flux calibration we expect our uncertainties in surface gravity and temperature may be underestimated by up to a factor of two. Further spectra of our objects would be required to quantify this

for each object and so we have been unable to quantify the effect on a case-by-case basis, but we do note that in general the uncertainty this introduces in the initial mass will be dwarfed by the effect of uncertainty in cluster age. As this value cannot be quantified without further observations, the mean value is assumed in the values we report rather than, e.g. twice the mean, as that would overestimate the errors on average.

We have measured the signal-to-noise ratio in the continuum between the  $H\beta$  and  $H\gamma$  lines using SPLOT in the onedspec package of IRAF. For each epoch, we use the appropriate plate scale ( $0.916 \text{ pix}^{-1} \text{ \AA}$ ) and adopt the resolution we used to convolve each model spectrum to convert the measured signal-to-noise ratio per pixel to signal-to-noise ratio per dispersion element. The model grids we currently use to extract initial and final mass do not extend below  $\log g = 7.0$ , so we have not derived final masses for 13H 20H, and 24H in M67. There is no need to extend the grids further to include these objects as the Sweeney (1976) method we apply requires all objects to have evolved in an isolated fashion. At these surface gravities the objects have no doubt experienced mass transfer in a tight binary as the timescale for them to exhaust their nuclear fuel far exceeds the age of any stellar population we might consider.

The WD mass and WD cooling age have been calculated using WD evolutionary models of Fontaine et al. (2001) and Wood (1995). Final mass follows from surface gravity as described in section 1.3, but the evolutionary models also depend on core composition and the thicknesses of the hydrogen and/or helium envelopes lying above the degenerate interior as they set the initial internal heat capacity of the object and its opacities respectively. These models assume Carbon-Oxygen cores for objects below

30,000K and Carbon cores in excess of this effective temperature. They also assume thick pure hydrogen atmospheres ( $q_H \equiv \frac{M_H}{M_\odot} = 10^{-4}$ ). We observe that our reanalyzed masses are generally higher than in Rubin et al. (2008), Williams & Bolte (2007), and Williams et al. (2009), which follows from what we would expect by using the more modern spectroscopic models.

The best fit model over the observed WD Balmer line profiles for M67 and each of our reanalyzed WDs are illustrated in Figures 2.7 through 2.11. To avoid the issue of drift we have systematically fit all spectra over the same range of absorption lines, noting that even where a line is not visually present at the level of the continuum noise valuable information is still present as the line may be quenched. Each subsequent line is shifted vertically, starting from  $H\beta$  at the bottom up through  $H9$  at the top, by an arbitrary offset for clarity. Normalized absorption lines are presented from line center to their wings along the x-axis. Our naming scheme has followed from the LAWDS survey of these previous papers, often adopting numbers which repeat across individual clusters, and having retired the LAWDS naming scheme used in prior literature for the more descriptive labeling prefix of WD in our tables and text. We caution one should be sure to study the correct cluster figures as to not confuse an object of one number for another of the same number in another cluster.

By presenting the physical parameters of our objects prior to making selection cuts to examine the possibility of cluster membership we share some information which is irrelevant for the IFMR analysis to come, but which may be useful for the reader to draw their own conclusions from. We purposefully illustrate our noisy spectra at the

same scale for fair comparison. We feel this is more significant than clearly displaying their detail as these objects will not be studied in further detail in this work. We reserve discussion of individual fits for the sections which follow below.



Table 2.1: M34 White Dwarf Data and Fit Atmospheric Parameters.

Object Solution	Simbad Identifier	RA (J2000)	Dec (J2000)	1D $T_{eff}$ Kelvin	1D $\log g$	3D $T_{eff}$ Kelvin	3D $\log g$	$M_f$ $M_\odot$	S/N
M34:WD18	LAWDS NGC 1039 18	2:40:24.77	42:59:33.1	21000 $\pm$ 300	7.87 $\pm$ 0.05	21000 $\pm$ 300	7.87 $\pm$ 0.05	0.55 $\pm$ 0.02	140
M34:WD17	LB 3565	2:40:27.93	42:30:56.6	26500 $\pm$ 400	8.43 $\pm$ 0.05	26500 $\pm$ 400	8.43 $\pm$ 0.05	0.89 $\pm$ 0.03	115
M34:WD15	LB 3566	2:40:33.73	42:58:16.7	26700 $\pm$ 400	8.41 $\pm$ 0.05	26700 $\pm$ 400	8.41 $\pm$ 0.05	0.88 $\pm$ 0.03	95
M34:WD9H	LB 3567	2:40:37.77	42:52:29.6	16000 $\pm$ 300	7.99 $\pm$ 0.05	16000 $\pm$ 300	7.99 $\pm$ 0.05	0.60 $\pm$ 0.02	92
M34:WD9C	LB 3567	2:40:37.77	42:52:29.6	12200 $\pm$ 200	8.20 $\pm$ 0.05	11900 $\pm$ 200	8.16 $\pm$ 0.05	0.70 $\pm$ 0.03	92
M34:WD40	LAWDS NGC 1039 40	2:40:43.57	42:35:45.6	19600 $\pm$ 600	7.91 $\pm$ 0.09	19600 $\pm$ 600	7.91 $\pm$ 0.09	0.57 $\pm$ 0.04	32
M34:WDS3	C1* NGC 1039 LAWDS S3	2:40:59.08	42:15:13.5	15000 $\pm$ 400	8.49 $\pm$ 0.05	15000 $\pm$ 400	8.49 $\pm$ 0.05	0.91 $\pm$ 0.02	92
M34:WDS2	C1* NGC 1039 LAWDS S2	2:41:05.05	42:15:59.0	32200 $\pm$ 500	8.36 $\pm$ 0.05	32200 $\pm$ 500	8.37 $\pm$ 0.05	0.86 $\pm$ 0.02	113
M34:WD14	LB 3569	2:41:05.76	42:48:15.3	22200 $\pm$ 400	7.74 $\pm$ 0.05	22200 $\pm$ 400	7.74 $\pm$ 0.05	0.49 $\pm$ 0.02	190
M34:WD20	LB 3570	2:41:09.11	42:43:51.1	15100 $\pm$ 300	8.04 $\pm$ 0.06	15100 $\pm$ 300	8.04 $\pm$ 0.06	0.63 $\pm$ 0.03	38
M34:WDN3	C1* NGC 1039 LAWDS N3	2:41:11.11	43:13:25.3	44500 $\pm$ 700	7.73 $\pm$ 0.05	44500 $\pm$ 700	7.73 $\pm$ 0.05	0.55 $\pm$ 0.01	98
M34:WDS1	C1* NGC 1039 LAWDS S1	2:41:17.12	42:25:46.8	23400 $\pm$ 300	7.91 $\pm$ 0.05	23400 $\pm$ 300	7.92 $\pm$ 0.05	0.58 $\pm$ 0.02	113
M34:WDS5H	C1* NGC 1039 LAWDS S5	2:41:33.01	42:03:47.3	17000 $\pm$ 300	7.98 $\pm$ 0.06	17000 $\pm$ 300	7.98 $\pm$ 0.06	0.60 $\pm$ 0.03	63
M34:WDS5C	C1* NGC 1039 LAWDS S5	2:41:33.01	42:03:47.3	12000 $\pm$ 200	8.33 $\pm$ 0.06	11700 $\pm$ 200	8.24 $\pm$ 0.06	0.75 $\pm$ 0.03	63
M34:WD22H	LB 3575	2:41:39.61	42:43:00.3	17900 $\pm$ 400	7.92 $\pm$ 0.06	17900 $\pm$ 400	7.92 $\pm$ 0.06	0.57 $\pm$ 0.03	33
M34:WD22C	LB 3575	2:41:39.61	42:43:00.3	11200 $\pm$ 200	8.37 $\pm$ 0.07	11000 $\pm$ 200	8.19 $\pm$ 0.07	0.71 $\pm$ 0.04	33
M34:WD19	LAWDS NGC 1039 19	2:41:44.93	42:30:05.6	11600 $\pm$ 200	8.09 $\pm$ 0.05	11300 $\pm$ 200	7.99 $\pm$ 0.05	0.59 $\pm$ 0.02	102
M34:WD25	LB 3576	2:41:55.24	42:53:22.0	15500 $\pm$ 400	8.04 $\pm$ 0.06	15500 $\pm$ 400	8.04 $\pm$ 0.06	0.63 $\pm$ 0.03	33
M34:WD102	LAWDS NGC 1039 102	2:42:54.29	43:04:00.3	26200 $\pm$ 500	7.80 $\pm$ 0.07	26200 $\pm$ 500	7.80 $\pm$ 0.07	0.53 $\pm$ 0.03	65
M34:WD34	LAWDS NGC 1039 34	2:42:59.90	42:38:14.3	28900 $\pm$ 500	7.73 $\pm$ 0.06	28900 $\pm$ 500	7.73 $\pm$ 0.06	0.51 $\pm$ 0.02	60

**Notes.** H or C denotes the hot or cold solution for this WD. S/N is given per dispersion element as measured through the  $H\beta$  and  $H\gamma$  continuum from about 4500Å to 4750Å. The external error described in Liebert et al. (2005a) has been incorporated in all of the  $T_{eff}$  &  $\log g$  uncertainties.

Table 2.2: M35 White Dwarf Data and Fit Atmospheric Parameters.

Object Solution	Simbad Identifier	RA (J2000)	Dec (J2000)	1D $T_{eff}$ Kelvin	1D $\log g$	3D $T_{eff}$ Kelvin	3D $\log g$	$M_f$ $M_\odot$	S/N
M35:WD30H	LAWDS NGC 2168 30	6:07:56.63	24:13:27.2	$29000 \pm 600$	$8.53 \pm 0.10$	$29100 \pm 600$	$8.53 \pm 0.10$	$0.96 \pm 0.05$	37
M35:WD30C	LAWDS NGC 2168 30	6:07:56.63	24:13:27.2	$9900 \pm 200$	$9.68 \pm 0.10$	$9900 \pm 200$	$9.41 \pm 0.10$	$1.41 \pm 0.06$	37
M35:WD29	LAWDS NGC 2168 29	6:08:02.20	24:25:24.2	$33200 \pm 500$	$8.44 \pm 0.06$	$33200 \pm 500$	$8.44 \pm 0.06$	$0.91 \pm 0.03$	46
M35:WD22	LAWDS NGC 2168 22	6:08:24.65	24:33:47.6	$54000 \pm 1000$	$8.13 \pm 0.08$	$54000 \pm 1000$	$8.13 \pm 0.08$	$0.76 \pm 0.04$	134
M35:WD1	CI* NGC 2168 RA 1	6:08:38.79	24:15:06.9	$33100 \pm 600$	$8.64 \pm 0.08$	$33100 \pm 600$	$8.65 \pm 0.08$	$1.03 \pm 0.04$	62
M35:WD2	LAWDS NGC 2168 2	6:08:42.30	24:10:17.7	$33300 \pm 600$	$8.93 \pm 0.09$	$33300 \pm 600$	$8.93 \pm 0.09$	$1.17 \pm 0.04$	62
M35:WD27	LAWDS NGC 2168 27	6:09:06.26	24:19:25.3	$30700 \pm 500$	$8.79 \pm 0.07$	$30700 \pm 500$	$8.79 \pm 0.07$	$1.10 \pm 0.03$	86
M35:WD5	CI* NGC 2168 RA 3	6:09:11.54	24:27:20.9	$53000 \pm 1000$	$8.20 \pm 0.07$	$53000 \pm 1000$	$8.20 \pm 0.07$	$0.80 \pm 0.03$	142
M35:WD15	LAWDS NGC 2168 15	6:09:11.63	24:02:38.5	$30000 \pm 500$	$8.64 \pm 0.06$	$30000 \pm 500$	$8.64 \pm 0.06$	$1.02 \pm 0.03$	77
M35:WD14	LAWDS NGC 2168 14	6:09:15.10	24:33:15.4	$29200 \pm 700$	$8.6 \pm 0.1$	$29200 \pm 700$	$8.6 \pm 0.1$	$0.99 \pm 0.06$	40
M35:WD6	CI* NGC 2168 RA 4	6:09:23.48	24:27:22.0	$57000 \pm 1000$	$8.09 \pm 0.07$	$57000 \pm 1000$	$8.09 \pm 0.07$	$0.75 \pm 0.03$	152
M35:WD12	LAWDS NGC 2168 12	6:09:31.19	24:19:06.2	$33400 \pm 600$	$8.79 \pm 0.08$	$33400 \pm 600$	$8.79 \pm 0.08$	$1.11 \pm 0.03$	66
M35:WD11	LAWDS NGC 2168 11	6:09:42.79	24:11:05.4	$20200 \pm 400$	$8.52 \pm 0.06$	$20200 \pm 400$	$8.52 \pm 0.06$	$0.94 \pm 0.04$	57

**Notes.** H or C denotes the hot or cold solution for this WD. S/N is given per dispersion element as measured through

the  $H\beta$  and  $H\gamma$  continuum from about 4500Å to 4750Å. The external error described in Liebert et al. (2005a) has

been incorporated in all of the  $T_{eff}$  &  $\log g$  uncertainties

Table 2.3: M67 White Dwarf Data and Fit Atmospheric Parameters.

Object	Solution	Simbad Identifier	RA (J2000)	Dec (J2000)	1D $T_{eff}$ Kelvin	1D $\log g$	3D $T_{eff}$ Kelvin	3D $\log g$	$M_f$ $M_\odot$	S/N
M67:WD2	...	...	8:50:39.43	11:53:26.82	$14900 \pm 300$	$8.12 \pm 0.06$	$14900 \pm 300$	$8.13 \pm 0.06$	$0.68 \pm 0.03$	66
M67:WD3	...	...	8:50:47.60	11:43:30.04	$10800 \pm 200$	$8.37 \pm 0.07$	$10600 \pm 200$	$8.15 \pm 0.07$	$0.69 \pm 0.04$	39
M67:WD5C	...	...	8:50:52.52	11:52:06.82	$11800 \pm 200$	$8.09 \pm 0.05$	$11500 \pm 200$	$8.00 \pm 0.05$	$0.60 \pm 0.03$	71
M67:WD5H	...	...	8:50:52.52	11:52:06.82	$15600 \pm 300$	$7.82 \pm 0.06$	$15600 \pm 300$	$7.82 \pm 0.06$	$0.51 \pm 0.02$	71
M67:WD6	...	...	8:50:58.61	11:45:38.79	$8900 \pm 100$	$8.26 \pm 0.10$	$8800 \pm 100$	$8.0 \pm 0.10$	$0.59 \pm 0.06$	42
M67:WD8H	...	...	8:51:01.78	11:52:34.48	$20100 \pm 500$	$8.16 \pm 0.07$	$20100 \pm 500$	$8.16 \pm 0.07$	$0.71 \pm 0.04$	45
M67:WD8C	...	...	8:51:01.78	11:52:34.48	$10800 \pm 200$	$8.60 \pm 0.07$	$10600 \pm 200$	$8.38 \pm 0.07$	$0.83 \pm 0.04$	45
M67:WD9	...	...	8:51:05.31	11:43:56.66	$13700 \pm 500$	$7.92 \pm 0.06$	$13700 \pm 500$	$7.92 \pm 0.06$	$0.56 \pm 0.03$	31
M67:WD10	...	...	8:51:08.89	11:45:44.87	$11700 \pm 200$	$8.44 \pm 0.06$	$11400 \pm 200$	$8.31 \pm 0.06$	$0.79 \pm 0.03$	42
M67:WD11	...	...	8:51:09.14	11:45:20.21	$9100 \pm 100$	$8.15 \pm 0.08$	$9100 \pm 100$	$7.88 \pm 0.08$	$0.52 \pm 0.04$	50
M67:WD12	...	...	8:51:09.58	11:43:52.63	$7300 \pm 100$	$8.35 \pm 0.10$	$7300 \pm 100$	$8.26 \pm 0.10$	$0.75 \pm 0.06$	63
M67:WD13H	...	...	8:51:11.04	11:48:14.33	$24000 \pm 2000$	$6.8 \pm 0.3$	$24000 \pm 3000$	$6.8 \pm 0.3$	... $\pm$ ...	18
M67:WD13C	...	...	8:51:11.04	11:48:14.33	$8700 \pm 300$	$7.9 \pm 0.4$	$8600 \pm 300$	$7.6 \pm 0.4$	$0.4 \pm 0.2$	18
M67:WD14	...	...	8:51:12.11	11:52:31.32	$13400 \pm 300$	$8.03 \pm 0.06$	$13400 \pm 300$	$8.03 \pm 0.06$	$0.62 \pm 0.03$	66
M67:WD15	...	...	8:51:19.90	11:48:40.63	$54000 \pm 1000$	$7.63 \pm 0.07$	$54000 \pm 1000$	$7.63 \pm 0.07$	$0.54 \pm 0.02$	55
M67:WD16	...	...	8:51:21.25	11:54:44.56	$10200 \pm 200$	$8.28 \pm 0.08$	$10000 \pm 200$	$8.04 \pm 0.08$	$0.62 \pm 0.04$	34
M67:WD17H	...	...	8:51:21.33	11:50:43.25	$16400 \pm 300$	$7.70 \pm 0.06$	$16400 \pm 300$	$7.70 \pm 0.06$	$0.46 \pm 0.02$	50
M67:WD17C	...	...	8:51:21.33	11:50:43.25	$11700 \pm 200$	$8.14 \pm 0.06$	$11400 \pm 200$	$8.04 \pm 0.06$	$0.62 \pm 0.03$	50
M67:WD19C	...	...	8:51:24.92	11:53:56.61	$13400 \pm 300$	$8.14 \pm 0.06$	$13400 \pm 300$	$8.14 \pm 0.06$	$0.69 \pm 0.03$	34
M67:WD19H	...	...	8:51:24.92	11:53:56.61	$14900 \pm 300$	$8.08 \pm 0.05$	$14900 \pm 300$	$8.08 \pm 0.05$	$0.65 \pm 0.03$	34
M67:WD20C	...	...	8:51:29.95	11:57:32.96	$8500 \pm 100$	$7.9 \pm 0.1$	$8400 \pm 100$	$7.7 \pm 0.1$	$0.42 \pm 0.06$	39
M67:WD20H	...	...	8:51:29.95	11:57:32.96	$27900 \pm 900$	$6.8 \pm 0.1$	$27900 \pm 900$	$6.8 \pm 0.1$	... $\pm$ ...	39
M67:WD22H	...	...	8:51:37.75	11:58:43.22	$15800 \pm 400$	$7.37 \pm 0.08$	$15800 \pm 400$	$7.37 \pm 0.08$	$0.33 \pm 0.02$	34
M67:WD22C	...	...	8:51:37.75	11:58:43.22	$10800 \pm 200$	$7.76 \pm 0.09$	$10500 \pm 200$	$7.58 \pm 0.09$	$0.39 \pm 0.03$	34
M67:WD24H	...	...	8:51:39.75	11:48:05.07	$36000 \pm 3000$	$6.5 \pm 0.5$	$36000 \pm 3000$	$6.5 \pm 0.5$	... $\pm$ ...	16
M67:WD24C	...	...	8:51:39.75	11:48:05.07	$7400 \pm 300$	$7.3 \pm 0.6$	$7500 \pm 300$	$7.2 \pm 0.6$	$0.2 \pm 0.4$	16
M67:WD25	...	...	8:51:40.56	11:46:00.61	$20400 \pm 300$	$7.98 \pm 0.05$	$20400 \pm 300$	$7.98 \pm 0.05$	$0.61 \pm 0.02$	68
M67:WD26	...	...	8:51:40.96	11:40:30.54	$9700 \pm 100$	$8.20 \pm 0.07$	$9600 \pm 100$	$7.93 \pm 0.07$	$0.56 \pm 0.04$	68
M67:WD28H	...	...	8:51:45.02	11:46:56.45	$27000 \pm 2000$	$7.1 \pm 0.2$	$27000 \pm 2000$	$7.1 \pm 0.2$	$0.32 \pm 0.05$	16
M67:WD28C	...	...	8:51:45.02	11:46:56.45	$9000 \pm 200$	$8.2 \pm 0.3$	$9000 \pm 200$	$7.9 \pm 0.3$	$0.5 \pm 0.1$	16
M67:WD29H	...	...	8:51:45.20	11:41:04.55	$18600 \pm 400$	$7.92 \pm 0.06$	$18600 \pm 400$	$7.92 \pm 0.06$	$0.57 \pm 0.03$	81
M67:WD29C	...	...	8:51:45.20	11:41:04.55	$11100 \pm 200$	$8.45 \pm 0.06$	$10800 \pm 200$	$8.25 \pm 0.06$	$0.75 \pm 0.04$	81
M67:WD32	...	...	8:52:12.00	11:37:50.43	$9900 \pm 100$	$8.19 \pm 0.05$	$9800 \pm 100$	$7.93 \pm 0.05$	$0.56 \pm 0.02$	220

**Notes.** H or C denotes the hot or cold solution for this WD. S/N is given per dispersion element as measured through the  $H\beta$  and  $H\gamma$  continuum from about 4500Å to 4750Å. The external error described in Liebert et al. (2005a) has been incorporated in all of the  $T_{eff}$  &  $\log g$  uncertainties.

Table 2.4: NGC 6633 White Dwarf Data and Fit Atmospheric Parameters.

Object Solution	Simbad Identifier	RA	Dec	1D $T_{eff}$	1D $\log g$	3D $T_{eff}$	3D $\log g$	$M_f$	S/N
		(J2000)	(J2000)	Kelvin		Kelvin		$M_{\odot}$	
NGC6633:WD15	LAWDS NGC 6633 15	18:26:08.1	06:24:51.0	$28200 \pm 400$	$7.77 \pm 0.05$	$28200 \pm 400$	$7.77 \pm 0.05$	$0.52 \pm 0.02$	229
NGC6633:WD25	LAWDS NGC 6633 25	18:26:13.6	06:31:05.5	$29300 \pm 500$	$7.03 \pm 0.07$	$29300 \pm 500$	$7.03 \pm 0.07$	$0.32 \pm 0.01$	97
NGC6633:WD4	LAWDS NGC 6633 4	18:27:10.4	06:26:15.7	$21800 \pm 300$	$8.29 \pm 0.05$	$21800 \pm 300$	$8.29 \pm 0.05$	$0.80 \pm 0.03$	177
NGC6633:WD27	LAWDS NGC 6633 27	18:27:12.3	06:21:02.1	$17000 \pm 400$	$8.43 \pm 0.07$	$17000 \pm 400$	$8.44 \pm 0.07$	$0.88 \pm 0.04$	58
NGC6633:WD13H	LAWDS NGC 6633 13	18:27:14.9	06:20:04.1	$53000 \pm 4000$	$7.3 \pm 0.3$	$53000 \pm 4000$	$7.3 \pm 0.3$	$0.44 \pm 0.09$	46
NGC6633:WD13C	LAWDS NGC 6633 13	18:27:14.9	06:20:04.1	$7300 \pm 300$	$9.4 \pm 0.3$	$7300 \pm 300$	$9.3 \pm 0.3$	$1.3 \pm 0.2$	46
NGC6633:WD8C	LAWDS NGC 6633 8	18:27:23.4	06:19:49.8	$11500 \pm 200$	$8.91 \pm 0.07$	$11300 \pm 200$	$8.75 \pm 0.07$	$1.06 \pm 0.03$	34
NGC6633:WD8H	LAWDS NGC 6633 8	18:27:23.4	06:19:49.8	$20200 \pm 400$	$8.31 \pm 0.06$	$20200 \pm 400$	$8.31 \pm 0.06$	$0.81 \pm 0.04$	34
NGC6633:WD7	LAWDS NGC 6633 7	18:27:49.9	06:20:51.8	$19300 \pm 300$	$8.42 \pm 0.05$	$19300 \pm 300$	$8.42 \pm 0.05$	$0.87 \pm 0.03$	174
NGC6633:WD12H	LAWDS NGC 6633 12	18:28:49.9	06:26:12.0	$18400 \pm 300$	$8.13 \pm 0.05$	$18400 \pm 300$	$8.13 \pm 0.05$	$0.69 \pm 0.03$	67
NGC6633:WD12C	LAWDS NGC 6633 12	18:28:49.9	06:26:12.0	$11600 \pm 200$	$8.51 \pm 0.06$	$11300 \pm 200$	$8.37 \pm 0.06$	$0.83 \pm 0.03$	67

**Notes.** H or C denotes the hot or cold solution for this WD. S/N is given per dispersion element as measured through the  $H\beta$  and  $H\gamma$  continuum from about 4500Å to 4750Å. The external error described in Liebert et al. (2005a) has been incorporated in all of the  $T_{eff}$  &  $\log g$  uncertainties.

Table 2.5: NGC 7063 White Dwarf Data and Fit Atmospheric Parameters.

Object Solution	Simbad Identifier	RA (J2000)	Dec (J2000)	1D $T_{eff}$ Kelvin	1D $\log g$	3D $T_{eff}$ Kelvin	3D $\log g$	$M_f$ $M_\odot$	S/N
NGC7063:WD3C	LAWDS NGC 7063 3	21:24:07.3	36:24:45.6	$11200 \pm 200$	$8.54 \pm 0.06$	$10900 \pm 200$	$8.35 \pm 0.06$	$0.82 \pm 0.04$	55
NGC7063:WD3H	LAWDS NGC 7063 3	21:24:07.3	36:24:45.6	$19200 \pm 400$	$8.05 \pm 0.06$	$19200 \pm 400$	$8.05 \pm 0.06$	$0.65 \pm 0.03$	55
NGC7063:WD1C	LAWDS NGC 7063 1	21:24:10.3	36:26:02.2	$11200 \pm 200$	$7.91 \pm 0.05$	$10900 \pm 200$	$7.77 \pm 0.05$	$0.48 \pm 0.02$	107
NGC7063:WD1H	LAWDS NGC 7063 1	21:24:10.3	36:26:02.2	$16500 \pm 300$	$7.57 \pm 0.05$	$16500 \pm 300$	$7.57 \pm 0.05$	$0.40 \pm 0.01$	107
NGC7063:WD18	LAWDS NGC 7063 18	21:24:20.7	36:35:32.0	$8100 \pm 100$	$8.20 \pm 0.09$	$8100 \pm 100$	$8.01 \pm 0.09$	$0.59 \pm 0.05$	57
NGC7063:WD2	LAWDS NGC 7063 2	21:24:21.5	36:26:00.7	$16100 \pm 200$	$7.94 \pm 0.05$	$16100 \pm 200$	$7.94 \pm 0.05$	$0.58 \pm 0.02$	181
NGC7063:WD4H	LAWDS NGC 7063 4	21:24:32.9	36:27:51.5	$16100 \pm 700$	$8.0 \pm 0.1$	$16100 \pm 700$	$8.0 \pm 0.1$	$0.63 \pm 0.07$	20
NGC7063:WD4C	LAWDS NGC 7063 4	21:24:32.9	36:27:51.5	$13200 \pm 700$	$8.2 \pm 0.1$	$13100 \pm 700$	$8.2 \pm 0.1$	$0.74 \pm 0.08$	20
NGC7063:WD6	LAWDS NGC 7063 6	21:24:49.4	36:33:16.4	$11600 \pm 400$	$8.7 \pm 0.2$	$11300 \pm 400$	$8.5 \pm 0.2$	$0.92 \pm 0.09$	25

**Notes.** H or C denotes the hot or cold solution for this WD. S/N is given per dispersion element as measured through the  $H\beta$  and  $H\gamma$  continuum from about 4500Å to 4750Å. The external error described in Liebert et al. (2005a) has been incorporated in all of the  $T_{eff}$  &  $\log g$  uncertainties.

### 2.3.5 Splitting the Spectroscopic Degeneracy with Photometry

For the surface gravity of any particular WD there exists a temperature where the line strength reaches its peak as both the electron populations and the degree of ionization are at odds with each other. For a WD at an effective temperature away from the maximum line strength there exists degeneracy, where there are two local minima in the figure of merit's parameter space. At any fixed surface gravity there is a peak in the absorption line's strength at the effective temperature for which the population in the upper atomic level is maximal. At higher effective temperatures ionization depletes these levels, whereas at lower effective temperatures the upper levels are less populated due to a lower amount of excitation. These best fit solutions are often called the 'hot' and 'cold' solutions. We append H or C to the names of solutions where degeneracy in the WD's spectroscopic solution has made its most appropriate model, and in turn its physical parameters, nebulous.

Of course, any particular WD only has one effective temperature and surface gravity, so the degeneracy must somehow be broken to reveal which model derives from the true physical parameters. Generally, we are able to break this degeneracy by visually inspecting the two solutions over the observed spectrum and determining, by eye, which fit is the better of the two. However, at effective temperatures near the peak line strength it is often difficult to tell by eye which of the two minima is in fact the best solution. Rather than relying on a goodness of fit parameter, we cross reference the WD's photometry as an independent measure to break this degeneracy. We do this by correcting the hot or cold solution's model colors for reddening and cross referencing

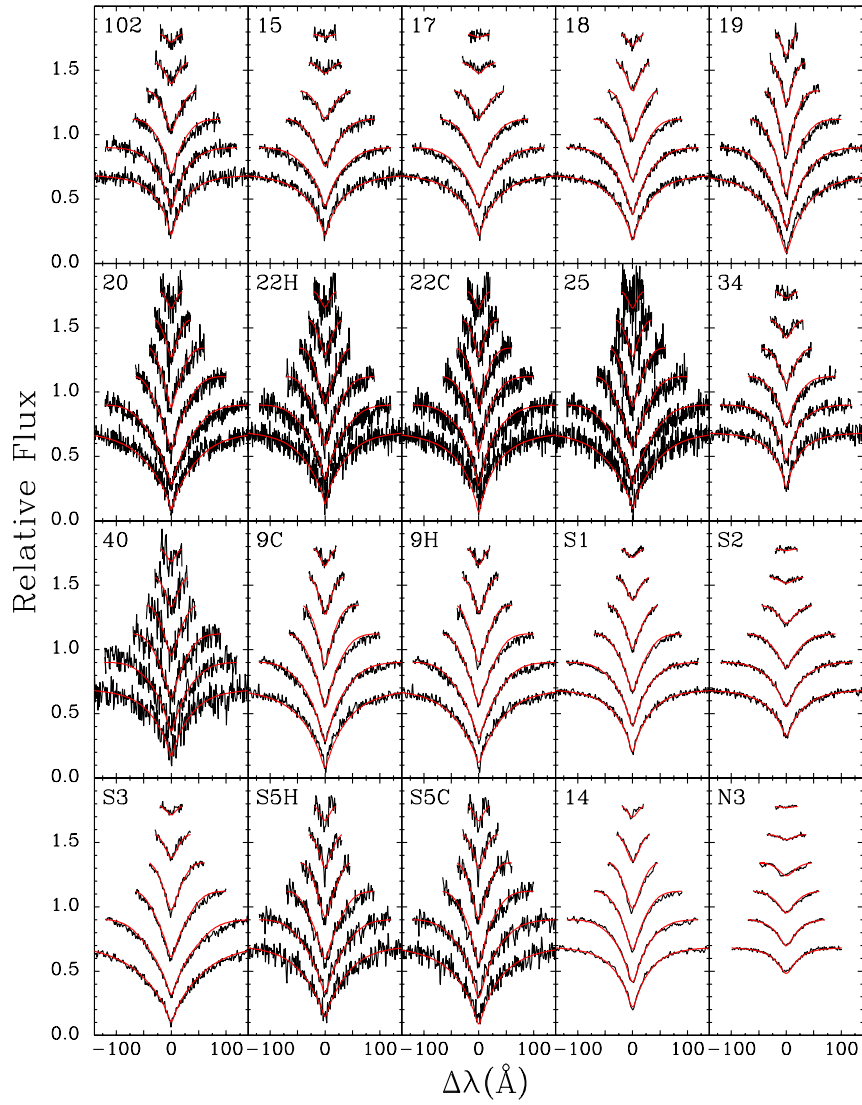


Figure 2.7: Normalized best-fit WD models (red) over plotted on top of normalized Balmer-line profiles (black histograms) for the open cluster M34, showing the offset from line center in angstroms plotted against flux. Displayed from bottom ( $H\beta$ ) to top ( $H9$ ), with an arbitrary offset in flux for clarity.

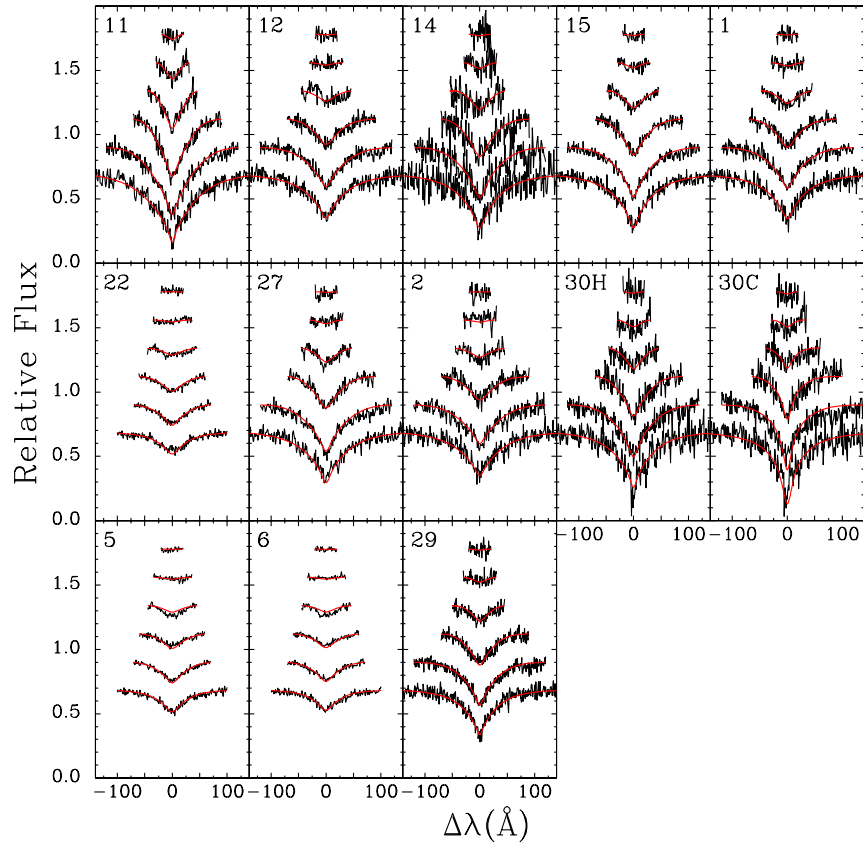


Figure 2.8: The normalized Balmer-line profiles and best fit solutions for M35.



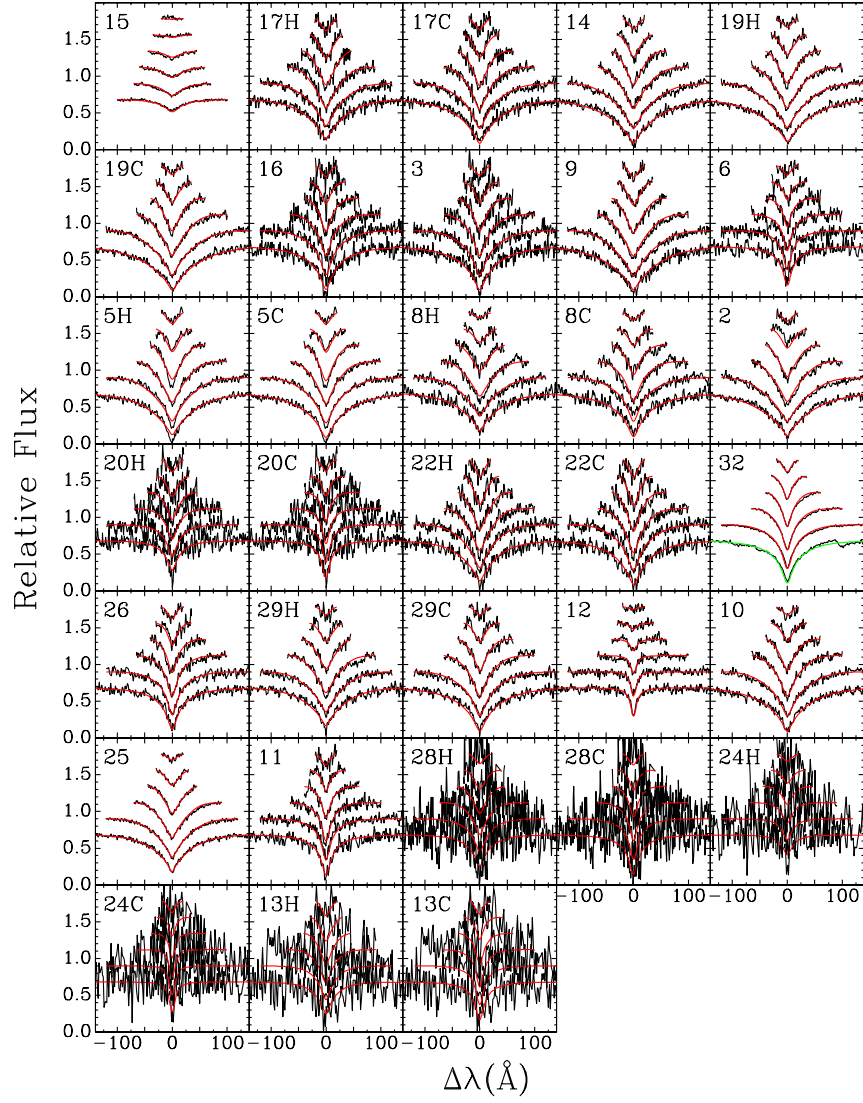


Figure 2.9: The normalized Balmer-line profiles and best fit solutions for M67.

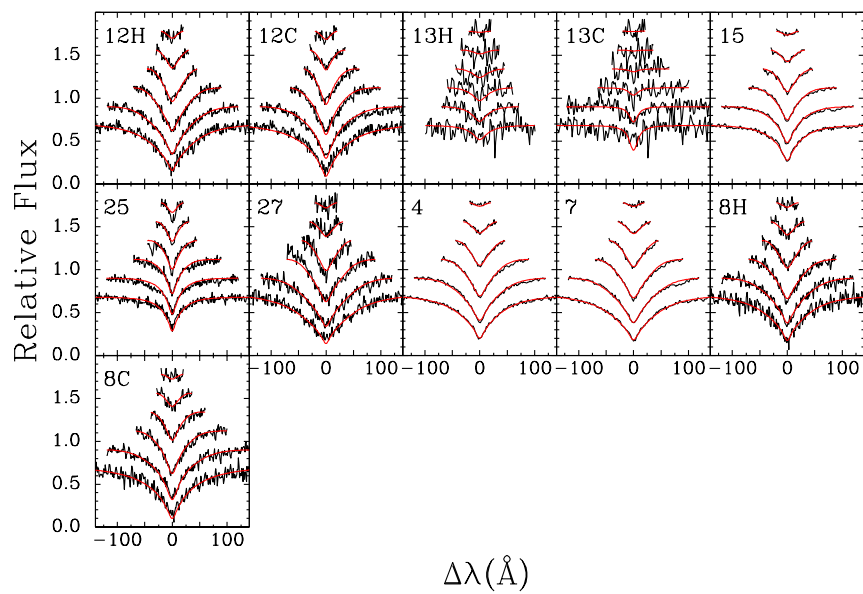


Figure 2.10: The normalized Balmer-line profiles and best fit solutions for NGC 6633.

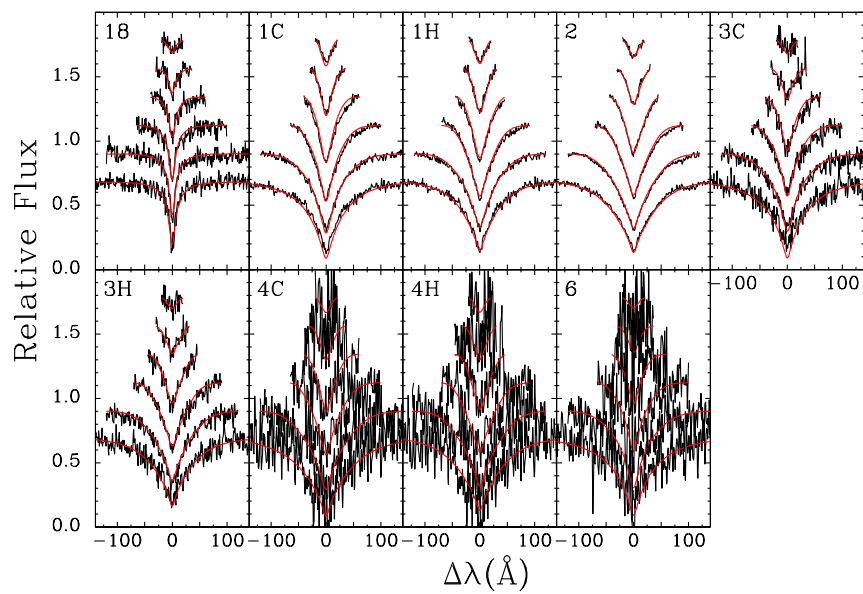


Figure 2.11: The normalized Balmer-line profiles and best fit solutions for NGC 7063.

them against the observed photometry, where our model colors derive from the use of the color and model calculations of Fontaine et al. (2001); Holberg & Bergeron (2006); Kowalski & Saumon (2006) and Tremblay et al. (2011a). Through this, we are able to rule out WDS5H and WD9C in M34, WD30C in M35, WD5H, WD8C, WD17H, WD20H, and WD29H in M67, and WD1H in NGC 7063, but display them in the event that alternate methods of determining physical parameters for these WDs should one day become available. In the case of WD22 in M34, WD19 and WD22 in M67, WD8, WD12, and WD13 in NGC 6633, and WD3 and WD4 in NGC 7063 this procedure is unsuccessful as our photometric uncertainties do not yield a clear choice of one solution over the other. With the correct model uncertain, we acknowledge it would be improper to arbitrarily choose one solution's set of physical parameters over the other and elect to exclude these WDs from the rest of the analysis. We also remove WD13, WD24, and WD28 in M67 for the same reason, but note that the reason for much uncertainty with these particular WDs is the spectra are of poor signal-to-noise.

### **2.3.6 On the Presence of Calcium**

The calcium II H and K spectral lines are some of the most common spectral features known in the visible part of the electromagnetic spectrum. In our reanalyzed spectra we identify little evidence of Calcium. While there are some spectra where a Ca II K absorption line may be evident in the blue wing of H $\epsilon$ , e.g. in M35:WD12 and NGC6633:WD25, in the overwhelming majority of cases there are noise features of comparable amplitude elsewhere in the same spectrum. The possibility of any calcium absorption being interstellar in origin for our M34 sample was proposed by Rubin

et al. (2008), and indeed we find the measured line centers are often blue of the rest wavelength (as opposed to gravitationally redshifted as would be the case if the calcium was in the stellar atmosphere) and the line widths often much too narrow for such high surface gravity objects. We conclude that any Ca II features are of an origin other than the atmosphere of the dense WD observed, and to the limit of our observations the use of hydrogen dominated atmospheric models is well justified.

We explored the effect of a small amount of Ca II in our model fits by refitting our spectra from H $\beta$  to H9 while drastically reducing the weight of the data in the H $\epsilon$  line, where there exists not only the Ca II K line in the blue wing of the H $\epsilon$  line but a blend with Ca II H. A blend acts to alter the line shape and so unless the effect of the other species is taken into account inaccurate physical parameters can result. We found the solutions of all of our reanalyzed WDs converge to within half of our errors, with the notable exception of M35:WD12. This spectrum displays a very asymmetrical H $\epsilon$  profile with a very steep blue wing. The presence of a Ca II K line, apparent at the leftmost edge of the H $\epsilon$  line in Figure 2.8, suggests the shape of the blue wing is simply due to the fact that this line is a blend of H $\epsilon$  with a significant Ca II H line. Evidence to support this comes from our exploration of refitting our spectra. Our solution in Figure 2.8 underestimates the flux in the blue wing when H $\epsilon$  carries significant weight in the fit, however when reducing the weight of this line we recover a solution that matches the flux level more appropriately. Our physical parameters for either M35:WD12 solution are however consistent within errors so we include the H $\epsilon$  line in our adopted solution for the sake of consistency across all our WDs. We do note

that calcium lines from the atmosphere of this star would be exceedingly weak at this WD's effective temperature, which suggest the calcium lines are of interstellar origin in this spectrum. As for NGC6633:WD25, we measure the Ca II K line to be slightly blueshifted with an equivalent width of just 0.56 Å- just a factor of a few more than if the equivalent width of the noise features is measured at the continuum level outside of the line wings.

### 2.3.7 Spectroscopic Peculiarities and Notable Objects

The quality of our fits is generally excellent, but there are some notable exceptions.

*M34:WDN3* — This WD exhibits an asymmetrical H $\epsilon$  line profile, possibly due to blended contamination with Calcium. However, we note that the presence of calcium in this spectrum is negligible as the noise level is comparable to the strength of what could be a Ca II K absorption line.

*M35:WD12* — This spectrum displays an asymmetrical H $\epsilon$  profile which is likely due to the presence of a trace amount of calcium as discussed in the previous section.

*M35:WD22* — In contrast to Williams et al. (2009), we are able to obtain a fit for M35:WD22 which, while still exhibiting a poor fit to the H $\beta$  line core, is a much better fit allowing us to further study this WD for the first time.

*M67:WD5* — We note the quality of our fits for M67:WD5 are less than exemplary.

*M67:WD32* — We identify M67:WD32 as a DA+M dwarf system by the presence of the TiO absorption band near 4950 Å in the red wing of H $\beta$ , and illustrate in Figure 2.9 that we have excluded the blended H $\beta$  line from the fit by illustrating it in green rather than red.

*NGC6633:WD8* — While we find photometry for NGC6633:WD8 to be too uncertain to choose between the hot or the cold solution, we note that this WD was excluded from membership by Williams & Bolte (2007) and included as a member by Williams (2002).

*NGC6633:WD9* — In addition to the normalized line profiles we display, we also studied NGC6633:WD9. This object was identified as an A star by Williams & Bolte (2007). Indeed, we find both the hot and cold solutions for this object have surface gravities lower than  $\log g = 7.00$ . It is likely that the cold solution is appropriate putting it at an effective temperature near 7,600K with  $\log g = 6.57$ , so it may be possible that it is a sdA star instead. It is thought that these objects and low mass WDs are often confused. In the event the object is a low mass WD, it would likely have derived from a binary channel, else it would have an isolated evolutionary timescale far greater than the cluster lifetime. In any case, we eliminated it from our analysis on the grounds that we require the assumption of coeval and isolated evolution of each cluster’s sample.

*NGC6633:WD25* — for NGC6633:WD25 we derive a mediocre fit and measure the Ca II K line to be slightly blueshifted with an equivalent width of 0.56 Å. If real and not an artifact of noise, the calcium line is interstellar and has no effect on the object’s physical parameters. Notably, this object was labeled as an A star by Williams & Bolte (2007). We also derived a low final mass for this object, suggesting that if the star is a bona fide WD, it has had history of mass transfer in its evolution. We therefore do not consider this star any further.

*NGC7063:WD1* — In the event that we have been misled by our photometric

preference for NGC7063:WD1, as might be alluded by the spectroscopic fits presented in Figure 2.11, we note that this object would be a low mass WD whose evolution must have been effected by mass transfer in a binary.

*NGC7063:WD6* — NGC7063:WD6 was described in Williams & Bolte (2007) as a possible blend with another object in the spectrograph’s slit. We also note our spectrum for this object is of rather poor signal to noise, but propagate it through membership selections for the first time.

*NGC7063:WD18* — Our models for NGC7063:WD18 do not yet yield photometry for the hot solution as our IFMR simulation grid does not extend below  $\log g = 7.0$ , however we are confident in our choice of the cold solution as the photometry for the object is consistent with the model prediction at the one sigma level. This object was thought to be an A star by photometric data in Williams & Bolte (2007), but the physical parameters of our spectroscopic fit for the cold solution coupled with photometric consistency suggest NGC7063:WD18 is in fact a WD.



## Chapter 3

# Testing for Membership and Isolation

Through the Sweeney (1976) method described in section 1.6, the IFMR depends on the assumptions that each WD in the sample formed at the same time as the rest of its apparent stellar association and that it has evolved without experiencing mass transfer with a companion. Put another way, it will be assumed that each WD is coeval with the rest of its respective open cluster, evolved with the metallicity characteristic of the other stars in the open cluster, and did so without a close binary companion. A number of selection cuts must therefore be applied as to have a clean working sample of WDs which are isolated members of their respective coeval populations. We apply these selection cuts for M67 and the reanalyzed clusters (M34, M35, NGC 6633, and NGC 7063), but adopt membership selections (and initial masses) for the other cluster samples directly from the literature.

We assume that an object is an isolated member unless proven otherwise, and adopt relatively generous selection criteria for each of these cuts. We are therefore confident that we are careful to exclude WDs which would be improper to include in the IFMR parameter space while being sure to include as many appropriate objects as possible. This approach is expected to result in few false positives while maximizing the efficiency of true positives. As the selection cuts progress through this chapter, we consider only solutions that have passed the previous criteria to that point.

### 3.1 Requirement of Isolated, Single-Star Evolution

Below a certain limit, low mass WDs form exclusively from tight binaries where mass accretion between the objects has perturbed their evolutionary timescales. For these objects the Sweeney (1976) method described in section 1.6 is inappropriate. As we aim to apply this method some care must be taken to exclude low mass WDs from our sample in an efficient fashion.

WDs can form over a range of mass from evolution in tight binaries, whereas there is a fairly well defined minimum mass for which an object could have evolved to the WD stage in an isolated fashion. Stars which form of sufficiently low mass have nuclear lifetimes in excess of the age of the stellar populations (e.g. open clusters) in the Milky Way (where again the nuclear lifetime is the sum of the main sequence and post-main sequence lifetimes). This defines the lower limit on the possible mass of WDs in our sample which can be used for deriving the IFMR.

As an example, consider the Sun. It has a nuclear lifetime of some eleven billion years, whereas all of the open clusters under consideration in this work are younger. Therefore, a star such as the Sun in any of the open clusters we study would still be a star unless it had undergone mass transfer in a tight binary (where we have been careful with our language in that a WD is not a star as it no longer processes nuclear fuel). There is however, at some higher mass than that of the Sun, a certain value of initial mass for which the time it takes to evolve to the WD stage is the age of the cluster. That object would be a very hot WD that had evolved in an isolated fashion in the open cluster. Higher mass stars would have also had time enough to reach the

WD stage, but it is the star at that certain initial mass which sets the minimum mass limit we aim to define.

The age of an open cluster defines for what initial mass there has been just enough time to evolve to the WD stage, but in practice this value is also dependent on metallicity. Strong evidence was put forth by Hansen (2005) and Kalirai et al. (2007) to suggest that metal rich objects will shed more material over the course of their lifetimes. It is therefore appropriate to apply a selection cut that conservatively excludes all low mass WDs that certainly formed from a tight binary channel in the oldest and most metal rich cluster, which in our case is NGC 6791. The objects in this cluster have experienced enhanced mass loss with respect to a cluster of equivalent age at lower metallicity. The same criteria applied for NGC 6791 will also be sufficient to reject objects which have evolved in tight binaries in younger, less metal rich clusters.

Following discussion of NGC 6791 in Kilic et al. (2007) we adopt  $0.45 M_{\odot}$  as the critical mass, the minimum mass for which the assumption of isolated evolution is acceptable. Going forward, objects below this mass will not be considered further for membership or the IFMR analysis. Just three objects in NGC 6791 pass this criterion (see Table 4.5). Although Kilic et al. (2007) do note that this cluster likely exhibits considerable stochastic mass loss through its relatively large metallicity dispersion (0.08 dex), these three objects exhibit final masses at  $0.47 M_{\odot}$  or greater. Objects we later include in the IFMR analysis from additional open clusters found in the literature are all from younger stellar populations where objects of such low mass are yet to form. Unsurprisingly, we find this selection cut has no effect on these samples. Of the

reanalyzed clusters and M67, this cut vets both M67:WD20C and NGC6633:WD25 from the rest of the analysis as they fail to pass our requirement at 0.42 and 0.32  $M_{\odot}$  respectively. Notably, Williams et al. (2018) discuss evidence which suggests M67:WD20 has evolved through a binary channel. Williams et al. (2018) also identify that the colors of M67:WD22 suggest a faint cool companion may be present, although there is little evidence of a companion in the available spectrum. This object has already been vetted from further analysis on the fact that it is not obvious if the hot or cold solution is appropriate (see section 2.3.5), but we do note that the WD mass for either solution is under our adopted critical mass.

We are confident we have kept any appropriate WD which has evolved in an isolated fashion, but there exists a chance that some objects are inappropriately included in the IFMR analysis. The mass cut certainly rules out binaries, but it does not ensure WDs above this mass have not experienced any mass transfer in their past. Still, the contamination level is expected to be small in our sample. Recently Maoz & Hallakoun (2017) found that the SPY survey, which looked at about 1,000 WDs for periodic radial velocity variation indicative of an unresolved binary, found the fraction of WDs in short period binaries is just 10%. A similar number was found with a joint study of both the SPY sample and that of SDSS Maoz et al. (2018). The authors illustrated that the SPY survey was sensitive to binaries with separations up to 4 AU. Combined with the fact that most double degenerate systems have mass ratios near one (which is illustrated by the small spread about the most frequent WD mass, see Figure 1.3), 10% is appropriate for the fraction of contamination we might expect from tight binaries as

a few AU is characteristic of the size at which mass transfer becomes a problem (the Roche lobe, Eggleton (1983)). These authors have not given the fraction of binaries as a function of mass, which would reveal the effectiveness of our choice of mass cutoff. The low mass peak in the mass distribution falls off rapidly to either side around  $0.40 M_{\odot}$ , which is well below the criteria that has been applied suggesting that a notable concentration of WDs which experienced mass transfer have been excluded. Further, this peak rapidly drops off towards higher masses there should be relatively few tight binaries at high mass. The mass distribution therefore suggests it is likely that the majority of WDs that have experienced mass transfer are below the adopted critical mass. This is consistent with what is seen in Figure 3.1, of Brown et al. (2011), which illustrates the fraction of WD binaries as a function of mass. The observed binary fraction is about 50% at  $0.45 M_{\odot}$ , but rapidly falls off to higher masses. This figure provides an upper limit on the samples contamination as only a fraction of binaries are of concern, those that tight enough to have exchanged mass. Williams et al. (2018) recently suggested the merger of two stars may form a blue straggler, which would eventually evolve into a seemingly isolated WD with a substantial excess in its final mass for its initial mass. It was suggested that M67:WD3 and M67:WD29C are in fact from this channel as they are outliers in the IFMR parameter space. These two solutions are tested for membership and propagated through this analysis to study their viability, but are excluded from the IFMR fit to be conservative. In the end, if 10% of WDs are in tight binaries then we would expect about 6 contaminating objects. Outliers may either be field objects or have experienced mass transfer with a companion, but when

all is counted up we are suspicious of the isolation of about as many objects we would expect (M34:WD9H, M34:14, M34:WD25, NGC6633:WD25, M67:WD3, M67:WD20, M67:WD29C, and possibly M67:WD10).

### 3.2 Requirement of Cluster Membership

To apply the Sweeney (1976) method we must confirm the objects are cluster members. Having done so, they are presumably coeval and we can assume the total age of the objects is that of the cluster in which they reside. Generally, a value of a parameter is derived from a large sample of stars in the cluster which is then compared to the value for each object. We apply this methodology to check that each object has been a WD for less time than the cluster has been in existence for, is at same distance as the stars that make up the cluster, and that it has about the same proper motion (or tangential velocity) as the other stars in the cluster. This ensures that the object is at the right distance, is going the right (tangential) velocity, and is of a reasonable age. These criteria are independent of one another and provide strong evidence that if an object has passed these cuts it is a member of the cluster and not just a remnant that happens to appear in the same part of the sky as the cluster (a field star). Other selection cuts, such as on radial velocity or confirming an object's photometry is consistent with the prediction of its spectroscopic model, are possible but in some cases less effective.

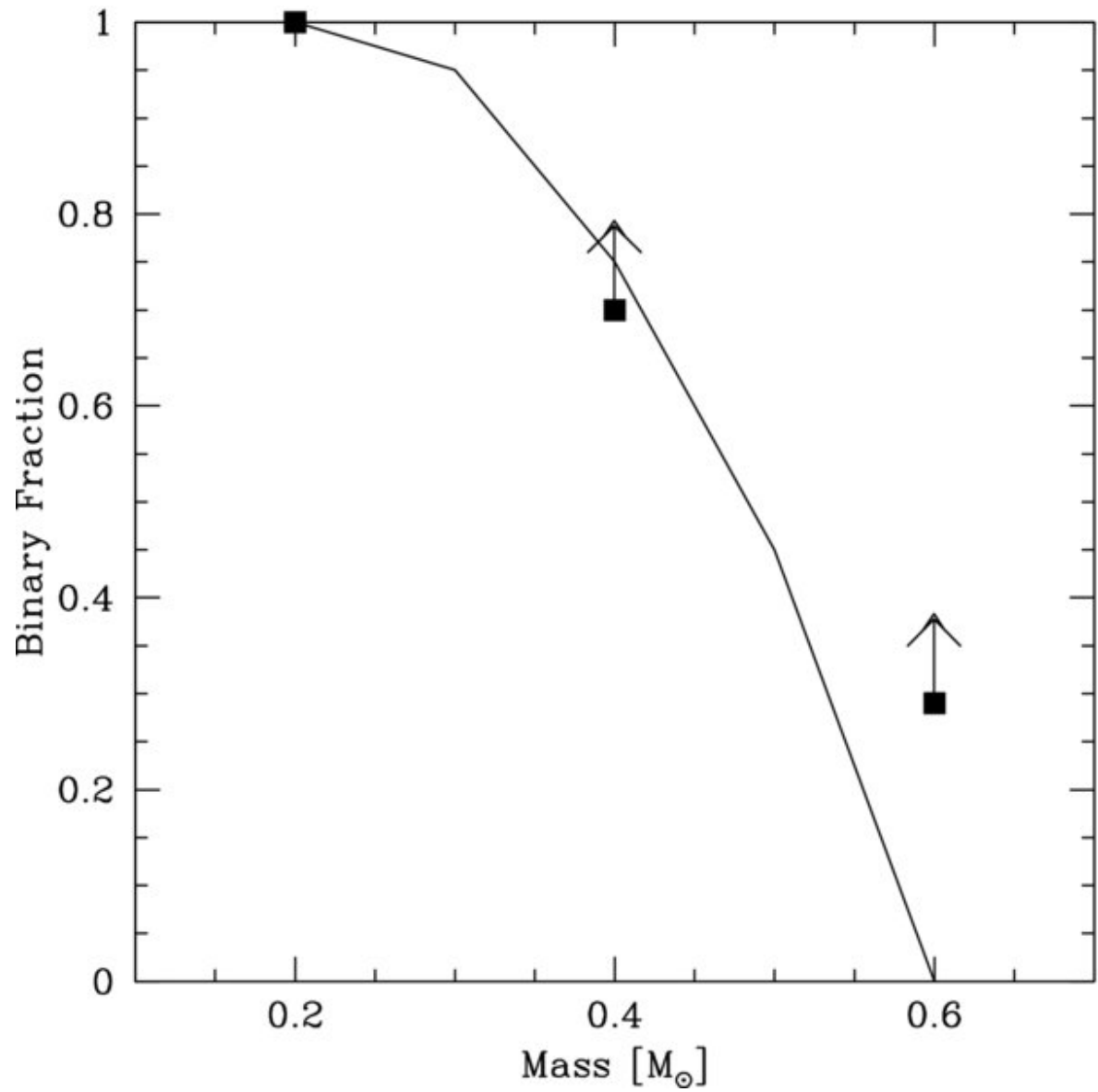


Figure 3.1: Observed WD binary fraction as a function of WD mass, as compared to a theoretical binary evolution model. Figure adopted from Brown et al. (2011).

### 3.2.1 Membership Cuts on Age

WDs which have cooled for longer than the cluster has been around for are not coeval with the cluster. A comparison of the cooling age to the cluster age is therefore effective at excluding WDs which are not cluster members from the rest of our analysis. It is assumed that for the open clusters in our sample all objects have formed at the same time. Although this introduced a minor systematic error this is reasonable as the timescale by which stars of different mass form is very short with respect to the duration of time our objects have been in existence for. It is also important to note that the cluster ages and uncertainties we use are systematically consistent with the PARSEC set of stellar evolution models that are later used in the IFMR analysis work to map nuclear age to initial mass. Our cluster ages are from Kharchenko et al. (2013), Cummings et al. (2016a), Bonatto et al. (2015) and Bressan et al. (2012), noting that the second solution presented for M67 in Bonatto et al. (2015) has been selected as the reddening and age are more consistent with previous literature on the cluster than their best fit.

The selection cut on age for each object in M34 is presented in Figure 3.2. The log of the cluster age and its uncertainty are presented as vertical lines, and the fiducial cooling age of each WD as solid dots with their respective error bars. As described in sections 1.2 and 2.3.4, the uncertainty for each object’s cooling age comes from the evolutionary models of Fontaine et al. (2001) and Wood (1995) with thick atmospheres ( $q_H \equiv \frac{M_H}{M_\odot} = 10^{-4}$ ). These models assume Carbon-Oxygen cores for objects below 30,000K and Carbon cores in excess of this effective temperature. The evolutionary



models also include WD masses and uncertainties obtained through the mass-radius relation, which were presented in Tables 2.1 through 2.5. Objects whose fiducial cooling age are shorter than the cluster age, or to the left of the solid vertical line, have likely been a WD for less time than the cluster has been in existence, suggesting the possibility that it may be coeval with the open cluster’s population.

In M34, only WDS5C, WDS3, and WD19 fail to pass this selection cut. Notably, uncertainties allow for the possibility that in M34 both WD20 and WD25 are older than the cluster. While we will later reason for exclusion of M34:WD25 from our IFMR fit altogether, the Sweeney (1976) method cannot be used to derive a physically realizable initial mass when this is the case (as the nuclear lifetime is negative). The new Monte Carlo simulation used to generate the IFMR data later in this dissertation rejects simulations for which uncertainty result in cooling ages greater than that of the cluster population.

Age-based membership selection for the other reanalyzed clusters are presented in a similar manner in Figures 3.3 through 3.6. Only WD11 in M35 and the remaining solutions in NGC 7063 are rejected. The WD sample for NGC 7063 will unfortunately not provide us any information in the initial-final mass parameter space. The age uncertainties of M35:WD2, M35:WD11, and M35:WD14 cross the cluster fiducial age, with WD11 being the only object for which the fiducial cooling age exceeds the cluster age. M67:WD12 also crosses the cluster fiducial age, although it does not exceed it and is to be further considered. In these cases the membership of these objects are questionable, although of these just M35:WD2 and M35:WD14 will be observed to pass

all our criteria and be used in the IFMR analysis.

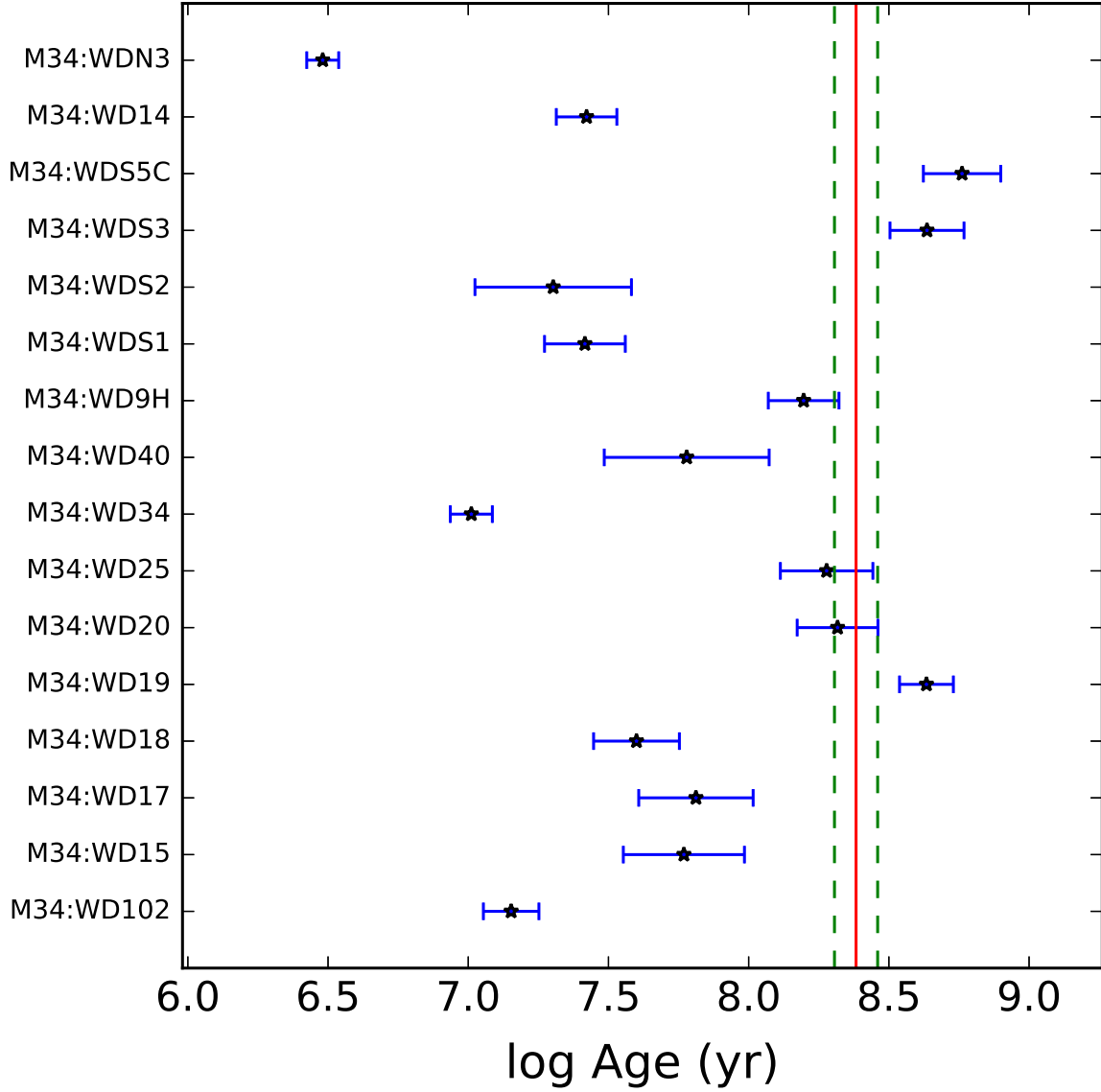


Figure 3.2: Logarithm of the age of M34 (8.383, solid line), with respective cluster age uncertainty (0.077, dashed line) over plotted on the cooling age for each DA WD solution. Error bars indicate  $3\sigma$  uncertainty in WD cooling age.

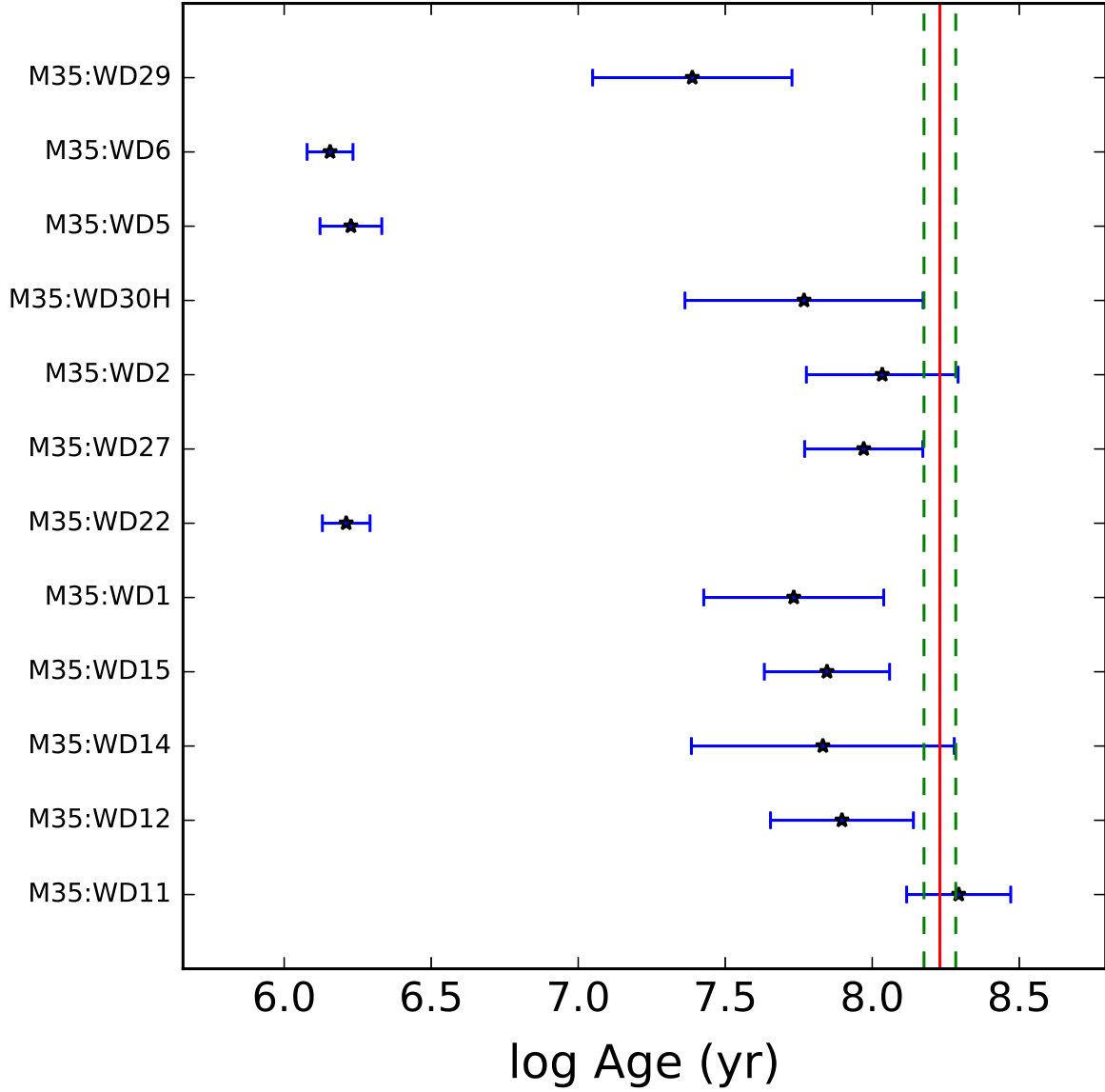


Figure 3.3: Logarithm of the age of M35 (8.230, solid line) with respective cluster age uncertainty (0.054, dashed line) over plotted on the cooling age for each DA WD solution. Error bars indicate  $3\sigma$  uncertainty in WD cooling age.

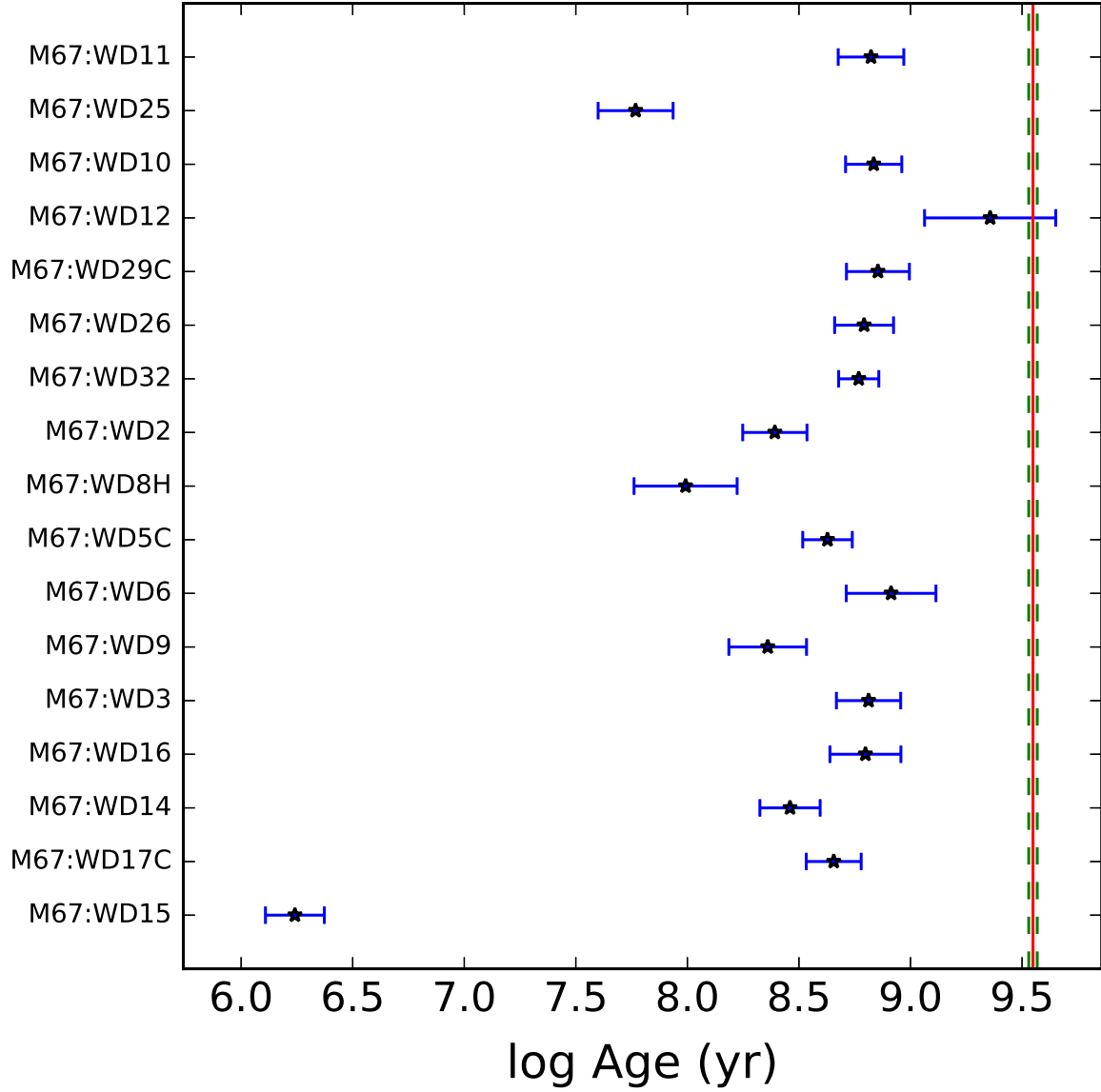


Figure 3.4: Logarithm of the age of M67 (9.549, solid line) with respective cluster age uncertainty (0.019, dashed line) over plotted on the cooling age for each DA WD solution. Error bars indicate  $3\sigma$  uncertainty in WD cooling age.

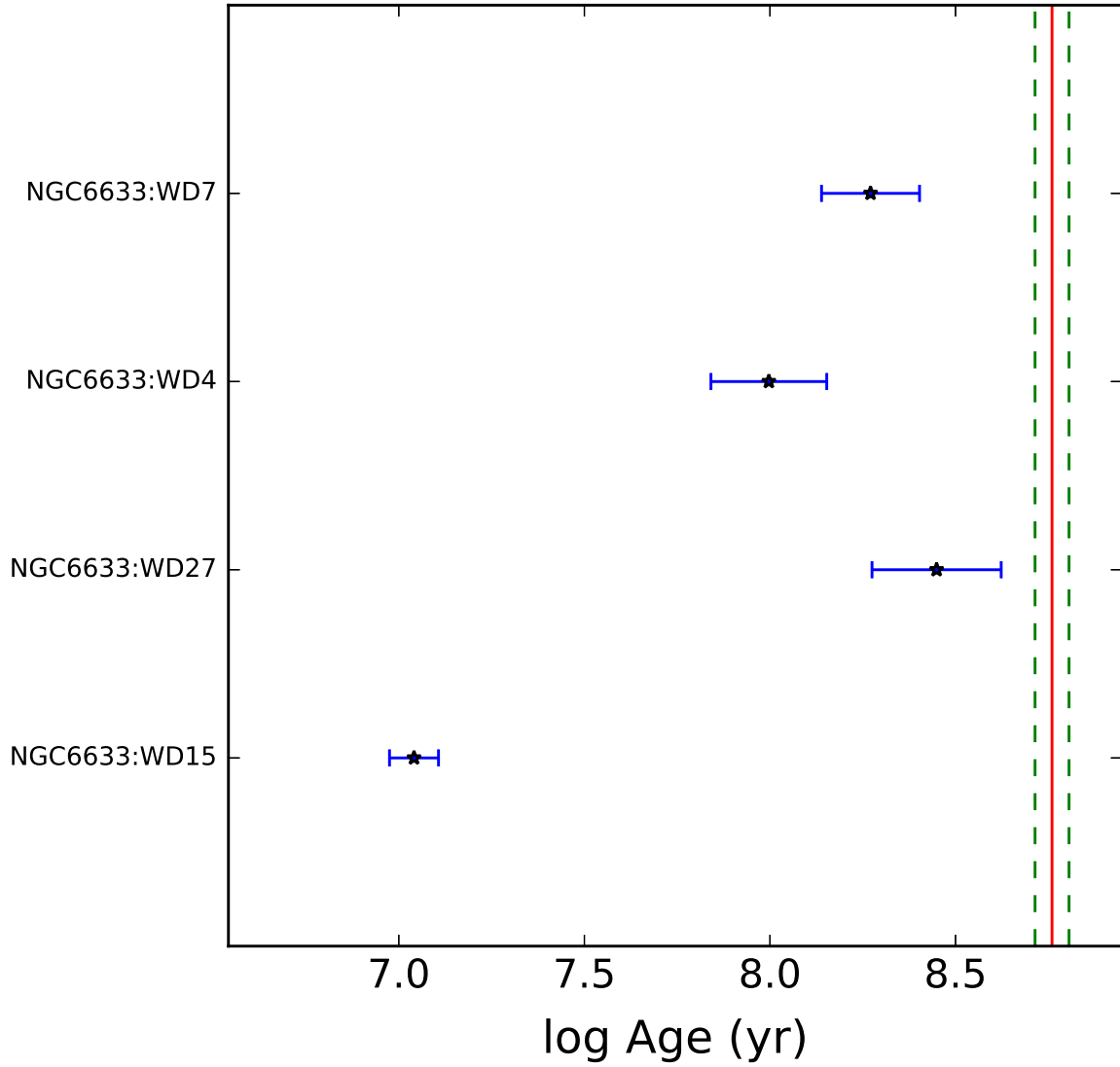


Figure 3.5: Logarithm of the age of NGC 6633 (8.760, solid line) with respective cluster age uncertainty (0.0458, dashed line) over plotted on the cooling age for each DA WD solution. Error bars indicate  $3\sigma$  uncertainty in WD cooling age.

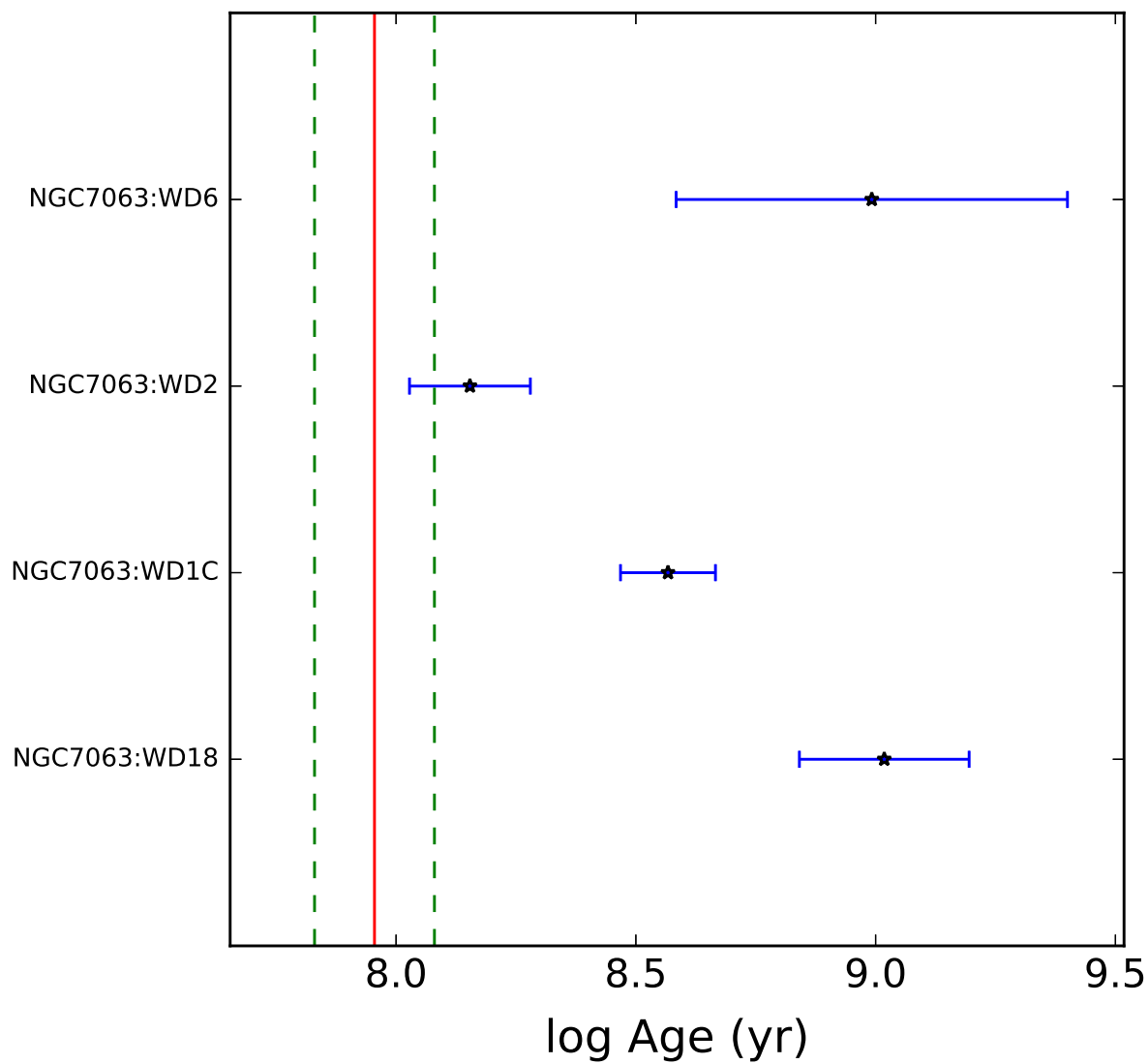


Figure 3.6: Logarithm of the age of NGC 7063 (7.955, solid line) with respective cluster age uncertainty (0.125, dashed line) over plotted on the cooling age for each DA WD solution. Error bars indicate  $3\sigma$  uncertainty in WD cooling age.

### 3.2.2 Membership Cuts on Distance

All cluster members should be at essentially the same distance. As with a light bulb, how bright an object appears depends on both distance and its luminosity. However, this relationship can not simply be inverted as knowing the distance also requires knowing the amount of extinction along the line of sight to the object. Interstellar dust both scatters and absorbs some of the light between the object and our detector. Hence, to avoid having to apply a correction we work with the apparent distance modulus rather than distance directly.

The apparent distance modulus subtracts the apparent magnitude ( $m$ , from the direct imaging originally used to select candidate objects for follow-up spectroscopy) from the absolute magnitude ( $M$ , from the best fit spectroscopic model through the evolutionary models). While this difference is related to distance through extinction, the apparent distance modulus for each WD can be compared with that of its supposed cluster population directly, without having to introduce a choice of extinction correction. In this way the distance modulus is specifically called the apparent distance modulus. We will assume differential reddening, or the extinction along the line of sight to each object, is insignificant.

The evolutionary models calculate the absolute magnitude for the best fitting spectroscopic model for each object, where the absolute magnitude has been convolved to the bandwidth congruent with the observed filter used in direct imaging. In turn the absolute magnitude is used with the apparent magnitudes available in the literature (Rubin et al., 2008; Williams et al., 2009; Williams & Bolte, 2007) to derive the distance



modulus for each object. The uncertainties in the absolute and apparent magnitudes are added in quadrature to derive the uncertainty in distance modulus for each object. Finally, for each WD the uncertainty in distance modulus is added in quadrature with the uncertainty in the distance modulus for each cluster, where the appropriate apparent distance moduli and uncertainties have been adopted or derived for M34 and NGC 6633 from Kharchenko et al. (2013), for M35 from Cummings et al. (2016a), and for M67 from Bonatto et al. (2015). As we cut at three times the uncertainty, we illustrate just that with the error bars presented over each object’s fiducial distance modulus in Figures 3.7, 3.8, 3.9, and 3.10 for M34, M35, M67, and NGC 6633 respectively. Each cluster’s distance modulus is illustrated as a vertical red line, and the uncertainty in this parameter is not explicitly displayed as it has already been folded in to illustrate the magnitude of our selection cut’s tolerance over the object’s fiducial distance modulus.

Objects which pass this selection cut have error bars that cross the cluster’s fiducial distance modulus. This cut excludes WD14, WD18, WD34, WD40, WD102, and WDN3 from membership in M34, while only excluding WD15 in M35. WD8H, WD10, WD11, WD12, WD15, and WD32 in M67 are also excluded, as is WD15 in NGC 6633. We confirm the suspicion of both Fleming et al. (1997) and Weidemann (2000), that M67:WD15 is not a member of M67. All of the aforementioned objects are either foreground or background to the cluster.

Binaries are problematic and are to be excluded if they are tight enough to have experienced mas transfer. In these figures the identification of possible binaries is trivial as they should appear foreground by up to 0.75 mag. The presence of an extra

unresolved companion would mean the object would appear brighter by about a factor of two as two objects would be contributing light rather than one, and the companion cannot be brighter than the WD as it would almost certainly be evident in the spectrum. This value is not exact but a rule of thumb, as the relative contribution of the companion will depend on the temperature of the objects and the shape of their spectral energy distributions. Of the objects that do appear foreground not all will pass our final cut, on proper motion, while others will be excluded for reasons we discuss explicitly.

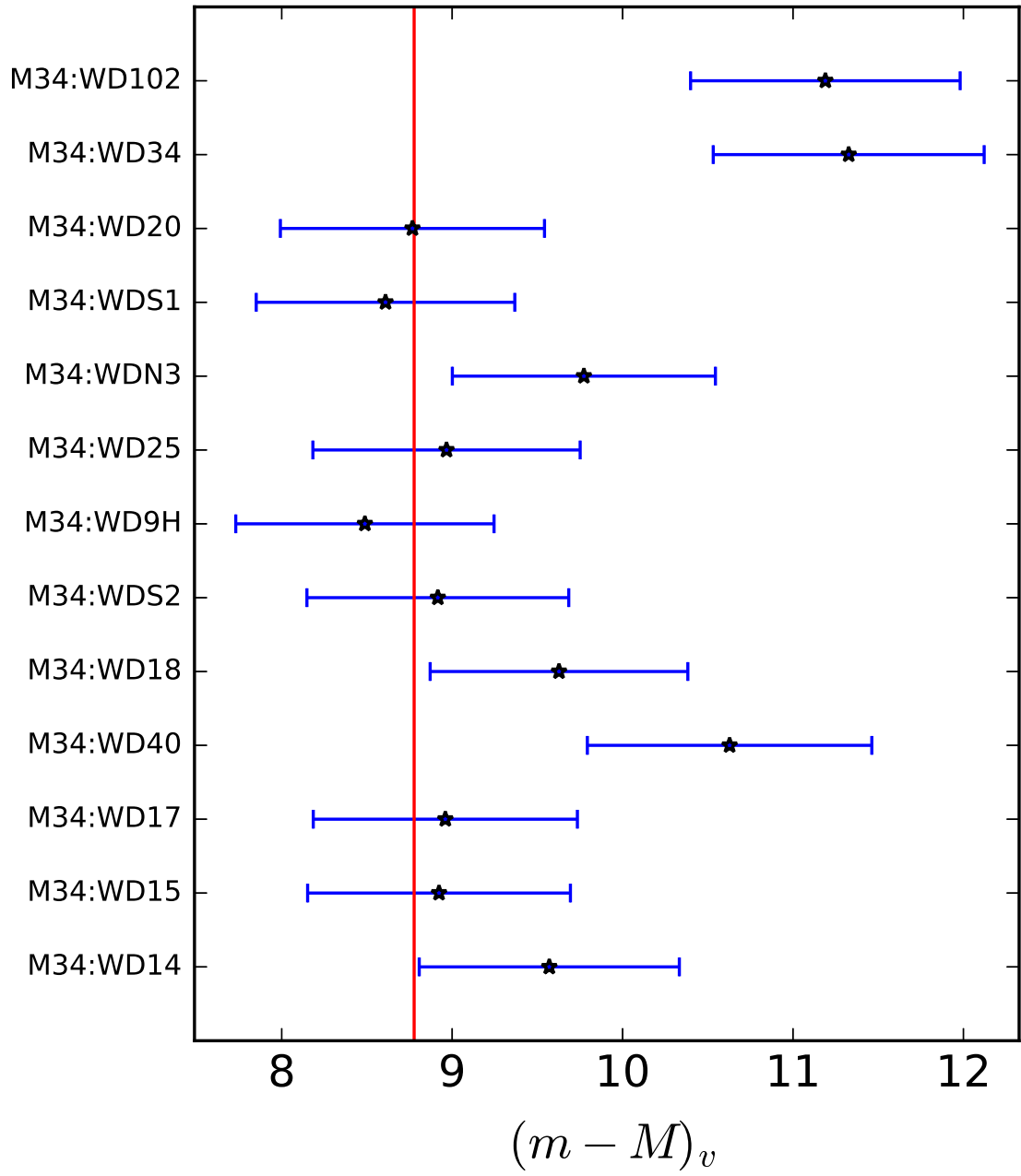


Figure 3.7: Apparent distance modulus of M34 (solid red line) compared the apparent distance modulus for each WD, both observed through the V filter. Error bars are plotted as  $3\sigma$  uncertainties; any solution whose error bar does not intersect the red line is therefore excluded as a cluster member.

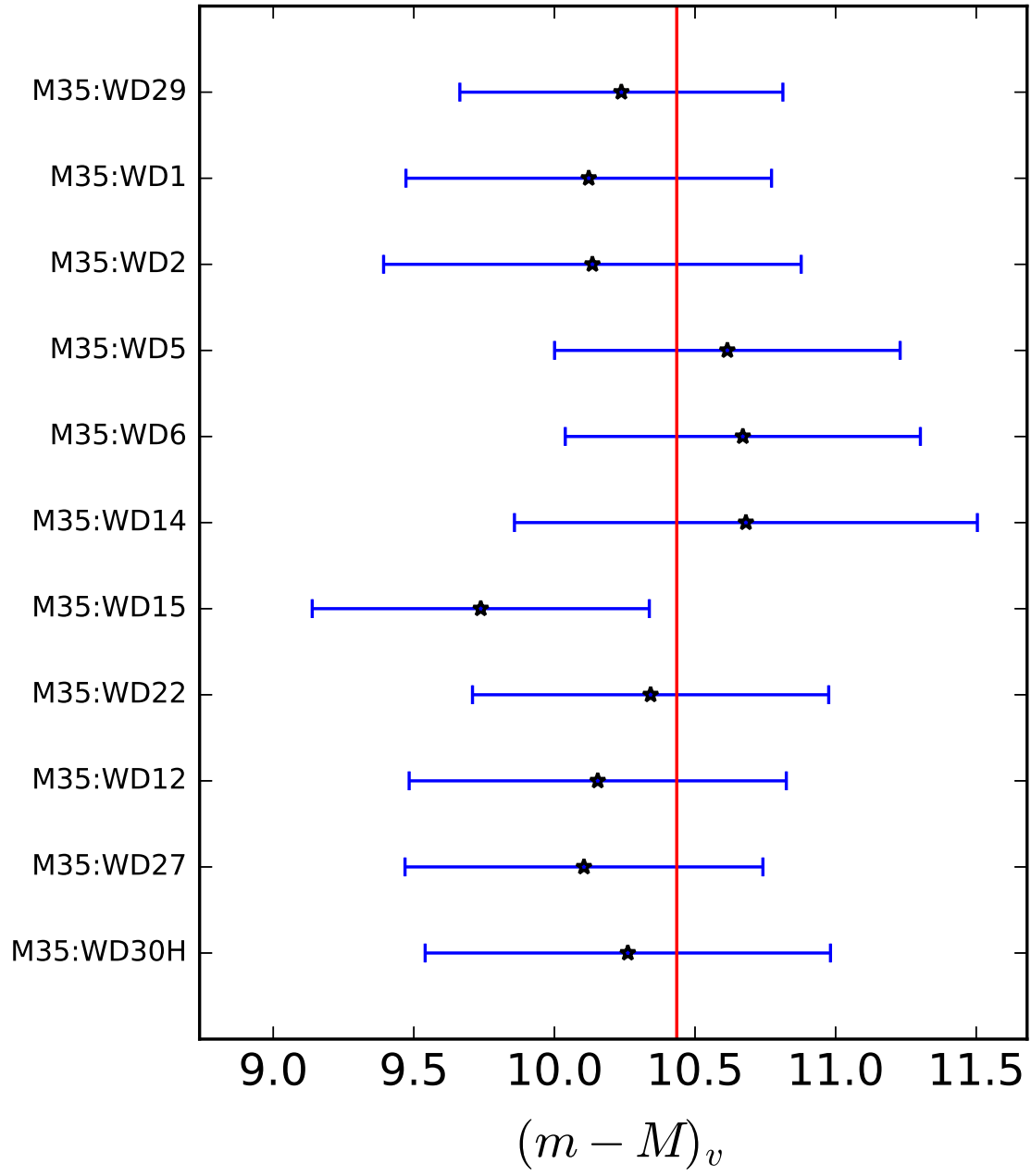


Figure 3.8: Same as Figure 3.7, except for M35. Objects whose  $3\sigma$  error bars fail to cross the cluster's distance modulus (vertical red line) are excluded as cluster members.

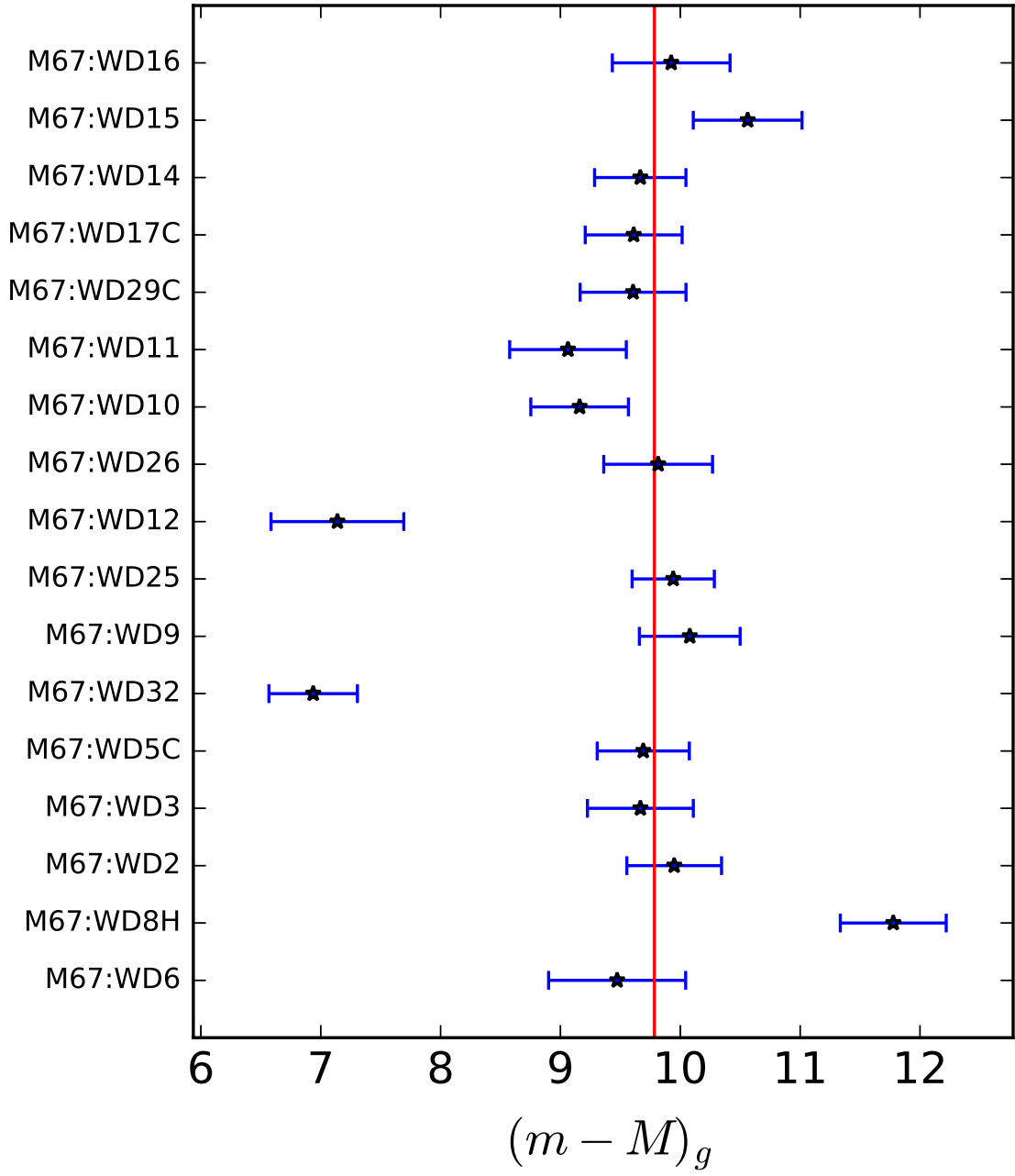


Figure 3.9: Same as Figure 3.7, except for M67 as observed through the  $g$  filter. Objects whose  $3\sigma$  error bars fail to cross the cluster's distance modulus (vertical red line) are excluded as cluster members.

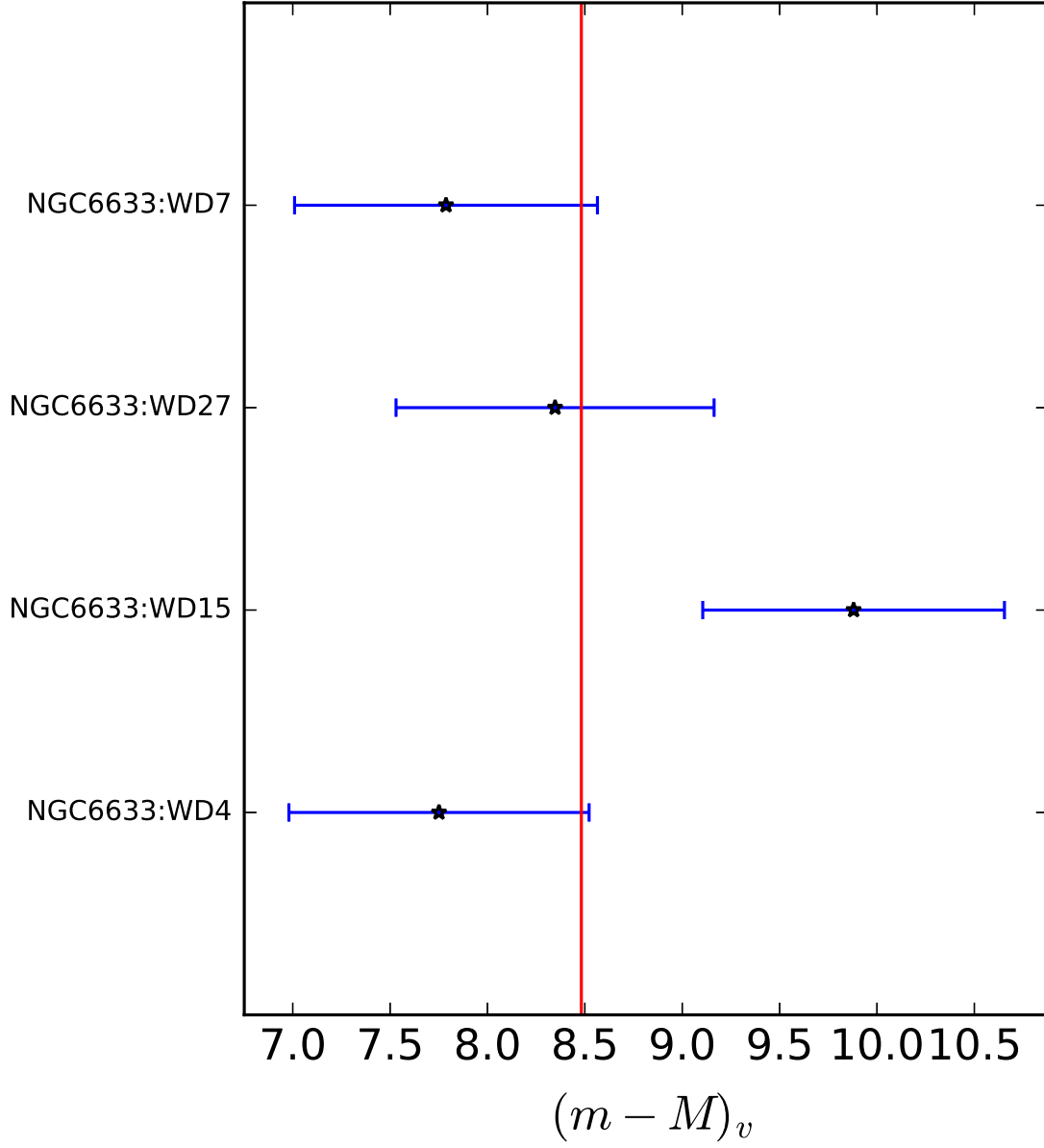


Figure 3.10: Same as Figure 3.7, except for NGC 6633. Objects whose  $3\sigma$  error bars fail to cross the cluster's distance modulus (vertical red line) are excluded as cluster members.

### 3.2.3 Membership Cuts on Proper Motion

Proper motion, measured in units of angle per unit time, describes how an object is seen to move across the sky with respect to a fixed background. Its measure requires obtaining images of an object at more than one epoch and is dependent on both distance and tangential velocity. The selection cut on distance has already ensured that the remaining objects in each cluster are at more or less the same distance, so in effect this selection cut tests if the WDs have tangential velocities characteristic of the stars in the cluster.

Information on proper motion is completely independent from our other selection cuts. It is thus an important criterion, but the available data for our reanalyzed objects is incomplete as the WDs in these open clusters are faint and it can take years for the subtle change in position to appreciate to a measurable scale. The relative errors for an individual object are often too large for this cut to be meaningful, but with enough baseline and a well determined cluster proper motion a selection cut on this parameter can be effective. Fortunately, a well determined value for the cluster proper motion is not hard to come by as it can be measured from a large sample of stars which are substantially brighter than the WDs. However, the motion of field stars in the Milky Way and the cluster may be such that the two distinct populations have little difference in proper motion as observed from Earth. Nevertheless the selection cut can be effective, as a cut on proper motion applied to the M67 sample successfully identified contamination due to field objects at the level of 30% (Williams et al., 2018).

We adopt the average proper motion of 40 stars as the proper motion of M34,

$\mu_{RA} = 0.03 \pm 0.18$  and  $\mu_{Dec} = -7.43 \pm 0.17$  (Loktin & Beshenov, 2003). We obtain proper motion data for our M34 WDs from the SuperCOSMOS Sky Survey (Hambly et al., 2001). To define criteria likely to accept cluster members while rejecting field contamination efficiently we require an object deviate by no more than three times our proper motion uncertainty in both right ascension and declination, where we define our proper motion uncertainty in either direction by adding the respective cluster and object proper motion uncertainties in quadrature. For M34 WD9H, WD15, WD17, WD25, and WDS2 pass our criterion, as does WDS3, WD34, and WD14 although these were cut on the basis of the age and distance cuts. M34:WD14 is notable in that it barely failed the distance cut but passed all the other selection cuts including this one. Indeed, more accurate proper motion data from GAIA DR2 also confirms the object passes the proper motion cut (Giammichele et al., 2018). However, in consideration that M34 is not a particularly old cluster and the WD’s mass ( $0.49 M_{\odot}$ ) it may have evolved in a tight binary. No exception is made for this object, and it is excluded in the IFMR analysis. While WDS3 passes the proper motion cut, the preferred cold solution failed the age cut so it too will be left out. The proper motion cut explicitly excludes just WD20 and WDS1 from membership. The rest of the M34 objects (WD102, WD18, WD19, WD22, WD40, WDS5, and WDN3) lack proper motion data to apply this selection cut. These results are consistent with the selections discussed in Dobbie et al. (2009), with the exception of M34:WD9H which follows from our slightly more relaxed uncertainty requirement. As discussed in section 3.3, having observed that this object could be a member an exception is made and it is excluded from the rest of the IFMR



analysis as it is in a young cluster with a final mass ( $0.60 M_{\odot}$ ) characteristic of a typical field WDs (Figure 1.3). In preliminary analysis it was found to have an unusually high initial mass for its final mass. This supports the suspicion that this object does not fit in as a coeval member of the cluster and is instead a field star.

At present proper motion data for our objects is available for M67 and NGC 6633, while proper motion data for M35 is forthcoming and will be presented in future work. For our M67 objects we adopt the proper motion membership of Williams et al. (2018), who in turn have employed the criteria of Bellini et al. (2010). In summary just WD3, WD6, WD9, WD10, WD14, WD15, WD16, WD17, WD19, WD20, WD22, WD24, WD25, WD26, and WD29 were found to be proper motion members of M67. Of these a number have already been excluded. Two of these are WD3 and WD29, which are suspected to have blue straggler progenitors (section 3.1). WD10 and WD15 failed the apparent distance modulus test. Likewise, WD24 was previously excluded as the spectrum was too noisy to derive meaningful results, while WD19 and WD22 were previously excluded as it was not possible to decide between the hot or cold solution, and WD20 was excluded because of its low mass. WD2 and WD5 in M67 are excluded by this cut. If the suspected blue straggler progenitor channel objects are included, this leaves nine objects which are likely isolated coeval members in M67, found in Table 4.4. Williams et al. (2015) discussed the available proper motion data for WD4 in NGC 6633. While NGC6633:WD4 was found to have a proper motion which deviates from that of NGC 6633 by 4 times the uncertainty in the proper motion of the object, it was pointed out that QSOs from the same catalog show a root mean squared dispersion similar in

scale. While the GAIA DR2 release does not have any proper motion information on our M35 objects, it has data for NGC6633:WD4, NGC6633:WD7, and NGC6633:WD27 (Giammichele et al., 2018). From this, all three passed the same criteria applied for M34. Further, the available parallax for NGC6633:WD4 also suggests that this object is consistent with cluster membership within the object’s uncertainty. The rest of the objects in NGC 6633 have already been excluded: WD25 for being low mass, WD15 for failing the distance cut, and WD8, WD12, and WD13 through the inability to decipher if the hot or cold solution is appropriate.

NGC6633:WD4, and NGC6633:WD7 continue to be particularly interesting. These objects do not show significant radial velocity variation (Williams et al., 2015), but would appear to be foreground to NGC 6633 as isolated WDs. These objects are massive as would be expected of WDs in a cluster of the age of NGC 6633, and in such a way that would be somewhat atypical of a field WD (see Figure 1.3). They also appear in the initial-final mass parameter space with an initial mass in reasonable agreement with the IFMR for their final mass. It is likely that these objects are binaries which are coeval with the cluster and wide enough to have not experienced mass transfer. If verified, these would be the only such occurrence known where the initial and final masses can be derived using both the Sweeney (1976) and the Andrews et al. (2015) methods. Considerable discrepancy exists between these methods at the level of 0.1-0.2  $M_{\odot}$  in final mass, so these objects should be further explored to identify systematic inconsistencies between the two methods.

### 3.3 Comparison With Membership in the Literature

The membership determinations have resulted in some differences with the literature which are summarized here. All WD solutions which have passed all of the selection cuts are included in Tables 4.2 through 4.4, excluding M34:WD9H which has been excluded from the IFMR analysis for reasons discussed in section 3.2.3 and below.

Unless explicitly discussed here, the membership criteria we use has identified objects which are consistent with the membership analyses in previous literature (Williams & Bolte, 2007; Rubin et al., 2008; Williams et al., 2009, 2018). While M34:WD9H passes all the selection cuts as the hot solution, it is found to be of rather high initial mass for its final mass. It also has a final mass that is typical of the field distribution and it only narrowly passed the proper motion criteria. While the hot solution is a better match to the photometry (for which the object passed all of our criteria), we will take a conservative approach and exclude this object from the rest of the IFMR analysis. While Rubin et al. (2008) considered WD20 and WDS1 in M34 to be cluster members, proper motion criteria have now ruled these objects out from membership. Although a choice between the hot and cold solutions for M34:WD22 was not possible, if the hot solution is adopted as in Rubin et al. (2008), in contrast to their work, the remnant would pass all of the criteria here with the caveat that the application of the proper motion cut is not yet possible. This difference is likely due to systematic differences in the application of the apparent distance modulus cut. Unlike in Rubin et al. (2008), M34:WD25 has passed all the selection criteria as we use a slightly older cluster age. The narrow margin by which this object passes the age cut suggests a short lifetime,

which in turn yields a high initial mass. Given this object has a final mass typical of the field WD population, it is unlikely that it would have descended from such a high mass star in the cluster population. Its initial mass is included in Table 4.2 and it is illustrated on the plot of the initial-final mass parameter space, but it is excluded in the IFMR regression. In the future proper motion measurements will help to understand if this object is a member of M34.

In M35, the membership determinations differ from the work of Williams et al. (2009) for just WD11, WD15, and WD22. We used a slightly younger cluster age, and WD11 now fails the age cut while WD15 fails the distance cut. Aside from WD11 and WD15, all of the WDs for which we have analyzed spectra for passed all of the selection criteria. This includes WD22, which historically had model fits which were a disappointing match to the observed spectral features. M35:WD22 is used in the determination of the IFMR in chapter 4.

The membership determinations for M67, NGC 6633, and NGC 7063 generally agree with the previous literature. The membership for M67 agrees with the work of Williams et al. (2018), although for we apply more stringent requirements to ensure isolated evolution (by excluding low mass WDs and WDs that are suspected to have evolved from a blue straggler). For this reason M67:WD3 and M67:WD29 were excluded in this work (see section 3.1). M67:WD19 has been excluded due to the difficulty of choosing between the hot and cold solutions, but no matter which solution is appropriate for this object it passes all of the selection criteria above, including the cut on proper motion. As the cold solution the object would be about 0.2 magnitude foreground. M67:WD19

could therefore be a member as a binary, although at almost  $0.7M_{\odot}$  it is unlikely to have undergone mass transfer as a tight binary. Its mass is typical of field WDs, and would be uncommonly high as an isolated cluster member for such an aged population. Thus, it is likely that either the hot solution is appropriate and it is an isolated member at  $0.65 M_{\odot}$ , or that it is a cluster member as the cold solution in a wide binary with a massive unseen compact component. In the latter case it could be useful for comparing the various methods by which initial mass can be found, although Occam’s razor would suggest the hot solution is more likely. Williams et al. (2018) excluded M67:WD10 on the basis that it was a potential binary. Consistent with that study M67:WD10 failed the selection cut on distance in such a way that it appears to be a foreground object at a level that is consistent with being an unresolved binary. If this were the case this object would be particularly interesting in that it would pass all of the selection cuts, including proper motion, as NGC6633:WD4 and NGC6633:WD7 have. As with those objects additional observations could reveal this object to be the first known wide WD binary in an open cluster from which the initial and final masses could be derived using both the Sweeney (1976) and Andrews et al. (2015) methods. However, unlike the NGC 6633 objects, M67:WD10 is yet to be checked for radial velocity variation. Follow-up spectroscopy is needed to rule out this object being a short period binary. While the results of the selection cuts are the same as in Williams & Bolte (2007) for NGC 6633, depending on which of the hot or cold solution is appropriate WD8 may also be coeval with the cluster. Although this object has been excluded from this analysis because of the difficulty of identifying which of the hot or cold solution is appropriate, in Williams

& Bolte (2007) the cold solution was adopted. If instead the hot solution is appropriate WD8 may be a cluster member as it would pass all of our selection criteria, although proper motion data is still not available. With better photometric precision this object may be useful in future IFMR studies. None of the previously observed WDs in NGC 7063 are of use, as was previously found by Williams & Bolte (2007) and Dobbie et al. (2009).

## Chapter 4

### On the Initial-Final Mass Relation

As we populate the initial-final mass parameter space with a Monte Carlo simulation the resulting figure is a busy plot, unlike much of the previous literature. Historically, error in initial and final masses for each object have been presented as perpendicular error bars about the fiducial value. However, this description fails to illustrate the uncertainty contours that result through the Sweeney (1976) method as the initial and final masses are correlated.

The regression performed in the literature is often not described in detail such that it would be reproducible. While some studies apply a simple unweighted fit the uncertainties for some objects can be quite large while others are simultaneously quite small. This is because objects at higher masses have smaller nuclear lifetimes. More explicitly, for the same size uncertainty in cluster and cooling age, the same range of nuclear lifetime maps to a wider range in initial mass. At short nuclear lifetimes the propagated uncertainties yield a wide range in initial mass, so objects at high initial mass tend to have larger error bars. This is compounded by the fact that, within each cluster, more massive objects have formed more recently so they tend to be hotter. Hot remnants usually have more uncertain physical parameters as the Balmer line sensitivity falls off away from the temperature characteristic of maximum equivalent width (see section 2.3.5). Further, field objects may pass our selection cuts (as was the case for M34:WD25), and if their cooling age is just below the cluster age they will have a short nuclear lifetime so they will have a very high initial mass for their final mass. For these

reasons, an unweighted fit is not appropriate and weighted schemes must be explored.

Few of the previous IFMR studies describe the weighted schemes that were used (Kalirai et al., 2008; Cummings et al., 2015, 2016a). In truth some methods are better than others, but there is no one right way to derive weights. An ad hoc weighing scheme has often been used to get a reasonable fit, such as progressively dropping the weight of points towards high masses (J. Cummings 2018, priv. comm.). We began by exploring methods to assign weights for each data point based on the uncertainty in both initial and final masses. The uncertainty in each direction for each point are asymmetrical, and the variables are correlated. Typically, when uncertainty in both parameters must be accounted for orthogonal distance regression (ODR) is used, whereby the distance of each point to a linear fitted function is measured from a perpendicular direction to the line. However, exploring this with the ODR package of Boggs et al. (1992) yields unsatisfactory results. Although our Monte Carlo simulations show that the errors in the initial-final mass parameter space for each object are asymmetrical, we approximated the uncertainty in the initial and final masses with uniform distributions to derive the weights using this ODR package. This approximation seemed reasonable as points with large asymmetry tend to occur at high mass with large errors, so when the uncertainty is highly asymmetrical the point tends to carry little weight anyhow. The ODR package did not find a fit that was visually a good match to the data. What had happened was the uncertainties in effective temperature and surface gravity had mapped to considerable differences in the size of the uncertainty in initial mass through the stellar and evolutionary models. The relative size of the uncertainty in the data



resulted in relatively few points dominating the weight of the fit. It was clear that a better treatment of the uncertainties was needed - one which would eliminate the need for an ad hoc weighting scheme.

Analytical solutions which might describe how the parameters are correlated are nontrivial, and we will show it is best to explore this problem with an equivalent Monte Carlo approach instead. By sampling within the uncertainties in effective temperature, surface gravity, and cluster age, the uncertainty in initial mass is found. As long as the simulation is run over a healthy range of the input parameters and many iterations the analytical function it aims to replace can be represented accurately (Press et al., 1992). Then, having properly explored the uncertainties an unweighted fit to the result of the Monte Carlo simulations is sufficient to describe the fiducial initial and final masses as well as the uncertainties in these parameters for each object.

## 4.1 Extracting the Initial Masses

Initial mass for each of the WDs in this study have been found using the method of Sweeney (1976) (see section 1.6). We assume that each remnant has evolved in an isolated fashion, and is coeval with the cluster (see chapter 3). With this, the total time that the object has been in existence is simply the duration of time the object had burned nuclear fuel plus the amount of time the object has been a WD. The initial mass for each object in M67 and the reanalyzed clusters with sufficient signal-to-noise is presented in Tables 4.2 through 4.4. Unless otherwise noted all of the objects included in these tables are used in the rest of our IFMR analysis. The systematic errors describe

the effect of the cluster age uncertainty. The systematic error is the difference in initial mass which follows from the fiducial cluster age to the initial mass which results from assuming the maximum or minimum cluster age. The random errors describe the 68% confidence interval from sampling Gaussian distributions about the fiducial values of the physical parameters with the cluster age fixed at its fiducial value.

The cluster ages, cooling timescales, and nuclear lifetimes must all come together to map the temperature and surface gravity to initial mass. For the M67 sample and the reanalyzed cluster samples of M34, M35, and NGC 6633 the same cluster ages are used for our selection cut on age as were used here for deriving the initial mass (section 3.2.1). With these, the evolutionary models are used to map surface gravity and temperature to how long the object has cooled for (how long the object has been a WD). These are the models of Fontaine et al. (2001) and Wood (1995), which assume the remnant’s core composition is pure carbon at or above 30,000 K, but half carbon and half oxygen below this temperature with the assumption that the hydrogen layer comprising their envelope is just  $M_H/M_{WD} = 10^{-4}$  (in the literature this mass fraction is said to be ‘thick’ in reference to the hydrogen layer thickness, whereas ‘thin’ atmospheres suggest a mass fraction  $\sim 10^{-10}$ ). Hydrogen makes up a small fraction of the star, but as it floats up and dominates the only part of the star we can directly observe, the atmosphere. Along with the size of the remnant, which is governed by surface gravity through the mass-radius relation, the hydrogen layer governs the rate of which energy is able to leave the object as it is a source of opacity. These evolutionary models can be found at <http://www.astro.umontreal.ca/~bergeron/CoolingModels/>.

Subtracting the cooling age from the cluster age gives us the nuclear lifetime. Mapping the nuclear lifetime to the object’s initial mass requires some assumption about the metallicity the object evolved with as models predict this effects the total mass loss from the star. Unfortunately, metals have long since settled out of the atmosphere of the remnants as is evident in their spectra, but having established some confidence in membership it can be assumed that each of the WDs still under consideration evolved as a star with metallicity characteristic of stars we observe in its respective cluster today. For M34, M35, M67, and NGC 6633 we adopt  $[\text{Fe}/\text{H}] = 0.02 \pm 0.06$ ,  $-0.143 \pm 0.014$ ,  $0.00 \pm 0.06$ , and  $-0.08 \pm 0.12$  respectively, where  $[\text{Fe}/\text{H}]$  is a logarithmic measure of iron content relative to hydrogen as compared to that of the sun. These values are based on high resolution spectroscopy of stars which are members of the cluster (Heiter et al., 2014; Steinhauer, 2003), through which they are relatively well constrained. Then, the PARSEC 1.2S models of stellar evolution (Bressan et al., 2012), which describe how long a star of a particular mass and metallicity takes to evolve to any particular stage (e.g. red giant, or WD), are used in the following sense: The model which has the cluster’s metallicity and the same nuclear lifetime as the WD describes the initial mass of that object.

We note that the random errors for our hottest objects in M35, around 50,000 K, are particularly small and round to zero at the level of the hundredths place. The other objects in this cluster are all around 30,000 K and have random error of at least an order of magnitude greater. There are two reasons the random error is so much smaller for the hot objects. The first effect is that at longer nuclear age (or hotter temperature having

had less time to cool), the range of nuclear age allowed by the uncertainty in nuclear age maps to a narrower range in initial mass. Secondly, differences in the uncertainty of the physical parameters influence the size of the uncertainty in the nuclear age in such a way that the nuclear age is more precise for hotter objects. This is counterintuitive, as one might expect that the less precise physical parameters of hot objects would yield less precise cooling ages, and in turn less precise nuclear lifetimes. There is, however, a more dominant force at play. Hotter objects cool faster, so the uncertainty interval in temperature for a hot object will result in a more well defined cooling age uncertainty. We find that at 50,000 K the uncertainty in temperature is often a factor of two larger (the sensitivity to the Balmer lines falls off with higher temperature), but because of the difference in cooling rates the evolutionary models still yield cooling age uncertainty that is a factor of two smaller for the hot objects. This is illustrated in Table 4.1, where we demonstrate these sensitivities for hypothetical objects at 50,000 and 30,000 K for fixed surface gravity ( $\log g = 8.00$ ) and fixed cluster age (that of M35, 170 Myr).

Table 4.1: Dependence of Random Error on Temperature.

Temperature	Cooling Age	Nuclear Lifetime	Random Error in Initial Mass
Kelvin	log(Yr)	log(Yr)	$M_{\odot}$
50,000 $\pm$ 1221	6.260 $\pm$ 0.036	8.225 $\pm$ 0.036	+0.00274 -0.00056
30,000 $\pm$ 653	6.966 $\pm$ 0.073	8.206 $\pm$ 0.073	+0.02022 -0.00638

**Notes.** Hypothetical objects in M35. Assumes fixed  $\log g = 8.00$  for each object and fixed cluster age (8.230 in log). The errors in temperature are just typical values one might have for such uncertainty at 30,000 and 50,000 K.

Table 4.2: Initial Masses of WDs in M34.

Object Solution	Mi	Random Error	Systematic Error
	$M_{\odot}$	$M_{\odot}$	$M_{\odot}$
M34:WD15	4.20	$+0.09_{-0.08}$	$+0.41_{-0.34}$
M34:WD17	4.25	$+0.10_{-0.08}$	$+0.43_{-0.36}$
M34:WD25 <sup>a</sup>	7.10	$+2.88_{-1.00}$	$+8.37_{-1.75}$
M34:WDS2	3.91	$+0.03_{-0.03}$	$+0.29_{-0.26}$

<sup>a</sup> Excluded from the IFMR fit. Suspected field star.

**N.B.** Random errors describe a 68% confidence interval from sampling Gaussian distributions for our physical parameters having fixed the cluster age at the fiducial value. Systematic errors describe the uncertainty in initial mass from assuming the maximum or minimum cluster age with respect to the initial mass from assuming the fiducial cluster age.

Table 4.3: Initial Masses of WDs in M35.

Object Solution	Mi	Random Error	Systematic Error
	$M_{\odot}$	$M_{\odot}$	$M_{\odot}$
M35:WD1	4.95	+0.24 -0.20	+0.41 -0.35
M35:WD12	5.48	+0.47 -0.31	+0.62 -0.49
M35:WD14	5.21	+0.54 -0.38	+0.48 -0.41
M35:WD2	6.50	+1.48 -0.79	+1.32 -0.86
M35:WD22 <sup>a</sup>	4.25	+0.00 -0.00	+0.22 -0.20
M35:WD27	5.88	+0.60 -0.38	+0.89 -0.60
M35:WD29	4.50	+0.09 -0.07	+0.28 -0.25
M35:WD30H	5.03	+0.36 -0.28	+0.44 -0.37
M35:WD5 <sup>a</sup>	4.25	+0.00 -0.00	+0.22 -0.20
M35:WD6 <sup>a</sup>	4.25	+0.00 -0.00	+0.22 -0.20

<sup>a</sup> Random error is nonzero but rounds down in the hundredths place.

See section 4.1 for discussion.

Table 4.4: Initial Masses of WDs in M67 and NGC 6633.

Object Solution	Mi	Random Error	Systematic Error <sup>a</sup>
	$M_{\odot}$	$M_{\odot}$	$M_{\odot}$
M67:WD14	1.46	+0.01 -0.00	+0.03 -0.03
M67:WD16	1.52	+0.01 -0.01	+0.03 -0.03
M67:WD17C	1.48	+0.01 -0.01	+0.03 -0.03
M67:WD25 <sup>b</sup>	1.42	+0.00 -0.00	+0.03 -0.02
M67:WD26	1.51	+0.01 -0.01	+0.03 -0.03
M67:WD29C <sup>a</sup>	1.53	+0.01 -0.01	+0.03 -0.03
M67:WD3 <sup>a</sup>	1.52	+0.01 -0.01	+0.03 -0.03
M67:WD6	1.55	+0.03 -0.02	+0.03 -0.03
M67:WD9	1.45	+0.01 -0.00	+0.03 -0.03
NGC6633:WD27	3.48	+0.20 -0.14	+0.29 -0.24
NGC6633:WD4	2.93	+0.03 -0.02	+0.13 -0.12
NGC6633:WD7	3.14	+0.06 -0.05	+0.18 -0.16

<sup>a</sup> Excluded from the IFMR fit. Suspected to have evolved from a blue straggler through mass transfer.

<sup>b</sup> Random error is nonzero but rounds down in the hundredths place.

**N.B.** Random error for objects in M67 is generally small because initial mass is weakly dependent on nuclear age for such long lived objects. The cooling rate is similar for that sample as the objects span a radiatively narrow range in temperature.



## 4.2 The Initial-Final Mass Relation

The aim of this analysis is to illustrate an improved method for handling the uncertainties involved in deriving an IFMR through the spectroscopic method while incorporating more recent spectroscopic models and the addition of the M67 WD sample. The M67 sample provides a significant solar metallicity constraint at the low mass end. At higher masses, the physical parameters for WDs in M34, M35, and NGC 6633 have now been updated with models which incorporate non-ideal effects, external fitting errors, and 3D atmospheric model corrections (Tremblay & Bergeron, 2009; Liebert et al., 2005a; Tremblay et al., 2013). The physical parameters ( $T_{eff}$  &  $\log g$ ) of objects from additional open clusters which were studied with the same models and corrections have also been pulled from the literature to sample the parameter space as best as possible while avoiding the introduction of external systematics. As the same models and corrections were used, there is no need to re-examine the membership and binarity determinations in the literature for these objects. The initial and final masses for these objects are recalculated through the new Monte Carlo simulations to examine the uncertainties in an improved fashion, and, unsurprisingly, are found to be consistent with those which have been previously published.

There are further objects in the literature with both initial and final masses which we do not consider in this work. They are based on a different set of models, and therefore their inclusion would introduce external systematic error. Salaris et al. (2009) showed that the scatter this introduces is considerable if a mix of models have been used for various objects, and should be avoided. The same set of stellar evolution models,

those of Bressan et al. (2012), are used to derive the cluster age and to map the nuclear lifetime to the initial mass for all of the objects we consider. It is of interest to ask how our results might change if a different set of stellar evolution models were used. This was explored in IFMR analysis of Cummings et al. (2016a), where the results from set of models we use were compared with the results found from using those of Yi et al. (2001). It was found that the results differed in cluster age by some 10-20 Myr and in initial mass for the objects by about  $0.1 M_{\odot}$ , suggesting the choice of stellar evolution models has a significant effect on accuracy on par with the internal sources of error considered. With intention of minimizing internal systematic errors, only objects from open clusters whose initial mass has been derived through the Sweeney (1976) method are considered (with the exception of one particularly well studied nearby WD, Sirius B).

The objects that are included in the IFMR analysis are summarized here and in Tables 4.2, 4.3, 4.4, and 4.5. The total sample used to derive the IFMR fit in section 4.2.2 includes 63 WDs in total, with 62 from 12 open clusters and Sirius B (64 objects are plotted, with M34:WD25 not being considered in the IFMR fit). While all objects in the young open cluster NGC 7063 have been excluded, we include objects from the recently published M67 sample and the reanalyzed objects in M34, M35, and NGC 6633. Our additional cluster WDs are from the Hyades, the Pleiades, NGC 2099, NGC 2287, NGC 2323, NGC 2516, NGC 3532, NGC 6791, and Sirius B (Tremblay et al., 2012; Cummings et al., 2016a, 2015, 2016b; Kalirai et al., 2007). From our reanalysis of the M34 we are able to include WD15, WD17, WD25, and WDS2 in our simulations,

while we exclude WD9H and WD25 from the IFMR fit as they just narrowly pass the selection criteria and are suspected to be field objects. From our earlier analysis we also include the physical parameters for WD1, WD2, WD5, WD6, WD12, WD14, WD22, WD27, WD29, and WD30 in M35, and WD4, WD7, and WD27 in NGC 6633. For the additional objects from the literature we use surface gravity and effective temperature as well as their uncertainties. Only the so called classical Hyades DA type WDs are included; 2, 3, 5, 6, 8, and 10 (from Tremblay et al. (2012)). We include just the well known massive LB 1497 WD in the Pleiades. Pulling from two sources, we find 2, 5, 6, 9, 10, 13, 16, 17, 18, 21, 24, 25, and 28 in NGC 2099 are appropriate for our analysis (Cummings et al., 2015, 2016a). From the NGC 2287 sample we use objects 2, 4, and 5. We adopt both of the two known massive WDs in NGC 2323, 10 and 11, while from the NGC 2516 sample we use 1, 2, 3, and 5. We also use 1, 5, 9, 10, J1106-590, J1106-584, and J1107-584 in NGC 3532. The NGC 6791 WD sample, presented in Kalirai et al. (2007), used the models of Bergeron et al. (1992a). We exclude NGC 6791 objects below our critical mass by which contamination due to mass transfer with a binary companion is expected, and in doing so find just objects 7, 8, and 9 are appropriate for our analysis. To maintain consistency we corrected the physical parameters therein to account for the effects of the updated stark broadening profiles and we also folded the published uncertainties with the Liebert et al. (2005a) external errors in quadrature. The physical parameters used for the IFMR analysis are: for WD7  $T_{eff} = 15400 \pm 352$ ,  $\log g = 8.01 \pm 0.071$ ; for WD8  $T_{eff} = 18900 \pm 376$ ,  $\log g = 7.79 \pm 0.071$ ; and for WD9  $T_{eff} = 16700 \pm 361$ ,  $\log g = 7.79 \pm 0.071$ . In some cases the literature values

did not include the 3D corrections of Tremblay et al. (2013), but we have confirmed that this only occurs when the corrections are not needed as the objects are too warm for significant convection.

Table 4.5: White Dwarfs in Open Clusters Added to Our Sample From the Literature

Cluster	(log) Age, Uncertainty	[Fe/H]	Included White Dwarfs	References
Hyades	8.816, 0.0458	0.146	WD2, WD3, WD5, WD6, WD8, WD10	Cummings et al. (2017) Tremblay et al. (2012)
Pleiades	8.041, 0.056	0.01	LB 1497	Cummings et al. (2016a)
NGC 2099	8.732, 0.0458	0.00	WD2, WD5, WD6, WD9, WD10, WD13, WD16, WD24, WD17, WD18, WD21, WD25, WD28	Cummings et al. (2015) Cummings et al. (2016b)
NGC 2287	8.311, 0.069	0.00	WD2, WD4, WD5	Cummings et al. (2016a)
NGC 2323	8.061, 0.083	0.00	WD10, WD11	Cummings et al. (2016a)
NGC 2516	8.176, 0.062	0.065	WD1, WD2, WD3, WD5	Cummings et al. (2016a)
NGC 3532	8.512, 0.028	0.00	WD1, WD5, WD9, WD10, WD J1106–590, WD J1106–584, WD J1107–584	Cummings et al. (2016a)
NGC 6791	9.873, 0.039	0.42	WD7, WD8, WD9	Bonatto et al. (2015) Heiter et al. (2014) Kalirai et al. (2007)
Sirius	8.376, 0.023	0.00	Sirius B	Cummings et al. (2016a)

### 4.2.1 Our Monte Carlo Simulations

The uncertainties in the IFMR are frequently presented as orthogonal error bars in the initial-final mass plane (Williams et al., 2009; Salaris et al., 2009; Cummings et al., 2016a). This representation of the uncertainties is inappropriate as the initial and final masses are correlated. This follows from the use of the Sweeney (1976) method (Figure 1.7). The initial mass of an object depends on the nuclear lifetime which in turn depends on the cluster and cooling ages, however the cooling age depends on effective temperature and surface gravity. Therefore, if temperature or surface gravity move both the final and initial mass are affected. For objects where the relative size of the nuclear lifetime to the cooling age is small the initial and final mass are strongly correlated. The extent of uncertainty in cluster age, temperature, and surface gravity, describe the extent of the uncertainty in initial and final mass, but the uncertainties do not describe the strength of correlation any more than they explore the relative size of nuclear to cooling timescales.

A Monte Carlo simulation is a better way to approach the problem for three reasons. First, an analytical approach which would propagate uncertainties through is not trivial. Through the use of Monte Carlo simulations, the uncertainty in the initial parameters propagate to the uncertainty in the final parameters. This should yield equivalent results to an analytical approach if the Monte Carlo simulation sufficiently samples the uncertainty in the initial parameters (both in parameter range and in number, Press et al. (1992)). Second, the traditional approach fails to graphically illustrate the correlation between the initial and final masses for each object. Finally, a Monte

Carlo simulation allows for exploration of the variable sensitivity of the initial masses to both cluster age and age uncertainties. While full exploration of the cooling and cluster age uncertainties has been done (Salaris et al., 2009) our work is the first to illustrate the results of a Monte Carlo simulation which incorporates these uncertainties outside of the typical presentation of 90 degree error bars. Furthermore, we consider the uncertainties in an open cluster’s age that lead to systematic shifts in the initial masses of all WDs from that one cluster (Williams et al., 2009). These shifts have often been simply added in quadrature with the random error of each object’s initial mass, ignoring correlation which arises from the assumption that the cluster age is the sum of the object’s fusion supported timescale as a star and its cooling age as a remnant. The application of a Monte Carlo simulation allows us to thoroughly explore the effects of the uncertainties without the need to analytically examine systematics which arise from correlation.

We present early results from a partial implementation of the new Monte Carlo simulations here. At present the simulations explore the uncertainties in the cluster age, surface gravity, and effective temperature. While metallicity is fixed across all objects in each cluster at their fiducial values, future work may incorporate uncertainty in this parameter. Metallicity has only a minor effect on the nuclear lifetime in the stellar evolution models of Bressan et al. (2012), so it is expected that the effect of this uncertainty will be dwarfed by the uncertainties we have explored, having only minor effect on our IFMR results. Metallicity will not play much of a role in a relative sense between objects in the same cluster, but if its effect is not completely dwarfed by the

other uncertainties it could be used to test the sensitivity of the IFMR between cluster samples of different metallicities.

For each object we generate 10,000 realizations where each choice of temperature, surface gravity, and cluster age are mapped to an initial and final mass pair. In each realization, we select an effective temperature and surface gravity from Gaussian distributions centered on the adopted value and with a standard deviation equal to twice the stated observational uncertainties (N.B. our values in Tables 4.2 to 4.4 derive from assuming the fiducial effective temperature, surface gravity, and cluster ages). The ranges of uncertainties in the input parameters do not describe the entire space for which values in the initial parameters are possible (see section 2.3.3 for uncertainty discussion). So, describing the Gaussian distribution’s sigma by twice the uncertainty in temperature, surface gravity, and cluster age ensures better accuracy (Press et al., 1992). Although this assumption will be explored in future versions of our new code, assuming a symmetrical distribution for the cluster age is likely to be reasonable as the distribution of data in a typical CMD is roughly symmetrical about an isochrone that is a good fit. Indeed, the choice of a uniform distribution instead of a Gaussian was explored and it was found that it yields similar results. In the results we share in this work the cluster age was sampled from a Gaussian distribution about the fiducial value where twice the cluster age uncertainty was used to represent the standard deviation of the Gaussian. In each of the 10,000 realizations the selected cluster age was held constant for all WDs. The routine then applied the evolutionary models of Fontaine et al. (2001) and Wood (1995) to determine the WD mass and cooling age for a given set



of physical parameters. In turn the cooling and cluster ages are mapped to the nuclear age, and then to the initial mass through the PARSEC models with the assumption of the cluster’s metallicity for that object (Bressan et al., 2012). That is, the method described in section 1.6 is applied here in our new Monte Carlo code. The cooling and cluster age uncertainties, being roughly symmetrical, propagate to symmetrical error on the nuclear lifetime, but this yields a skewed initial mass distribution for each object as the mapping from nuclear lifetime to initial mass through the stellar evolution models is nonlinear. This is the dominant effect of the initial and final mass being correlated, and is amplified when the nuclear lifetime is short or where the errors in age become a more substantial fraction of the progenitor star’s lifetime.

#### 4.2.2 Results and Discussion

We present the results of our Monte Carlo simulations in the initial-final mass parameter space in Figure 4.1. The bottom right distribution in pink describes one object, an outlier, where it is clear that the Monte Carlo simulations result in a well defined range of parameter space. Around an initial mass of  $1.2 M_{\odot}$ , the Monte Carlo simulations for all of the objects from NGC 6791 blend, where again one color represents one object. It is no surprise that the least massive objects derive from the oldest cluster in our sample as lower mass stars have had sufficient time to reach the WD stage, while more massive objects in the same cluster have not been observed as they would have had plenty of time to fade below detection limits. Something similar has been found in the case of M67, where all the objects in this cluster have well constrained initial masses around  $1.5 M_{\odot}$ . The initial mass is relatively well constrained for objects in

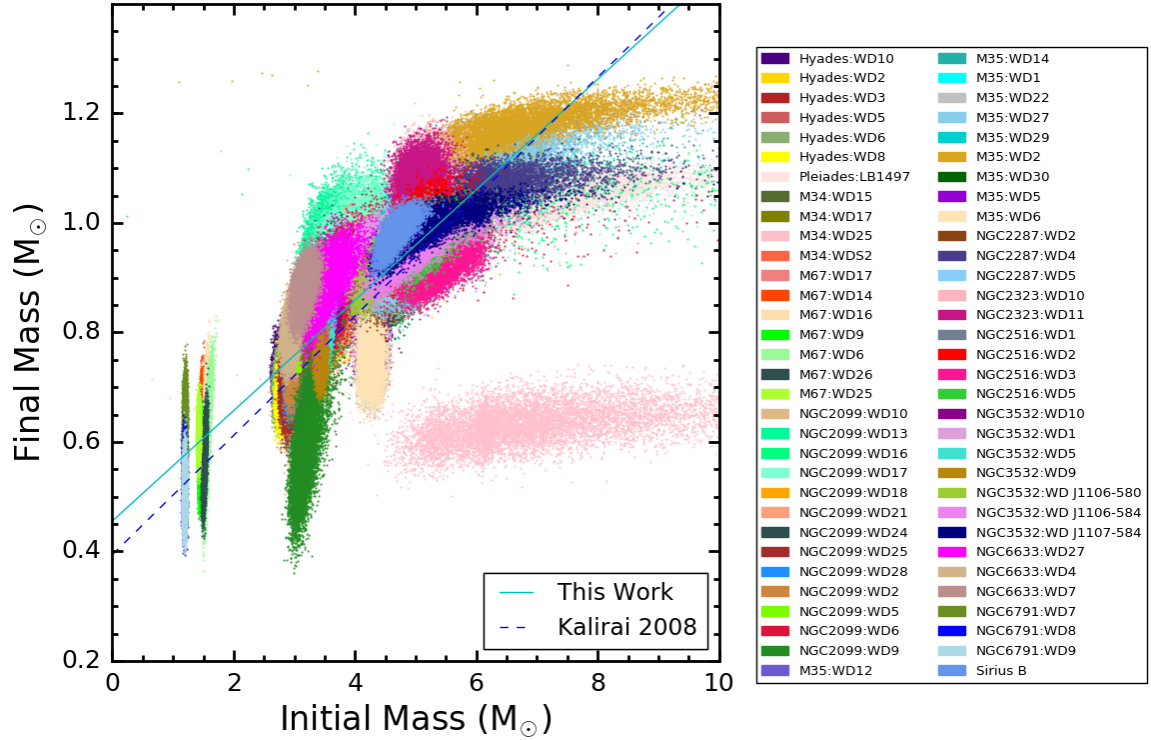


Figure 4.1: The initial-final mass parameter space populated by our WD sample. Each of the 63 objects, plus M34:WD25, are illustrated with one color representing the results of the Monte Carlo simulations for one object. This reveals that for objects at higher mass the correlation between initial and final mass is stronger. Overplotting has covered some objects. Our IFMR, from an unweighted fit to the Monte Carlo simulation data, is shown in cyan (solid line). M34:WD25 clearly stands out as an outlier in the bottom right (the pink points), and is not included in the IFMR fit. Previously published WDs in the metal rich open cluster NGC 6791 (the leftmost distribution) likely experienced elevated mass loss as the addition of the solar metallicity M67 sample (the narrow distribution second from the left) has resulted in a shallower IFMR.

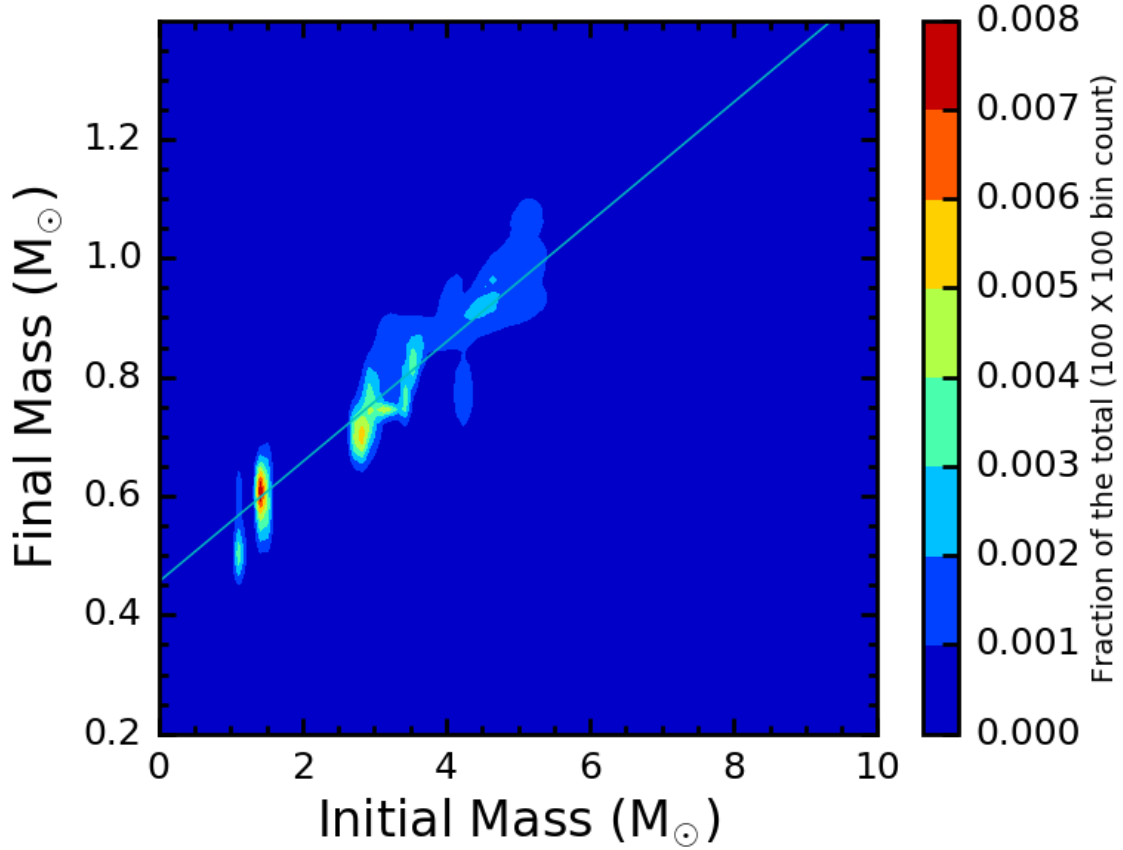


Figure 4.2: Color is used to illustrate density of the same data in the initial-final mass parameter space seen in Figure 4.1. Those data have been binned with 100 bins on each axis, the number of bins chosen so that the location of objects with relatively small errors are represented without significant displacement. The colors represent the fraction of the total data in that bin with respect to the total of all points in the parameter space shown. Our IFMR (in cyan) is overplotted for direct comparison between figures. The density contours suggest that an unbroken line is sufficient as it describes the regions of greatest density, suggesting that more complex functions would overfit these data. The new M67 sample clearly populates a unique parameter space, providing a heavy anchor on the low end of an important relation.

these aged clusters as the nuclear lifetimes are long with respect to the dominant source of uncertainty in initial mass, the cluster age uncertainty, which is typically 10 to 20% of the cluster age regardless of how old a cluster is. There are many overlapping colors at higher masses over a much wider range of parameter space as each color represents another object from each of the other 10 open clusters (and Sirius B). With so many clusters at various age a wider range of parameter space is explored, and hence the space is better populated. The use of one color for each object draws out the shape of each object’s uncertainty. The main purpose of the colors is to illustrate that for any one object the initial and final masses are more strongly correlated at higher mass. The distribution representative of each object is generally asymmetrical which indicates the uncertainty contour for each object has been and would be poorly represented by illustrating errors in a perpendicular fashion along the axes. Overall, the positive trend simply reflects that objects with higher initial mass produce higher mass WDs. Our WD sample covers a broad range of fiducial values, from 1.17 to 7.22  $M_{\odot}$  in initial mass and 0.50 to 1.18  $M_{\odot}$  in final mass.

The asymmetrical appearance of the distributions reflects the correlation of the initial and final mass, which is not of the same strength for all objects. It is clear in the figure that within the uncertainty of any object, for steps of fixed size towards higher final mass, the distribution moves towards high initial mass at an increasingly rapid pace. The correlation is particularly amplified for massive objects through how rapidly initial mass grows with increasingly shorter nuclear lifetime.

Instead of changing the final mass (in effect, surface gravity and temperature) to

examine uncertainty, one could instead consider the one other source of uncertainty the Monte Carlo simulation explores, the cluster age. Consider the effect of cluster age uncertainty on one object. With surface gravity and temperature fixed both the final mass and the cooling age are fixed. The cluster age alone directly affects the initial mass through the nuclear lifetime, which of course maps symmetrical uncertainty in cluster age to asymmetrical uncertainty in initial mass. Therefore, even for fixed final mass some horizontal spread is present which would be larger at higher mass. Once more, since cluster age fixes the scale by which the nuclear and cooling ages are measured, cluster age uncertainty would systematically move the total age for all objects in the cluster in the same direction (towards either lower or higher initial mass). It does so in such a way that for the same shift in cluster age the magnitude of each object's shift is dependent on how short that particular object's nuclear lifetime is.

Some information that has been lost in regions of high density as data of objects have been overplotted on one another, and transparency is not an option as it would blur the color information. Just as the distribution of uncertainty for each object follows a sort of banana shape, so does the sample of each cluster. Objects with shorter nuclear lifetimes display larger asymmetry at high mass. If there were a sufficient number of objects to sample all masses within a cluster, the same sort of banana shape would be seen in an overall sense from the lowest mass objects which show low asymmetry through long nuclear lifetimes to the objects with the shortest nuclear lifetimes with nearly horizontal distributions. In practice, the oldest clusters only show a nearly linear vertical trend, but this is because the objects with the shortest nuclear lifetimes

would have cooled below detection limits. Plotting many clusters in the same figure generally results in overlapped banana like contours, shifted and slightly distorted in the parameter space due to having different cluster ages. These data allude to this pattern, although it is largely obscured by incomplete sampling and the number of overlaid clusters. Underlying individual cluster distributions are evident at the high and low mass ends where the overall distribution is flat and steep accordingly, while in regions where the parameter space is more richly populated a moderate slope is evident over a wide range as clusters and objects are juxtaposed. At its roots, the resulting overall distribution appears non-linear due to the correlation between the initial mass and final masses through the physical parameters, systematic error due to uncertainty in the cluster ages, and the fact that mapping nuclear lifetime to initial mass is nonlinear.

Figure 4.2 presents an alternate view of the initial-final mass parameter space. The data in Figure 4.1 has been binned into 100 bins down each axis. The number of data points within each bin was then normalized to the total number of data points in the parameter space shown, so the fraction measures the density of the parameter space at each bin. This illustrates that the regions of greatest density would fall on a straight line, with the one exception between initial mass values of 4-4.5  $M_{\odot}$ . Although this region looks significantly populated in Figure 4.1, this alternate look shows the region is only sparsely populated. Further, the contours do not suggest a linear piecewise fit is required to better match the regions of highest density. On top of this we have not explored the sensitivity of our results to using different models so the observed scatter may be larger than we observe in this figure. Thus, it would be easy to overfit these

data while assuming a linear function to fit these data is sufficient to get a good fit.

While cumulation of all the cluster distributions illustrates that final mass generally grows with initial mass, it has been suggested, and arguably observed, that the IFMR tapers off at higher masses due to the second dredge up (Cummings et al., 2016a, 2018, and references therein). The distribution in Figure 4.1 seems to flatten out as expected, but this would be easily confused with the fact that the distributions naturally tend to flatten off with higher initial masses with the use of the Sweeney (1976) method. While there may be physical reasons consistent with the trends we observe it seems likely that the shape observed in this figure, being steep at low mass and almost horizontal at high mass, derives primarily from the procedure employed.

The region below the IFMR between initial mass values of 4-4.5  $M_{\odot}$  may be indicative of dependencies of the final mass beyond simply the initial mass, systematic shifts in the age of certain clusters, or simply the result of an incompletely populated parameter space. It is also possible that a few objects have inappropriately passed the selection criteria for isolated membership. M34:WD25 is the obvious outlier in pink at the bottom right of Figure 4.1, and is shown to illustrate that despite the selection criteria in chapter 3 it is likely that there are obvious examples of contamination due to field objects. Although it is not shown in Figure 4.1, as pointed out in section 3.2.3, M34:WD9H was also found to be an obvious outlier in the initial-final mass parameter space which supported the case that it is a field object. Both of these objects are excluded from the IFMR regression.

Our IFMR derives from a regression analysis of data in the initial-final mass

parameter space. Using 10,000 simulations for each object, when each of which has a rather large uncertainty, tends to make the parameter space seem more thoroughly sampled than it actually is. Further, as the Monte Carlo simulations sample from a Gaussian distribution in the cluster age there are some cases where an object’s cooling time exceeds the age of the cluster. For these simulations it is impossible to derive an initial mass from the stellar evolution models as the lifetime by which a star supported itself by nuclear burning is negative. These objects have fewer points in our physically realizable parameter space, and as such are slightly deweighted in our best fit IFMR. This is known to occur for M34:WD20 and WD2, WD12 and WD14 in M35. Notably, this would also be the case for M34:WD25. While those simulations required a negative nuclear lifetime, some other simulations resulted in initial and final mass that are simply outside of the physically realizable parameter space. We restrict the parameter space of our fitted data to that which is illustrated in Figure 4.1. This was chosen as at higher initial mass objects would experience core collapse and not form a WD, while at higher final mass the WD would exceed the Chandrasekhar mass and have also experienced collapse. The lower limits we use generously include all physically realizable values of initial and final mass. The upper limit on what initial mass will experience a core collapse is not precisely defined, with Smartt et al. (2009) suggesting this value is  $8.5^{+1.0}_{-1.5} M_{\odot}$ . It therefore seems reasonable to ask how our IFMR might be sensitive to the extent at which we include data at high initial mass in our fit. The choice of  $10 M_{\odot}$  is conservative, but if their lower limit is instead adopted such that data at higher initial mass than  $7 M_{\odot}$  is excluded from the fit the slope (at 0.107) is less steep by just



0.006, whereas the y-intercept (at 0.434) is lower by 0.022. This is about the size of our uncertainty in these parameters (discussed below). The sensitivity of our IFMR to the value which defines the critical mass, above which core collapse will result while below which a WD will form, is therefore small.

We describe the IFMR as a linear function, having applied method of least squares to these data. Our Monte Carlo simulations have thoroughly explored the uncertainty in cluster age, surface gravity, and effective temperature, so it is appropriate to apply an unweighted fit across all of our Monte Carlo data. Our IFMR, presented in Figure 4.1 as a solid cyan line, is:

$$M_f = (0.101^{+0.005}_{-0.006})M_i + (0.456^{+0.021}_{-0.019}) M_{\odot}$$

This relationship is useful in the range of 1.17-7.22  $M_{\odot}$ . It is, however, important to not extrapolate.

The uncertainties in slope and y-intercept have been obtained through random sampling rather than study of the residuals of our IFMR. The initial and final mass from any particular Monte Carlo simulation derives from random sampling in the cluster age, surface gravity, and temperature, so by pulling the  $i$ th simulation for each object we built a random sample of 63 points. The same fitting routine used to derive the IFMR was then applied to the sample to derive a slope and y-intercept. This process was repeated 8,500 times, exploring nearly all of the initial and final mass points that are physically realizable from the Monte Carlo simulations (we required generously defined criteria:  $0.45 \leq M_f \leq 1.38 M_{\odot}$  and  $0.00 \leq M_i \leq 10.00 M_{\odot}$ ). The results are presented in Figures 4.3 and 4.4, histograms for the slope and y-intercept respectively.

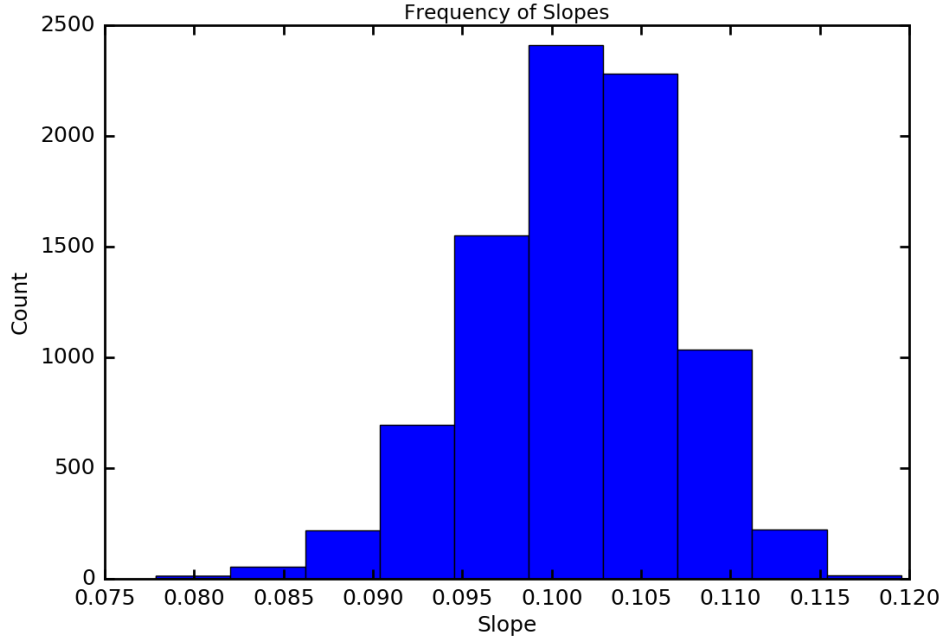


Figure 4.3: Histogram of slopes. 8,500 samples were fit using the method of least squares, where each sample consisted of 63 data points where one point was pulled from each object’s distribution. The median is 0.102, and a 68% contour centered on the median value extends from 0.096 to 0.107.

Our uncertainties describe the difference between the critical values which define a 68% contour and the median in each parameter. The median values are 0.102 for the slope and 0.453 for the y-intercept. Our fiducial values in slope (0.101) and y-intercept (0.456) are well within the 68% tile contour, which is to say the median values and our slope and intercept from fitting all the reasonable Monte Carlo simulation data are consistent with one another. Therefore, the uncertainty about the coefficients in our IFMR from our Monte Carlo simulations is well represented by the contours which describe the uncertainty about the median values.

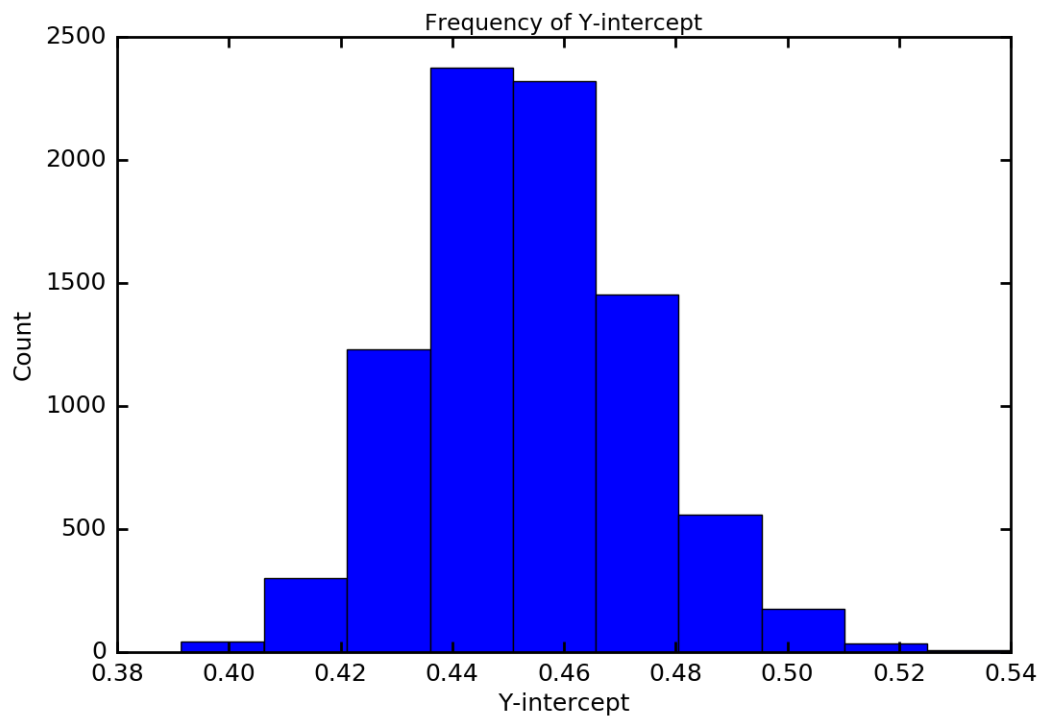


Figure 4.4: Histogram of y-intercepts. 8,500 samples were fit using the method of least squares, where each sample consisted of 63 data points where one point was pulled from each object's distribution. The median is 0.453, and a 68% contour centered on the median value extends from 0.434 to 0.474.

The addition of the M67 sample provides valuable insights. The distribution of our M67 sample is very tight in initial mass. Primarily, this is due to the fact that for older open clusters, the masses of the stars on the main sequence turn-off are much closer in mass to the last star that has evolved off the main sequence. At the advanced age of M67, the result is that objects that have significantly higher masses evolved off the main sequence long enough ago to have had sufficient time to fade below detection limits. Effectively, only the objects which have fairly recently evolved off the main sequence are still above the detection limits of the M67 sample. Hence, M67 has a very narrow distribution in initial mass. In addition to populating previously unexplored parameter space, the M67 sample's distribution also lands slightly above our IFMR. This could be the result of enhanced mass loss from objects in the metal-rich NGC 6791, which may have pulled down the IFMR while providing an equally heavy anchor on the low mass end. As compared with the IFMRs of Kalirai et al. (2008), who found  $M_f = (0.109 \pm 0.007)M_i + (0.394 \pm 0.025)M_\odot$ , and Williams et al. (2009), who found  $M_f = (0.129 \pm 0.004)M_i + (0.339 \pm 0.015)M_\odot$ , M67 has pulled up the intercept and the low mass end while also resulting in a shallower slope. There is much to be understood about the effect of metallicity on scatter in the IFMR.

## Chapter 5

### Conclusions and Future Work

A reanalysis of the IFMR with a more appropriate treatment of uncertainties with the addition of the solar metallicity M67 sample has been presented. Formerly, the low mass end was anchored solely by the NGC 6791 WD sample. At  $[\text{Fe}/\text{H}] = 0.42$  this cluster is particularly metal-rich with respect to the others in our study, and so filling the parameter space with a new WD sample from an aged open cluster with a more typical (nearly solar) metallicity was of particular interest. M67 just happens to be one of the few rich, old, and well studied solar metallicity open clusters. Arguably, the reanalysis of the M34, M35, and NGC 6633 samples with current models has been as significant.

The IFMR presented in chapter 4 has implications for problems in many subfields of astronomy. Using the IFMR the integrated mass loss of any object is known as this is simply the difference between the initial and final mass. When convolved with an initial mass function this is can be used to find the amount of material which remains locked up in all WDs from a burst of star formation. This also describes the fraction of mass that is shed back out into the interstellar medium from which the next generation of stars can form. The IFMR plays a direct role in the evolution of both the spectral energy distribution and metallicity of galaxies. The objects at the high mass end of the IFMR also bound the mass by which an object will form a WD rather than exploding as a core collapse supernova, further characterizing galactic chemical evolution. The IFMR can also be used to find the nuclear lifetime of the coolest field WDs. In conjunction

with kinematic information which reveals to which galactic component that WD belongs to, adding the cooling age to the nuclear lifetime in turn bounds the ages of the galactic components. Also, rapid advancement has recently been made in the field of exoplanets. Here, the IFMR again finds use as it can map the post main sequence mass of a WD to the ZMAS mass for remnants which might host a planet or which show evidence of debris disks. The IFMR presented here can likely be used in ways beyond what have been envisioned here.

## 5.1 Caveats and Future Work

There are some caveats to the derivation of the IFMR presented in this work as well as some future work to be done. While we have been internally consistent wherever possible and believe our semi-empirical relation is precise we have not explored the accuracy of the models we have employed. The work of Cummings et al. (2016a) suggests that the results from using one set of isochrones to another can introduce uncertainty of roughly similar scale to what is found from the sources of error we have considered. Future work could examine the effect of such external error by repeating the analysis with additional sets of stellar evolution models. We have incorporated improvements in the atmospheric fitting routines and have used the most recent WD and stellar evolutionary models. However, some improvements with regards to the treatment of composition could improve the accuracy of our results. The atmospheric species of many WDs is thought to evolve as WDs cool in time. Such spectral evolution is not accounted for in the evolutionary models, although we do note that some of

the WDs in our study probably have thick enough hydrogen atmospheres to have retained their composition throughout their history despite the onset of deep convection (MacDonald & Vennes, 1991; Castanheira & Kepler, 2008). With asteroseismology it is possible to know the thickness of the atmospheric layer of hydrogen, but because WDs only pulsate in narrow ranges of the physical parameters it is not possible to have a very good idea of how likely spectral evolution is to have played a role or if our assumption of thick atmospheres is appropriate for any particular object. Our analysis of M67 has turned up some open cluster DB WDs (Williams et al., 2018), but their analysis is left to future work. To get an idea as to how significant this systematic may be one could consider the difference in cooling time between objects which maintain hydrogen or helium atmospheres. The cooling timescale for a DA WD at 10,000K and  $\log g = 8$  is 603 Myr, whereas for a DB WD of the same physical parameters the cooling timescale is 623 Myr (M. Kilic 2018, priv. comm.). Depending on the nuclear lifetime of the object some 20 Myr may contribute significantly to the uncertainty in initial mass. Assumptions about core composition may also contribute significant systematic error. The stellar evolution models which have been used to map the nuclear lifetime to initial mass were developed independently from the evolutionary models and in general they do not predict the same core composition as the evolutionary models assume. On a per unit mass basis, the number of ions is greater for lighter elements. For a WD of any particular mass this means that the thermal energy content is greater for a WD comprised of lighter elements. Thus, as core composition effects the cooling age the initial mass is dependent on core composition. The cooling ages presented in this

dissertation were derived using evolutionary models which assumed either a carbon or carbon and oxygen mix depending on temperature. There is no reason to expect such an abrupt change in core composition about 30,000 K, but this was done as models with consistent composition that span the range of temperatures were not available. In addition, uncertainty in cluster metallicity has not yet been incorporated in our Monte Carlo simulations. The stellar evolution models which map nuclear age to initial mass depend on metallicity, so incorporating uncertainty in cluster metallicity in the Monte Carlo simulation will contribute some additional uncertainty to the initial mass of each object.

It has only been recently that the core composition for WDs has been explored empirically but much remains to be done on the subject. The only object with an empirically constrained core composition is the object examined by Giammichele et al. (2018), KIC08626021, and so much work remains to be done in expanding our knowledge of core composition over a range of WD masses. Models of stellar evolution predict WDs at low mass have helium cores, while at high mass they suggest the core is comprised of oxygen, neon, and magnesium. For such objects the cooling ages may not be particularly accurate as the evolutionary models assume carbon as a major constituent. If confirmation of these high and low mass compositions comes from future asteroseismology studies there would be two additional real discontinuities in the IFMR, one at each low and high mass. These transitions are likely to be abrupt as it is clear that mass loss grows primarily with the mass of an object, but secondary effects on mass loss (e.g. metallicity, rotation) may turn what would be abrupt transitions into



something less well defined. Future asteroseismology studies will empirically constraint the mass of which transitions in composition occur, but until then an educated guess must be made based on model predictions.

There exists stellar populations that are old enough for low mass objects to have evolved to the WD stage with helium cores (Kalirai et al., 2007), so in principle if studies confirm low mass WDs have helium cores it is possible to examine the kink in the IFMR that arises from this change in core composition. In this dissertation this would not be present as we have not assumed such evolutionary models, but helium core composition for low mass objects could be incorporated in the Monte Carlo simulation such that this can be studied. It should be noted that it is by chance that the transition from helium core to a higher mass core with carbon content occurs is right around where we set our mass cut to exclude binaries. We had aimed to eliminate low mass objects as they often evolve in tight binaries, but that does not exclude the possibility that if a cluster is old and metal rich enough some low mass stars have reached the remnant stage. NGC 6791 is one such example of a stellar population. Kalirai et al. (2007) obtained spectroscopy for the NGC 6791 WD sample, which showed many of the objects on the WD sequence were low mass, and that if they were helium core the cooling ages would bring the age of the cluster as determined from the WD cooling sequence in alignment with cluster ages predicted from fitting isochrones to the main sequence turn off. In doing so, there does exist some indirect evidence that low mass WDs are helium core below  $0.45 M_{\odot}$  and that it is likely that at the metallicity of NGC 6791 many helium core objects have had sufficient time to reach the remnant stage in

an isolated fashion. The formation of these helium core remnants differs from that of their more massive counterparts in that as metal rich red giant stars the objects would have shed mass to the point that their helium core would never grow large enough to undergo a helium flash. Each object would have evolved to the extreme horizontal branch as a sdB or sdO star before exhausting its helium burning shell, after which it would experience some residual contraction (which may drive some explosive runaways) and monotonically cool before being observed today as a low mass helium core WD. Of the three objects which were thought to be of a carbon and oxygen core mixture, contrary to the IFMR work presented in this dissertation, Kalirai et al. (2007) assumed Helium cores for WD8 and WD9 in NGC 6791. Reexamination of the objects in this sample with new observations to see if they are tight binaries should be done as they may have evolved without mass transfer to helium core WDs, and if a much greater fraction of the WD sample in this cluster could be included in the initial-final mass parameter space.

For massive WDs the effect having a different composition has on initial mass is stronger as the nuclear lifetime is short. Exploration of the transition to oxygen-neon-magnesium core compositions should therefore be explored by examining the transitional mass by which the IFMR turns to a shallower slope, reflecting the effect of second dredge up on core composition. We have found in our reanalysis of the massive objects in M35 that many are of higher mass and higher surface gravity than their earlier analysis Williams et al. (2009). We explored this before we had implemented our Monte Carlo routine. The first step was to simply plot the reanalyzed value of temperature

from the 1D models against the published value for each object. The same was done for surface gravity. By comparing the 1D physical parameters the only difference between the published values and the reanalyzed values was the work of Tremblay & Bergeron (2009). A subplot of the residuals showed that the physical parameters had changed in a way that that was consistent with what is expected of the improvements in the spectroscopic models (figure 8, Tremblay & Bergeron (2009)). Therefore, the reason why we generally observe higher masses is the updated physics in the spectroscopic models. This was fortunate as if the spectroscopic models were not the source of the change then we would have compared the previously published masses with that of the reanalysis, propagating the 1D physical parameters with updated models of stellar evolution through which the cluster ages were found and the initial mass found from the nuclear lifetime. Identifying the source of what has lifted our masses was significant as it is these objects which bound how small the ZAMS mass can be and still form a WD as opposed to an object which experiences core collapse. Despite the fact that most objects have been found to be higher in mass, not all have moved significantly upwards. This was also traced to the fact that for cool objects where deep convection plays a significant role in the transportation of energy the 3D model corrections have pulled the elevated physical parameters back down by a magnitude well described in figure 8 of Tremblay et al. (2013). Although we reanalyzed the M35 objects for the sake of consistency with the rest of our cluster samples, a reanalysis of the M35 sample was also performed by Cummings et al. (2016a). Their results are generally consistent with our physical parameters. While we understand how significant the reanalysis of the

cluster samples was, even though evolutionary models for WDs of oxygen, neon, and magnesium composition are available they have yet to be incorporated in the Monte Carlo simulation. This implementation will likely come in future work as it seems likely that empirical evidence will surface showing such a core composition is accurate. Further, additional observations of the hot objects in the sample might be beneficial as metals, easily identifiable in the ultraviolet, can systematically alter the physical parameters of these objects (Gianninas et al., 2010).

Additional multiwavelength observations may also reveal the presence of unresolved binary companions. The possibility of tight binary contaminants in the sample remains an ongoing challenge as they cannot be completely vetted from studies of the IFMR unless if stringent criteria were applied, such that a large fraction of the sample of actual cluster members would also be vetted at the low mass end. We suggest future studies optimize this with efficiency versus rejection curves, but further work on the binary fraction as a function of mass needs to be done before such endeavors can derive meaningful results. In this work objects below  $0.45 M_{\odot}$  have been excluded not because they have not evolved in an isolated fashion, but because the fraction of binaries is known to rapidly fall off about this value (Brown et al., 2011). This selection cut likely excludes good data from aged metal rich environments. Still, some level of contamination above whatever mass cut is chosen is likely as unresolved tight binaries, or remnants which have evolved from them (e.g. M67:WD3 and M67:WD29C), are difficult to identify. X-ray and radio observations could possibly identify the presence of an neutron star companion, while infrared observations could identify M dwarf

companions. Multiple spectroscopic observations could identify shifts in radial velocity, but these observations require considerable resources for what is likely to make only a minor difference on the science.

Significant spread in final mass exists within the M67 and NGC 6791 samples. Aside from the possibility of binary contamination, any number of the concerns raised above could be at fault. Both advancements in the models and the discovery of further WDs in stellar populations of known age will further accelerate our understanding of the systematics involved.

In the future uses of the IFMR would greatly benefit from work which further expands the coverage of the parameter space. This includes WDs in open clusters, globular clusters, and wide degenerate binaries. Recently, El-Badry & Rix (2018) identified nearly 400 wide double WD binaries within 200 pc from the Gaia DR2 release (Gaia Collaboration et al., 2018). These objects could be analyzed with the methodology presented in Andrews et al. (2015). As for the wide period binaries in NGC 6633 (NGC6633:WD4 and NGC6633:WD7), they may provide a means by which a comparison between initial and final mass studies using both the Sweeney (1976) and the Andrews et al. (2015) methods can be done (as discussed in section 3.2.3). If M67:WD10 is also found to not show radial velocity variation from additional spectroscopic observations it may also be useful for this purpose. At present the 0.1-0.2  $M_{\odot}$  discrepancy between these two methods needs to be examined further. Wide binaries where one component is a WD and the systemic age can be found through the companion may also supplement the parameter space, as has been done with the

Sirius system. This has already been done for a handful of other systems, although we excluded these objects from our analysis as they made use of a different set of stellar evolution models and to maintain consistency in methodology (Catalán et al., 2008).

Open and globular clusters are more obvious subjects for filling in and expanding the parameter space. For particularly aged clusters, the age of the cluster far exceeds the timescale for massive WDs to cool and fade beyond detection limits. Our lack of massive WDs in M67, or our rather narrow mass distribution, suggests that few if any stars north of the turn off point have recently completed their stellar evolution. So far, this same thing has been observed in the other aged populations that have been studied (NGC 6791 and M4). The initial mass for these objects, through their long nuclear lifetimes, are well constrained. This, combined with the fact that massive objects have faded below detection limits, means that field objects are easily spotted in these samples (e.g. M67:WD29C and M67:WD3). As they are of low metallicity globular cluster samples may pull the slope of the relation down still further. These samples can be difficult in that they are crowded fields, and their stellar remnants are both cool and faint. Some also shown a double or triple main sequence populations. It is not uncommon for a second main sequence to appear about 0.75 magnitudes above a more well populated sequence in any cluster as many objects are unresolved binaries, but unlike in open clusters it has been shown that at least some globular clusters have sequences which derive from populations of different age (Gratton et al., 2012). Where this is the case the total lifetime of an object cannot simply be assumed to be the age of the cluster, and the Sweeney (1976) method will derive an initial mass which is not

accurate. As open clusters evaporate with time there are few at very old ages, so this may put a limit on how low the low mass anchor on the IFMR can actually go despite the existence of older clusters. By contrast, there are many young open clusters which have yet to be examined for WDs with spectroscopy. Though, with the slope of the initial mass function such efforts may turn up few objects (as was the case for NGC 7063), and at such young nuclear ages the uncertainty in the cooling and cluster ages gives way to high uncertainty in initial mass. Such work would benefit greatly from improvement in the uncertainty of the age of open clusters so this should be an area of greater focus.

## 5.2 Concluding Remarks

Although empirical data rule, theory can also lead observations. Through our physical understanding of stellar evolution the IFMR should have two discontinuities in slope due to the occurrence of a helium flash at low mass and second dredge up at relatively high intermediate mass. This would be a piecewise function which may be further broken due to discontinuities in core composition. Mass loss due to secondary parameters, such as metallicity and rotation, likely play some lesser role in the shape of the IFMR. With a frequentist approach the scatter in the relation is too large to meaningfully illustrate these dependencies. If the IFMR is well described by a steeper slope at intermediate masses, when convolved with the IMF the shape of the IFMR may be able to describe the appearance of what seems like two WD sequences in the recent DR2 GAIA data.

With improvements in line with the issues described in this chapter we may be able to answer long standing questions, such as whether or not the IFMR is a single valued function and if it is linear. In the course of this work improvements were made with the addition of a spectroscopic analysis of the solar metallicity M67 sample, a Monte Carlo approach to explore the uncertainties, and a reanalysis of the M34, M35, NGC 6633, and NGC 7063 WDs samples. In the future the LSST will bring us deep multiband photometry for many stellar populations in the southern hemisphere, and spectroscopy from projects like DESI or follow-up through classical observing modes will increase the sample size. Progress on the IFMR is ongoing, and it will continue to influence astronomy as a whole.



# Bibliography

- Alam, S., Albareti, F. D., Allende Prieto, C., Anders, F., Anderson, S. F., Anderton, T., Andrews, B. H., Armengaud, E., Aubourg, É., Bailey, S., & et al. 2015, ApJS, 219, 12
- Andrews, J. J., Agüeros, M. A., Gianninas, A., Kilic, M., Dhital, S., & Anderson, S. F. 2015, ApJ, 815, 63
- Anthony-Twarog, B. J. 1982, ApJ, 255, 245
- Barber, S. D., Belardi, C., Kilic, M., & Gianninas, A. 2016, MNRAS, 459, 1415
- Barstow, M. A., Bond, H. E., Holberg, J. B., Burleigh, M. R., Hubeny, I., & Koester, D. 2005, MNRAS, 362, 1134
- Bédard, A., Bergeron, P., & Fontaine, G. 2017, ApJ, 848, 11
- Bellini, A., Bedin, L. R., Piotto, G., Salaris, M., Anderson, J., Brocato, E., Ragazzoni, R., Ortolani, S., Bonanos, A. Z., Platais, I., Gilliland, R., Raimondo, G., Bragaglia, A., Tosi, M., Gallozzi, S., Testa, V., Kochanek, C. S., Giallongo, E., Baruffolo, A., Farinato, J., Diolaiti, E., Speziali, R., Carraro, G., & Yadav, R. K. S. 2010, A&A, 513, A50
- Bergeron, P. 1989, PhD thesis, UNIVERSITE DE MONTREAL (CANADA).
- Bergeron, P. 1993, in NATO Advanced Science Institutes (ASI) Series C, Vol. 403, NATO Advanced Science Institutes (ASI) Series C, ed. M. A. Barstow, 267

- Bergeron, P., Liebert, J., & Fulbright, M. S. 1995a, *ApJ*, 444, 810
- Bergeron, P., Ruiz, M. T., & Leggett, S. K. 1997, *ApJS*, 108, 339
- Bergeron, P., Saffer, R. A., & Liebert, J. 1992a, *ApJ*, 394, 228
- Bergeron, P., Wesemael, F., & Fontaine, G. 1992b, *ApJ*, 387, 288
- Bergeron, P., Wesemael, F., Lamontagne, R., Fontaine, G., Saffer, R. A., & Allard, N. F. 1995b, *ApJ*, 449, 258
- Boggs, P. T., Boggs, P. T., Rogers, J. E., & Schnabel, R. B. 1992
- Bonatto, C., Campos, F., Kepler, S. O., & Bica, E. 2015, *MNRAS*, 450, 2500
- Bressan, A., Marigo, P., Girardi, L., Salasnich, B., Dal Cero, C., Rubele, S., & Nanni, A. 2012, *MNRAS*, 427, 127
- Brown, J. M., Kilic, M., Brown, W. R., & Kenyon, S. J. 2011, *ApJ*, 730, 67
- Bruzual, G., & Charlot, S. 2003, *MNRAS*, 344, 1000
- Burbidge, E. M., Burbidge, G. R., Fowler, W. A., & Hoyle, F. 1957, *Reviews of Modern Physics*, 29, 547
- Canton, P. A., Williams, K. A., Gianninas, A., & Kilic, M. 2019, (In Prep)
- Carroll, B. W., & Ostlie, D. A. 2006, *An Introduction to Modern Astrophysics*
- Castanheira, B. G., & Kepler, S. O. 2008, *Communications in Asteroseismology*, 157, 294

- Catalán, S., Isern, J., García-Berro, E., Ribas, I., Allende Prieto, C., & Bonanos, A. Z. 2008, *A&A*, 477, 213
- Cooke, J., Sullivan, M., Gal-Yam, A., Barton, E. J., Carlberg, R. G., Ryan-Weber, E. V., Horst, C., Omori, Y., & Díaz, C. G. 2012, *Nature*, 491, 228
- Cummings, J. D., Deliyannis, C. P., Maderak, R. M., & Steinhauer, A. 2017, *AJ*, 153, 128
- Cummings, J. D., Kalirai, J. S., Tremblay, P.-E., & Ramirez-Ruiz, E. 2015, *ApJ*, 807, 90
- . 2016a, *ApJ*, 818, 84
- Cummings, J. D., Kalirai, J. S., Tremblay, P.-E., Ramirez-Ruiz, E., & Bergeron, P. 2016b, *ApJ*, 820, L18
- Cummings, J. D., Kalirai, J. S., Tremblay, P.-E., Ramirez-Ruiz, E., & Choi, J. 2018, *ApJ*, 866, 21
- Debes, J. H., & Sigurdsson, S. 2002, *ApJ*, 572, 556
- Dobbie, P. D., Napiwotzki, R., Burleigh, M. R., Williams, K. A., Sharp, R., Barstow, M. A., Casewell, S. L., & Hubeny, I. 2009, *MNRAS*, 395, 2248
- Dominguez, I., Straniero, O., Tornambe, A., & Isern, J. 1996, *ApJ*, 472, 783
- Eddington, A. S. 1920, *Nature*, 106, 14
- Eggleton, P. P. 1983, *ApJ*, 268, 368

- El-Badry, K., & Rix, H.-W. 2018, MNRAS, 480, 4884
- Falcon, R. E., Winget, D. E., Montgomery, M. H., & Williams, K. A. 2010, ApJ, 712, 585
- Finley, D. S., & Koester, D. 1997, ApJ, 489, L79
- Fleming, T. A., Liebert, J., Bergeron, P., & Beauchamp, A. 1997, in *Astrophysics and Space Science Library*, Vol. 214, *White dwarfs*, ed. J. Isern, M. Hernanz, & E. Garcia-Berro, 91
- Fontaine, G., Bergeron, P., Billères, M., & Charpinet, S. 2003, ApJ, 591, 1184
- Fontaine, G., Brassard, P., & Bergeron, P. 2001, PASP, 113, 409
- Gaia Collaboration, Babusiaux, C., van Leeuwen, F., Barstow, M. A., Jordi, C., Vallenari, A., Bossini, D., Bressan, A., Cantat-Gaudin, T., van Leeuwen, M., & et al. 2018, A&A, 616, A10
- Genest-Beaulieu, C., & Bergeron, P. 2014, ApJ, 796, 128
- Giammichele, N., Charpinet, S., Fontaine, G., Brassard, P., Green, E. M., Van Grootel, V., Bergeron, P., Zong, W., & Dupret, M.-A. 2018, Nature, 554, 73
- Gianninas, A., Bergeron, P., Dupuis, J., & Ruiz, M. T. 2010, ApJ, 720, 581
- Gianninas, A., Bergeron, P., & Ruiz, M. T. 2011, ApJ, 743, 138
- Gianninas, A., Dufour, P., Kilic, M., Brown, W. R., Bergeron, P., & Hermes, J. J. 2014, ApJ, 794, 35

- Gianninas, A., Kilic, M., Brown, W. R., Canton, P., & Kenyon, S. J. 2015, *ApJ*, 812, 167
- Gomez, T. A. 2017, PhD thesis, University of Texas, Austin
- Gratton, R. G., Carretta, E., & Bragaglia, A. 2012, *A&A Rev.*, 20, 50
- Green, R. F., Schmidt, M., & Liebert, J. 1986, *ApJS*, 61, 305
- Griffiths, D. J. 1995, *Introduction to Quantum Mechanics*
- Hambly, N. C., MacGillivray, H. T., Read, M. A., Tritton, S. B., Thomson, E. B., Kelly, B. D., Morgan, D. H., Smith, R. E., Driver, S. P., Williamson, J., Parker, Q. A., Hawkins, M. R. S., Williams, P. M., & Lawrence, A. 2001, *MNRAS*, 326, 1279
- Hansen, B. M. S. 2005, *ApJ*, 635, 522
- Heiter, U., Soubiran, C., Netopil, M., & Paunzen, E. 2014, *A&A*, 561, A93
- Holberg, J. B., & Bergeron, P. 2006, *AJ*, 132, 1221
- Hubeny, I., & Mihalas, D. 2014, *Theory of Stellar Atmospheres*
- Hummer, D. G., & Mihalas, D. 1988, *ApJ*, 331, 794
- Iben, Jr., I. 1978, *ApJ*, 219, 213
- Kalirai, J. S., Bergeron, P., Hansen, B. M. S., Kelson, D. D., Reitzel, D. B., Rich, R. M., & Richer, H. B. 2007, *ApJ*, 671, 748
- Kalirai, J. S., Hansen, B. M. S., Kelson, D. D., Reitzel, D. B., Rich, R. M., & Richer, H. B. 2008, *ApJ*, 676, 594

- Kalirai, J. S., Saul Davis, D., Richer, H. B., Bergeron, P., Catelan, M., Hansen, B. M. S.,  
& Rich, R. M. 2009, *ApJ*, 705, 408
- Kawaler, S. D. 1995, in *Saas-Fee Advanced Course 25: Stellar Remnants*, ed. A. O.  
Benz & T. J.-L. Courvoisier, 1
- Kharchenko, N. V., Piskunov, A. E., Schilbach, E., Röser, S., & Scholz, R.-D. 2013,  
*A&A*, 558, A53
- Kilic, M., Stanek, K. Z., & Pinsonneault, M. H. 2007, *ApJ*, 671, 761
- Koester, D., & Chanmugam, G. 1990, *Reports on Progress in Physics*, 53, 837
- Kowalski, P. 2006, PhD thesis, Vanderbilt University
- Kowalski, P. M., & Saumon, D. 2006, *ApJ*, 651, L137
- Landolt, A. U. 1992, *AJ*, 104, 340
- Liebert, J., Bergeron, P., & Holberg, J. B. 2005a, *ApJS*, 156, 47
- Liebert, J., Fontaine, G., Young, P. A., Williams, K. A., & Arnett, D. 2013, *ApJ*, 769, 7
- Liebert, J., Young, P. A., Arnett, D., Holberg, J. B., & Williams, K. A. 2005b, *ApJ*,  
630, L69
- Loktin, A. V., & Beshenov, G. V. 2003, *Astronomy Reports*, 47, 6
- Ma, X., Chen, X., Chen, H.-l., Denissenkov, P. A., & Han, Z. 2013, *ApJ*, 778, L32
- MacDonald, J., & Vennes, S. 1991, *ApJ*, 371, 719

- Maoz, D., & Hallakoun, N. 2017, MNRAS, 467, 1414
- Maoz, D., Hallakoun, N., & Badenes, C. 2018, MNRAS, 476, 2584
- McCarthy, J. K., Cohen, J. G., Butcher, B., Cromer, J., Croner, E., Douglas, W. R., Goeden, R. M., Grewal, T., Lu, B., Petrie, H. L., Weng, T., Weber, B., Koch, D. G., & Rodgers, J. M. 1998, in Proc. SPIE, Vol. 3355, Optical Astronomical Instrumentation, ed. S. D’Odorico, 81–92
- McCook, G. P., & Sion, E. M. 1987, ApJS, 65, 603
- Napiwotzki, R. 1997, A&A, 322, 256
- Nomoto, K., Thielemann, F.-K., & Yokoi, K. 1984, ApJ, 286, 644
- Oke, J. B., Cohen, J. G., Carr, M., Cromer, J., Dingizian, A., Harris, F. H., Labrecque, S., Lucinio, R., Schaal, W., Epps, H., & Miller, J. 1995, PASP, 107, 375
- Osterbrock, D. E., Fulbright, J. P., Martel, A. R., Keane, M. J., Trager, S. C., & Basri, G. 1996, PASP, 108, 277
- Paczynski, B. 1972, Astrophys. Lett., 11, 53
- Press, W. H., Teukolsky, S. A., Vetterling, W. T., & Flannery, B. P. 1992, Numerical recipes in FORTRAN. The art of scientific computing
- Renzini, A., & Ciotti, L. 1993, ApJ, 416, L49
- Riess, A. G., Filippenko, A. V., Challis, P., Clocchiatti, A., Diercks, A., Garnavich, P. M., Gilliland, R. L., Hogan, C. J., Jha, S., Kirshner, R. P., Leibundgut, B., Phillips,

- M. M., Reiss, D., Schmidt, B. P., Schommer, R. A., Smith, R. C., Spyromilio, J., Stubbs, C., Suntzeff, N. B., & Tonry, J. 1998, *AJ*, 116, 1009
- Romanishin, W., & Angel, J. R. P. 1980, *ApJ*, 235, 992
- Rubin, K. H. R., Williams, K. A., Bolte, M., & Koester, D. 2008, *AJ*, 135, 2163
- Saffer, R. A., Liebert, J., & Olszewski, E. W. 1988, *ApJ*, 334, 947
- Sahu, K. C., Anderson, J., Casertano, S., Bond, H. E., Bergeron, P., Nelan, E. P., Pueyo, L., Brown, T. M., Bellini, A., Levay, Z. G., Sokol, J., aff1, Dominik, M., Calamida, A., Kains, N., & Livio, M. 2017, *Science*, 356, 1046
- Salaris, M., Serenelli, A., Weiss, A., & Miller Bertolami, M. 2009, *ApJ*, 692, 1013
- Sion, E. M., Greenstein, J. L., Landstreet, J. D., Liebert, J., Shipman, H. L., & Wegner, G. A. 1983, *ApJ*, 269, 253
- Smartt, S. J., Eldridge, J. J., Crockett, R. M., & Maund, J. R. 2009, *MNRAS*, 395, 1409
- Stacey, F. D. 2000, *Journal of Geophysical Research: Solid Earth*, 105, 13155
- Steinhauer, A. 2003, PhD thesis, Indiana University
- Stetson, P. B. 1987, *PASP*, 99, 191
- Sweeney, M. A. 1976, *A&A*, 49, 375
- Tremblay, P.-E., & Bergeron, P. 2009, *ApJ*, 696, 1755



- Tremblay, P.-E., Bergeron, P., & Gianninas, A. 2011a, *ApJ*, 730, 128
- Tremblay, P.-E., Ludwig, H.-G., Steffen, M., Bergeron, P., & Freytag, B. 2011b, *A&A*, 531, L19
- Tremblay, P.-E., Ludwig, H.-G., Steffen, M., & Freytag, B. 2013, *A&A*, 559, A104
- Tremblay, P.-E., Schilbach, E., Röser, S., Jordan, S., Ludwig, H.-G., & Goldman, B. 2012, *A&A*, 547, A99
- Vassiliadis, E., & Wood, P. R. 1993, *ApJ*, 413, 641
- Vidal, C. R., Cooper, J., & Smith, E. W. 1970, *J. Quant. Spec. Radiat. Transf.*, 10, 1011
- Weidemann, V. 1977, *A&A*, 59, 411
- . 2000, *A&A*, 363, 647
- Weidemann, V., & Koester, D. 1983, *A&A*, 121, 77
- Wesemael, F., Greenstein, J. L., Liebert, J., Lamontagne, R., Fontaine, G., Bergeron, P., & Glaspey, J. W. 1993, *PASP*, 105, 761
- Williams, K. A. 2002, PhD thesis, UNIVERSITY OF CALIFORNIA, SANTA CRUZ
- Williams, K. A., & Bolte, M. 2007, *AJ*, 133, 1490
- Williams, K. A., Bolte, M., & Koester, D. 2009, *ApJ*, 693, 355
- Williams, K. A., Canton, P. A., Bellini, A., Bolte, M., Rubin, K. H. R., Gianninas, A., & Kilic, M. 2018, *ApJ*, 867, 62

- Williams, K. A., Serna-Grey, D., Chakraborty, S., Gianninas, A., & Canton, P. A. 2015, *AJ*, 150, 194
- Winget, D. E., & Kepler, S. O. 2008, *ARA&A*, 46, 157
- Wood, M. A. 1995, in *Lecture Notes in Physics*, Berlin Springer Verlag, Vol. 443, *White Dwarfs*, ed. D. Koester & K. Werner, 41
- Yi, S., Demarque, P., Kim, Y.-C., Lee, Y.-W., Ree, C. H., Lejeune, T., & Barnes, S. 2001, *ApJS*, 136, 417
- Zingale, M., Almgren, A. S., Bell, J. B., Nonaka, A., & Woosley, S. E. 2009, *ApJ*, 704, 196
- Zingale, M., Nonaka, A., Almgren, A. S., Bell, J. B., Malone, C. M., & Woosley, S. E. 2011, *ApJ*, 740, 8